DOTTORATO DI RICERCA IN
SCIENZE DELLA TERRA

CICLO XXIX

COORDINATORE Prof. LORENZO ROOK

Semi-automatic analysis of landslide spatio-temporal evolution

Settore Scientifico Disciplinare GEO/05

Dottorando	**Tutore**
Dott. Giulia Dotta	Dr. Giovanni Gigli

Coordinatore
Prof. Lorenzo Rook

Anni 2013/2016

Table of contents

Acknowledgements

Firenze

November 29, 2016

Giulia Dotta

Abstract

Remote sensing techniques represent a powerful instrument to detect and characterise earth's surface processes, especially using change detection approaches. In particular, TLS (*Terrestrial Laser Scanner*) and UAV (*Unmanned Aerial Vehicles*) photogrammetry technique allow to obtain high-resolution representations of the observed scenario as a three-dimensional array of points defined by x, y and z coordinates, namely point cloud. During the last years, the use of 3D point clouds to investigate the morphological changes occurring over a range of spatial and temporal scales, is considerably increased.

During the three-years PhD research programme, the effectiveness of point cloud exploitation for slope characterization and monitoring was tested and evaluated by developing and applying a semi-automatic MATLAB tool. The proposed tool allows to investigate the main morphological characteristics of unstable slopes by using point clouds and to point out any spatio-temporal morphological changes, by comparing point clouds acquired at different times. Once defined a change detection threshold, the routine permits to execute a cluster analysis and automatically separate zones characterized by significant distances and compute their area.

The introduced tool was tested on two test sites characterized by different geological setting and instability phenomena: the San Leo rock cliff (Rimini province, Emilia Romagna region, northern Italy) and a clayey slope near Ricasoli village (Arezzo province, Tuscany region, central Italy). For both case of studies, the main displacement or accumulation zones and detachment zone were mapped and described. Furthermore, the factors influencing the change detection results are discussed in details.

Riassunto

Le tecniche di rilevamento rappresentano un utile strumento per rilevare e caratterizzare i processi gravitativi di versante, in particolare attraverso l'uso di approcci volti ad individuare le aree in movimento. Nel dettaglio, tecniche come il laser scanner terrestre e la fotogrammetria digitale permettono di ottenere rappresentazioni ad alta risoluzione dello scenario osservato sotto forma di una nuvola di punti (*point cloud*) in tre dimensioni. Durante gli ultimi anni, l'uso delle nuvole di punti per investigare i cambiamenti morfologici a scala temporale e spaziale, è notevolmente aumentato.

In questo contesto è maturato il presente progetto di ricerca, durante il quale, l'efficacia dell'utilizzo delle nuvole di punti per la caratterizzazione e il monitoraggio di versanti instabili è stata testata e valutata attraverso lo sviluppo di un *tool* semi-automatico in linguaggio di programmazione MATLAB. Lo strumento di analisi proposto consente di investigare le principali caratteristiche morfologiche dei versanti instabili indagati e di determinare le variazioni morfologiche e gli spostamenti dalla comparazione di nuvole di punti acquisite in tempi differenti. In seguito, attraverso una tecnica di *clustering*, il codice permette di estrapolare i gruppi le zone interessate da spostamenti significativi e calcolarne l'area.

Il *tool* introdotto è stato testato su due casi di studio contraddistinti da differenti caratteristiche geologiche e da diversi fenomeni di instabilità: l'ammasso roccioso di San Leo (RN) e il versante presso l'abitato di Ricasoli (AR). Per entrambi i casi di studio, sono state individuate e descritte le aree caratterizzate da deformazione superficiale o accumulo di materiale e le aree caratterizzate da distacco di materiale. Inoltre, sono stati approfonditi i fattori che influenzano i risultati della *change detection* tra nuvole di punti.

Riassunto

1. Introduction

The term "landslide" is defined as the movement of a mass of rock, debris or earth down a slope under the influence of gravity (Varnes, 1978; Cruden, 1991). This physical system includes a wide range of mass movements (flows, slides, topples, falls), a great range of type of geological materials and activities, and different velocity (Varnes, 1978; Cruden and Varnes, 1996). It evolves in time as a result of three different stages: pre-failure deformations, failure and post-failure displacements (Terzaghi, 1950; Skempton and Hutchinson, 1969).

Landslides are globally widespread phenomena and they represent one of the major type of geological hazards, occurring worldwide more frequently than any other natural disasters, such as earthquakes, floods and volcanic eruptions (IGOS, 2004). Although the action of gravity is the primary reason for a landslide, there are other predisposing factors that affect the slope stability such as soil and rock mechanical properties, slope geomorphic features (gradient and aspect) and land cover characteristics (Cruden and Varnes, 1996). This instability phenomena can be triggered from different factors, including intense or prolonged rainfall, rapid snowmelt, permafrost thawing, earthquakes, volcanic eruptions, toe slope undercutting by water courses or ocean waves and wildfires (Guzzetti et al., 2008). Moreover, according to Nadim et al. (2006), the uncontrolled human activities such as overexploited natural resources, intensive deforestation, poor land-use planning and growing urbanization are causing a documented increase of landslide occurrence. Furthermore, in the last years many authors (Jakob and Lambert, 2009; Borgatti and Soldati, 2010) have investigated the existence of potential correlation between landslide occurrences and climate changes. In detail, precipitations events, the most important triggering factor, are rising in terms of magnitude and frequency and this can increase the landslide occurrence.

Landslides cause a significant number of human loss of life and injury and extensive economic damages to public and private properties. Italy is one of the most harshly affected country in the world by landslide hazard, the estimated landslide losses range from 1 to 2 billion of dollars annually, corresponding to about 0.15% of the national domestic product (Canuti et al., 2004). Considering the importance of landslide problem, experts in the field of geotechnical engineering and engineering geology have for a long time recognised the necessity to have a consistent strategy for the evaluation of landslide risk (Whitman, 1984).

The landslide risk is defined (UNISDR, 2009) as "the expected number of lives lost, person injured, damage to property or disruption of economic activity due to a landslide", and can be expressed by following equation:

$$R = H \times E \times V$$

where: R (*Risk*) is defined as the expected degree of loss due to a particular landslide phenomenon; H (*Hazard*) is defined as a description of the magnitude (M) and probability (P) of occurrence of a landslide within a specified period of time and within a given area of a potentially damaging landslide phenomenon (Fell, 1994); E (*Elements at risk*) includes the population, properties, economic activities, and public services at risk in a given area (Fell, 1994); V (*Vulnerability*) is the potential degree of loss (damage) to a given element or set of elements at risk resulting from the occurrence of a landslide of a given magnitude (Varnes, 1984).

Therefore, a thorough knowledge of the spatial distribution (location, extent and typology) and temporal evolution (style, state of activities and kinematics) of landslides is the first step towards its understanding and preventing disaster and to ensure an adequate level of safety to people living in affected areas.

Nowadays, a variety of remote sensing techniques is available for unstable slopes investigation, which may include landslide recognition, monitoring or hazard analysis and prediction (Scaioni et al., 2014). Regarding to landslide characterization and monitoring or, in wider terms to the evaluation of its changes over time: the commonly used sensors are microwave-based (such as SAR sensors), and optical and laser scanning (or LiDAR – *Light Detection and Ranging*) implemented in airborne and ground-based platforms. These techniques, contrary to traditional and punctual instruments such as extensometers (e.g. Angeli et al., 2000; Corominas et al., 2000; Intrieri et al., 2012), GPS (e.g. Squarzoni et al., 2005; Yin et al., 2010) or total stations (e.g. Barla et al., 2010), provide spatially continuous data, allowing to cover large-scale areas.

In particular the use of optical imagery, processed using digital photogrammetry (Chandler, 1999; Lane et al., 2000; Baily et al., 2003), and laser scanning (Slob et al., 2002; Slob and Hack, 2004; Lombardi et al., 2006; Rahman et al., 2006; Turner et al., 2006; Slob and Hack, 2007; Jaboyedoff et al., 2009; Oppikofer et al., 2009; Sturzenegger and Stead, 2009; Jaboyedoff, 2012; Fanti et al., 2013; Gigli et al., 2013; Gigli et al. 2014) allow to obtain a highly detailed

three-dimensional representation of the observed scenario and, consequently, to perform a morphological and morphometrical characterization of the observed areas. Indeed, the main output of these surveying techniques is a fully three-dimensional array of points, namely *point cloud*, in which a unique x, y coordinate is associated with several elevations. This topographic surface representation is characterized by high resolution, from centimetric to millimetric for both techniques (Slob and Hack, 2004; Harwin and Lucieer, 2012).

During the recent years, the use of these technologies to describe the morphological changes occurring over a range of spatial and temporal scales, by comparing point clouds gathered at different times, is considerably increased (Abellán et al., 2016). Compared to change detection with widely employed radar sensors (Lingua et al., 2008), laser scanning and digital photogrammetry techniques show some advantages including their capability to detect changes in directions different to the line of sight of the instrument and the availability of a complete 3D model of the scenario.

Change detection is defined by Singh (1989) as the process of identifying differences in the state of an object or phenomenon by observing it at different times. Change detection answers the question: did the situation change? Yes or no? When the change detection is quantified, it can be defined as deformation analysis (Vosselman and Maas, 2010). Monitoring morphologic changes or deformations on unstable slopes is strictly related to the characteristics of the applied technique in terms of precision, accuracy and revisiting time, with respect to the displacement rates. Indeed, fast moving landslides (up to 1 m/day) can be effectively monitored using ground-based radar sensors or terrestrial laser scanning while, for very slow moving phenomena (millimetre per year scale deformations) satellite radar data, processed with advanced interferometric techniques, are more suitable.

Considering change detection based on 3D point cloud, two types of approaches can be mentioned, mainly applied in literature to LiDAR data: (a) tracking of corresponding elements within successive point clouds, in order to compute a displacement field (Teza et al., 2007; Monserrat and Crosetto, 2008; Aryal et al., 2012); (b) distance calculation between two point clouds when homologous elements cannot be individuated (Girardeau-Montaut et al., 2005; Abellán et al., 2009; Lague et al., 2013; Kromer et al., 2015).

The work carried out in this PhD thesis, representing the result of a three-years research activity at the Earth Sciences Department of the University of Firenze (Italy), mainly concerns

this latter approach. Furthermore, within the PhD programme, a four months' research period was carried out at the College of Surveying and Geo-Informatics of the Tongji University (Shanghai, China), to improve the knowledge about Laser Scanning technique and its applications.

The main research purpose of this PhD was to develop a new tool for an expeditious semi-automatic analysis to investigate the main morphometric characteristics of unstable slopes by using point clouds and to point out any spatio-temporal changes, by comparing point clouds acquired at different times. To do this, the MATLAB (MATrix LABoratory) programming language was used. Indeed, this software is a high-level technical computing language that operates on matrices and arrays, and allows to work with large datasets, as in the case of point cloud data.

The proposed tool is composed of two separate routines. The former allows to perform a morphometric analysis of the point cloud chosen as *reference* and, therefore, to perform a point cloud comparison between the *reference* cloud and a *compared* one, obtaining the signed (positive and negative) distance values between the two point clouds. Once defined a change detection threshold, the second routine permits to execute a cluster analysis and automatically separate zones characterized by significant distances and compute their area. Therefore, this procedure provides a powerful tool to perform spatial (location and areal extent) and temporal evaluation of instability phenomena at the base of hazard assessment.

The proposed approach was applied on two test sites characterized by different slope instability phenomena, respectively: a rock fall and a shallow landslide in a clayey slope.

In addition to the *Introduction* (*Chapter 1*), this thesis includes a total of eight chapters, structured as follows:

- *Chapter 2.* Contains the basic principles of the remote sensing techniques exploited in this work, that is laser scanning and digital photogrammetry, as technologies capable to provide a 3D representation of the investigated areas in point cloud format.
- *Chapter 3.* Contains an overview of the existing point cloud comparison methods, along with a critical evaluation of their advantages and drawbacks.
- *Chapter 4.* Contains the detailed description of the proposed Matlab tool in all its part and the theory it is based on; it also includes a brief discussion on the factors influencing the change detection between point clouds.

- *Chapter 5.* Describes the potential of terrestrial laser scanning and digital photogrammetry, exploited using the approach described in this thesis, in the two selected case studies.
- *Chapter 6.* Contains a discussion on the advantages and drawbacks of the proposed semi-automatic approach and its applicability to the selected test sites.
- *Chapter 7.* Summarizes the main findings of the thesis and future developments.
- *Chapter 8.* Contains the main references of this work, listed in alphabetical order.
- *Chapter 9.* Consist in a list of the papers written during the three years PhD course.

The already published papers are attached as Annexes.

2. Remote sensing techniques for point cloud comparison

Laser scanning and digital photogrammetry provide 3D model of the observed landscape as an array of points, a so-called point cloud. The former is an active remote sensing technique employing a laser beam to acquire a three-dimensional information of the surface, the latest is a passive remote sensing method involving the visual analysis and optical image interpretation to measure the three-dimensional coordinates of an object. Therefore, in the case of laser scanning technique, the point cloud is measured, on the other hand, the photogrammetry point cloud is computed.

In this thesis, *Terrestrial Laser Scanning* (TLS) technique and *Unmanned Aerial Vehicles* (UAV) digital photogrammetry were examined in depth and utilized with change detection purpose.

2.1 Terrestrial Laser Scanning Technique

Basic principle of laser technology is well-known within the surveying environment since the end of the 1990s. During the last decade, its application in Earth Sciences has been largely increased, both from ground-based (*Terrestrial Laser Scanner* – TLS) and airborne-based platforms (*Aerial Laser Scanner-* ALS). Concerning ALS, the applications range from landslide mapping (Corsini et al., 2009b; Borkowski et al., 2011; Van Den Eeckhaut et al., 2007; Đomlija et al., 2014) to monitoring of wide scale processes (Thoma et al., 2005; Corsini et al., 2009a). Rather, TLS has been widely applied to characterization of rockmasses (Slob and Hack, 2002; Rahman et al., 2006; Jaboyedoff et al., 2007; Slob, 2008; Lato et al., 2009; Sturzenegger and Stead, 2009; Gigli et al., 2013; 2014) and monitoring, especially rock falls (Rosser et al., 2005; Abellán et al., 2009; Abellán et al., 2011), rockslides (Oppikofer et al., 2009) and other landslide types (Teza et al., 2007; Monserrat and Crosetto, 2008; Jaboyedoff et al., 2009; Prokop and Panholzer, 2009).

In the case of this thesis, laser scanning technique applied using ground-based platform was described in detail.

2.1.1 Principle

A LASER (Light Amplification by Stimulated Emission of Radiation) is a device that produces and releases a beam or pulse of collimated, directional, coherent and in-phase

monochromatic radiation. The electromagnetic radiation source can consist of different type of material and distinguishes the lasers as for example gas, solid-state or semiconductor lasers. In literature, a widespread term to indicate this technique is even LiDAR, that stands for Light Detection and Ranging.

The laser scanner method is an active remote sensing technique that allows to obtain the range measurement of the objects located on the observed area. The raw result of the laser scanning survey is a dense, unorganised point cloud, where each point is represented by a three-dimensional coordinate space relative to the scanner's position. In this context, unorganised means that "the points are spatially uncorrelated and they aren't in a spatial structure, this because each point is stored sequentially in the order in which the measurements are made" (Slob, 2008).

According to Shan and Toth (2008) and Wehr and Lohr (1999), the main techniques used in laser scanning surveying for distance determination are: the pulse-based and the phase-based lasers (Figure 1).

The formers measure the time-of-flight (TOF) of a short and intense laser pulse to travel from the instrument to the object and to come back after reflection. A time interval counter measures the time associated with a specific point on the pulse; the device waits for the return of the pulse, or for a time-breaking, before sending out the consecutive pulse. The measured distance is:

$$D_{PULSE-BASED} = c \times t/2 \qquad\qquad [\,1\,]$$

where c is the speed of light and t is the travelling time of the light pulse. The azimuth and the zenith angles of the beam and the amplitude (intensity) of the returned signal are recorded too. The range resolution depends on the resolution of the time interval measurement, but also on the length of the emitted pulse.

The method allows to measure distances of few tens or thousands of meters, in the case of ground-based device, and in the order of hundreds of meters to several kilometres for airborne-based platform.

In the phase method, the laser emits a continuous beam and the distance is measured by comparing the phase of the transmitted and the backscattered sinusoidal signal (Figure 1). In

this case, the distance is determined knowing the frequency of the signal (*f*) and the phase difference between two signals (ϕ):

$$D_{PHASE\text{-}BASED} = \frac{1}{4\pi}\frac{c}{f}\phi \qquad\qquad [\,2\,]$$

Comparing with TOF method, the use of Continuous Wave (CW) laser is restricted to a maximum of seventy to one hundred meters (Slob, 2008) but it enables greater measurement rates.
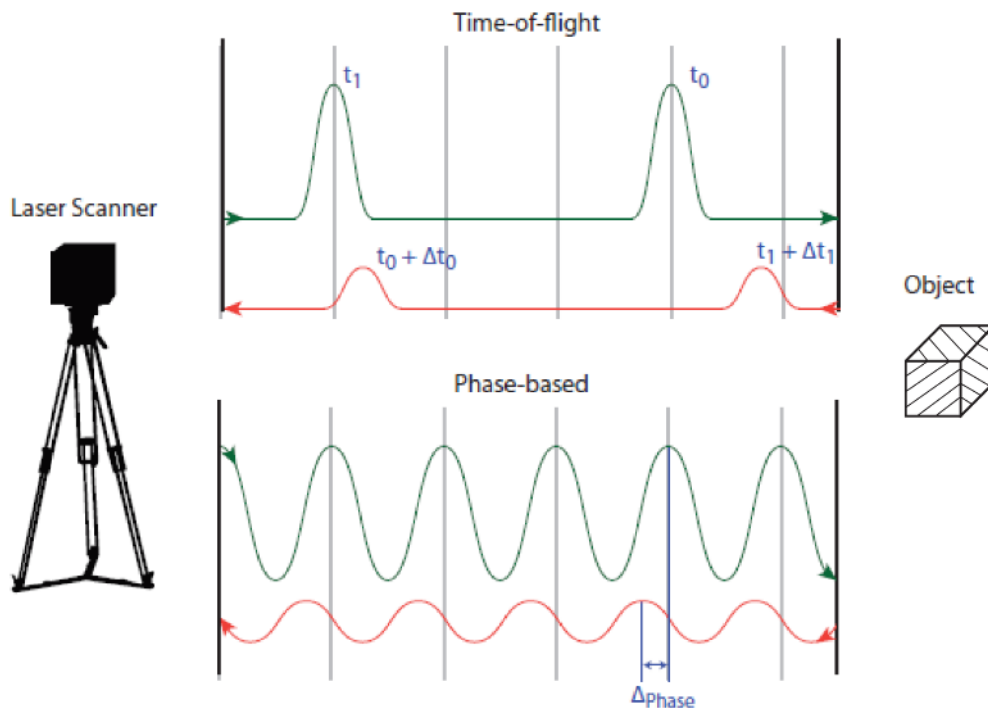
Figure 1. Distance measurement principle of time-of-flight laser scanners (top) and phase based laser scanners (bottom) (modified after Soudarissanane, 2016).

An opto-mechanical scanning mechanism, a rotating mirror or prism and a motor drive, deflects the laser beam in a well-defined pattern. In addition to range measurement (ρ), a vertical Δ_{φ} and a horizontal Δ_{θ} angular steps are defined proving a spherical 3D point cloud of the surroundings (Figure 2). Different deflection apparatuses are currently in use, which produce different point cloud patterns and involve different detection systems.

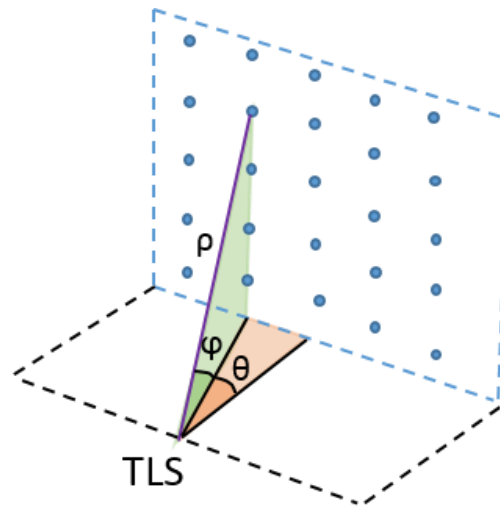*Figure 2. Schematic representation of the point cloud acquisition. A point is measured at an angular position (ϑ, ϕ), with a certain range ρ.*

As regards TLS, the position of the platform is fixed while the scanner moves the beam in vertical and azimuth directions allowing the measurement of a series of profiles with respect to the device.

2.1.2 Accuracy and precision

The accuracy is among the main parameters which characterize the distinct laser scanner instruments, influencing the quality of results and it is defined as the degree of closeness of a range measurement to the real distance. The accuracy of an acquisition derives from the systematic errors, that is from the reproducible errors defined by the biases of the measures (Figure 3).

On the other hand, the precision (also called reproducibility or repeatability) of the acquisition derives from the random errors described by the statistical dispersion of the measurements and it is the degree to which further measurements show the same results (Figure 3); this kind of errors are not reproducible and are determined through the redundancy of information and expressed as standard deviations.
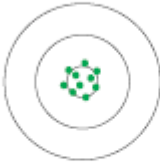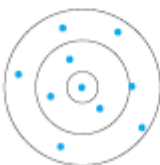
Precision \ Accuracy	High accuracy — Small systematic errors	Low accuracy — Large systematic errors
High precision — Small random errors		
Low precision — Large random errors		

Figure 3. Random errors and systematic errors, from which precision and accuracy respectively depend (from Soudarissanane, 2016).

The range accuracy for both TOF and CW methods, depends on the inverse of square root of the signal-to-noise ratio which is dependent on several factors, such as background radiation, measurement rate and power of received signal. Furthermore, this parameter depends on the ranging signal (the pulse length or the rise time for pulse-based ranging, the wavelength of the ranging signal for the phase-based) (Wehr and Lohr, 1999). For these reasons, the accuracy decreases when increasing range, complexity of the observed surface (surface roughness) and angle of incidence (Abellán et al., 2009; Soudarissanane et al., 2009; Voegtle et al., 2008).

The accuracy of range measurement can usually vary from millimetric to centimetric values and can reach values lower than 10 millimetres (Frohlich and Mattenleiter, 2004) depending on the distance of the target. In the case of phase measurement principle it can be possible to achieve accuracy up to a few millimetres, making this method more accurate than the other.

2.1.3 Resolution

Another important parameter is the resolution, defined as the level of detail that can be observed in a point cloud (Pesci et al., 2011; Jaboyedoff et al., 2012). Two kinds of resolution can be defined: the range and the angular (or spatial) resolution. The first one represents the ability to distinguish two objects on the same LOS (Line Of Sight) and it is governed by pulse

length (typically 3-4 mm for long range devices, Pesci et al., 2011). The second one is the ability to resolve two objects on adjacent LOSs and it depends on: the user-defined sampling interval, common interpreted as the spacing between points of a point cloud; and the laser beam width (spot dimension or laser beam diameter - Abellán et al., 2014), which is a function of the device-target distance and of the characteristics of the instrument.).

Point density depends on: the range resolution, usually reported in thousand pulses per second or kHz; angular resolution; the distance sensor-object; the geometry of the scanned object; and the speed of the moving platform. The expressions *point density* or *pulse density* should be interchangeable, unless the target range is out of range and the signal is dropped (Pirotti et al., 2013).

2.1.4 Laser beam and footprint

Generally, the beam provided by the laser source is assumed to have an ideal Gaussian distribution (Figure 4) and the energy is normally scattered across the emitted beam. Owing to diffraction, the emitted beam diverges and the beam width increases as distances get longer resulting in a larger footprint on the surfaces to be measured (Shan and Toth, 2008), such that the footprint may be considerably greater than the point spacing at long distances. A smaller footprint is more advisable enabling a better measurement of the observed object.

According to Weichel (1990), the beam width (*w*) diverges non-linearly from the minimum spot diameter (i.e. the beam waist, w_0) as:

$$w(r) = w_0 \sqrt{1 + \left(\frac{\lambda r}{\pi w_0^2}\right)^2} \qquad\qquad [\,3\,]$$

where *r* is range relative to the beam waist location, λ is the wavelength of the laser light and $\frac{\lambda}{\pi w_0}$ is the beam divergence for $r \to \infty$ when the laser beam asymptotically nears a cone (γ_0).

Usually the laser scanner instruments use lenses and other optical elements to collimate the beam and reduce the divergence. For every device, the beam divergence is specified in the technical data sheet (e.g. for Riegl LMS-Z420i, the beam divergence is 0.25 mrad that correspond to 25 mm increase of beamwidth per 100 m of distance). The assumption of a Gaussian intensity profile is advantageous since the beam intensity remains Gaussian after refraction of optical devices.
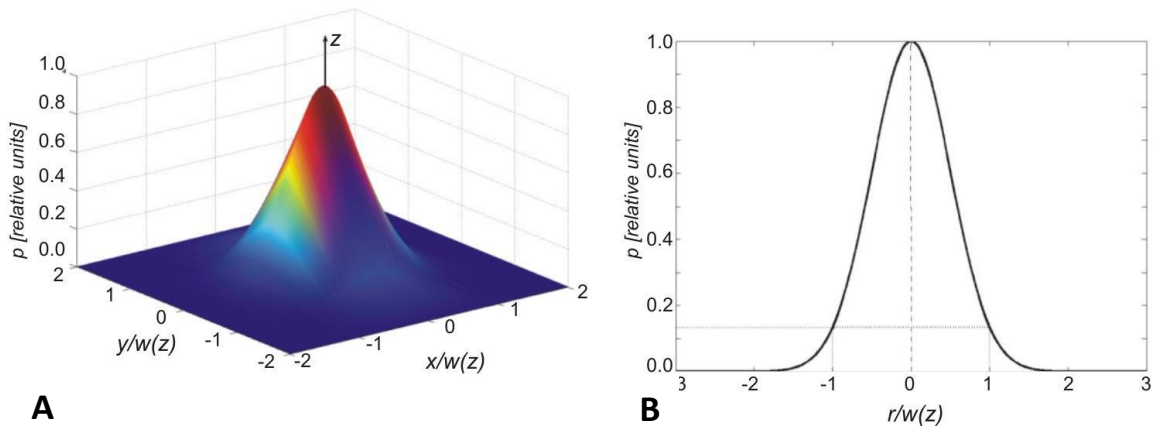
Figure 4. A) Power distribution around the laser beam axis where z shows the direction of propagation; B) radial power profile (from Pesci et al., 2011).

The definition of the footprint is the intersection area between a surface and the laser beam. Its shape depends on two factors which are the topography or shape of the surface (e.g. planar, spherical) and the scanning geometry, that is the angle at which the laser beam hits the surface. The diameter of a laser beam footprint orthogonally hitting a flat surface is defined as

$$d(r) = d_0 + 2r \, tan(\gamma) \qquad\qquad [4]$$

where γ is the beam divergence and the footprint results in a circular shape. The area illuminated by the diverging beam when it reaches the target is

$$A = \frac{\pi}{4}(d + r\gamma)^2. \qquad\qquad [5]$$

When the beam hits a surface that is slanted with respect to the laser source, the resulting footprint is elongated (Figure 5). If the hit surface is irregular in shape or elevation, the return signal will be the average of the mixture of reflections occurring within the circular or elliptical area illuminated by the incident laser radiation.

Figure 5. A laser beam hitting perpendicularly a surface (circular footprint) and a laser beam hitting a surface at an incidence angle α (ellipsoidal footprint) ((from Soudarissanane, 2016).
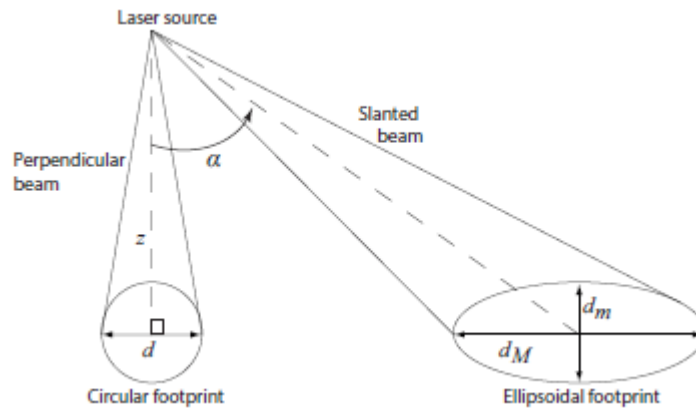
2.1.5 Maximum range and reflectivity

The maximum distance "which can be reached by a pulse which can effectively provide a return signal" (Pirotti et al., 2013) depends on the object reflectivity (i.e. on its composition) and the backscattering properties of the hit surface; which in its turn is influenced by the geometry of the surface, such as angle of incidence and surface roughness.

This parameter depends also of survey conditions, laser wavelength and pulse repetition rate of the device. Effectively the emitted pulse energy is inversely proportional to the pulse repetition rate.

The amount of energy reflected is measured and recorded as intensity. This value, provided for each point in addition to spatial information, is defined as the power of the backscattered radiation and it is usually normalized on a scale ranging from 0 to 255. This parameter depends on the reflectance properties of the object surface, along with instrumental and atmospheric effects and scanning geometry (such as the range and the incidence angle).

Nowadays, most of the laser scanner devices provide at least first and last return pulse, and at most allow to record the entire full waveform of the backscattered signal. The full waveform technology is used in the airborne lidar since 2004 while only the last generation of TLS allows to acquire in principle an infinite number of echoes and to perform a complete waveform analysis (Mallet and Bretar, 2009). Respect to discrete return laser systems, this kind of sensors derive the physical properties of the hit objects and allow discriminating the vegetation from the ground (Mallet and Bretar, 2009; Guarnieri et al., 2012; Barbarella and Fiani, 2013). In fact, when the vegetation is not very dense, it is often assumed that the first

echo belongs to the canopy top and the last pulse to the ground. But it is also important to remember that the two first echoes contain about 90% of the total reflected signal power (Mallet and Bretar, 2009).

In this regard, the survey of a landslide area in Sichuan province (south-western China) carried out from the College of Surveying and Geo-Informatics research group is reproduced here (Figure 6). The used device is a 3D VZ-Line Laser Scanner RIEGL VZ-4000 that allows time of flight measurements of scanner-object distance up to about 4000 m. The Riegl's V-Line technology is based on echo digitization and online waveform processing. The associated operating and processing RiSCAN PRO software package (Riegl, 2013) allows displaying multi-target classification (first, other, last and single targets). Thanks to full waveform technology, the discrimination between different returned pulse groups was possible (Figure 6). For ground monitoring purpose, the last back-scattered pulse is ordinarily the most relevant (Jaboyedoff et al., 2012); instead the points belonging to first and other target groups are generally attributed to vegetation features.
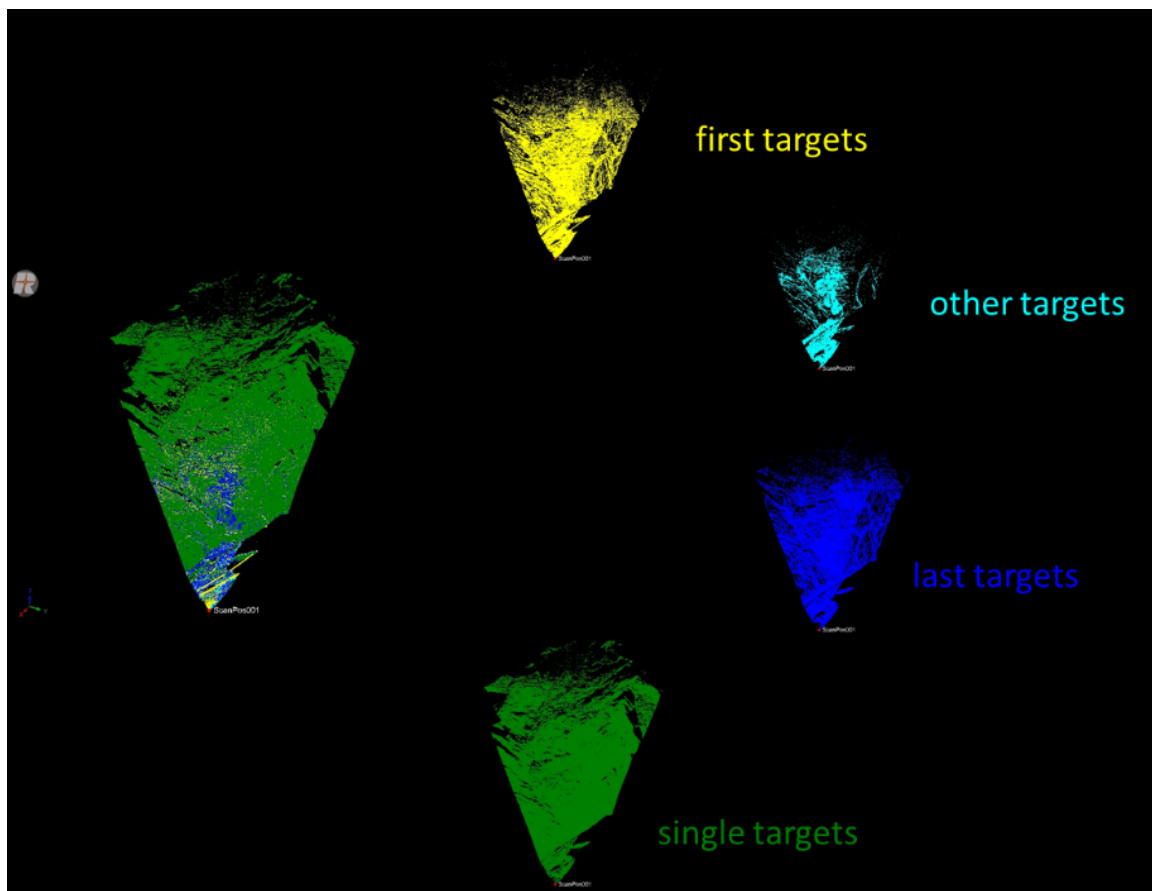

Figure 6. Example of multi-target classification.

2.1.6 Survey workflow

A survey using terrestrial laser scanner produce a huge amount of data in a very short time, therefore a thorough planning of the surveying campaign is recommended. The choice of the location and the viewpoint of the survey station should consider dimension and complexity of the scanned area to minimize occlusions (this error source is analysed in paragraph 3.1.1). In some cases, the occlusions can be reduced by performing scanner surveys from multiple locations (Lato et al., 2010). Furthermore, as a function of the level of detail of the investigation, the resolution and the resulting point density should be planned.

Usually, during the survey, the positions of targets positioned on the scenario are measured using Real Time Kinematic GPS to georeference the scansions in a global coordinate system, e.g. World Geodetic System (WGS84) and its projections. Special targets are provided by the vendors. As an alternative, even a direct georeferencing could be possible if the position and the orientation of the device are known.

It is important to remember that the laser scanner product features like as point density, positional accuracy, scan geometry and surface morphology, are not permanent in the space domain because they change during the survey.

The raw point cloud resulting from the survey is successively submitted to filtering and registration stages (pre-processing phase) (Figure 7). Automatic algorithms can be used to filter outlier points and vegetation using the characteristics of the point cloud geometry (e.g. Brodu and Lague, 2012) or the intensity of the returned signal (e.g. Pesci et al., 2008). Unfortunately, most automatic algorithms cannot clean the low-lying plants, dense vegetation or bushes; in this case a manual editing is required.

When the number of scan positions for the same scenery is more than one, or two or more scans of the same area were acquired at different times; an overlying point cloud coregistration is mandatory and can be performed with two different approaches: using ground control points (GCPs), which are in common to different scans (*target-based* registration) otherwise using cloud matching techniques based on overlapping features within the clouds (*feature-based* registration, e.g. Bae and Lichti, 2008) or *point-to-point* (and *point-to-surface*) methods (e.g. ICP algorithm, Besl and McKay, 1992; Olsen et al., 2011; Antova, 2015), considering a cloud as the reference scan.
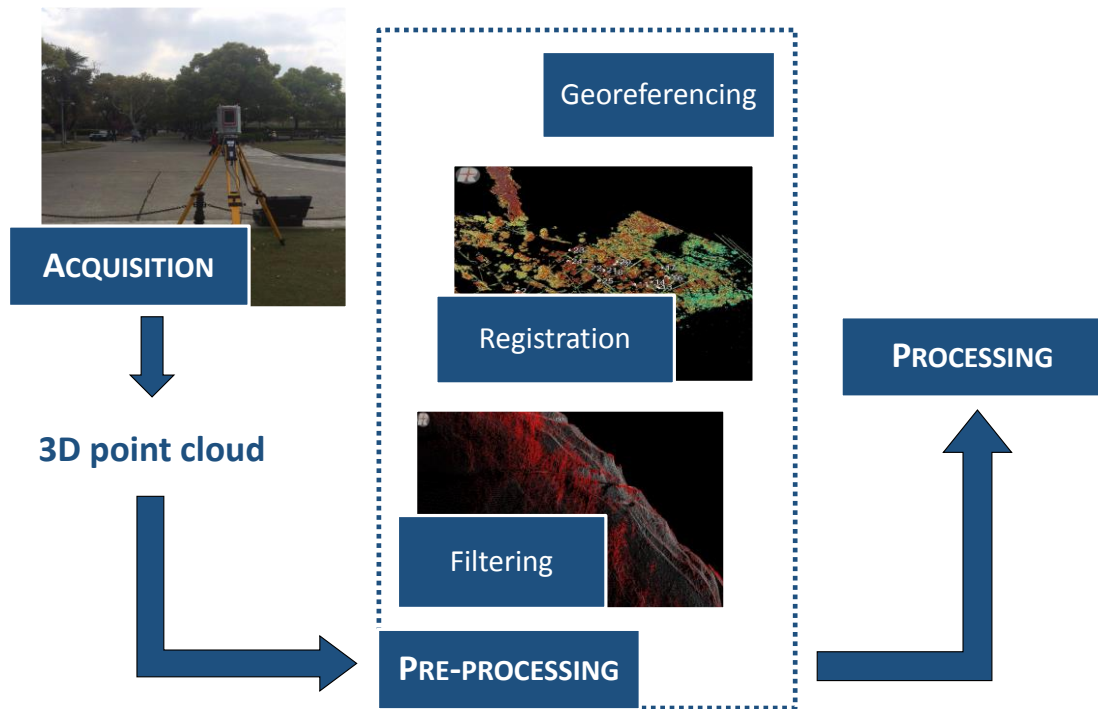
Figure 7. Schematic survey workflow.

2.2 Digital Photogrammetry Technique

Photogrammetry is a technique that allows to obtain precise metrical information about three-dimensional objects (shape, dimensions and geographical position), by means of the interpretation, combination and measurement of photographic images.

The recent developments of the technique, thanks to the availability of digital images, introduced new interesting fields of applications such as architectural design, topographical surveys, cartography, up to environmental geology.

Although the first digital photogrammetric applications were aimed to the architectural modeling, photogrammetry developed mainly for topographical and terrain surveys and was, until the end of the 20th century, widely applied as "aerial photogrammetry" (Figure 8).
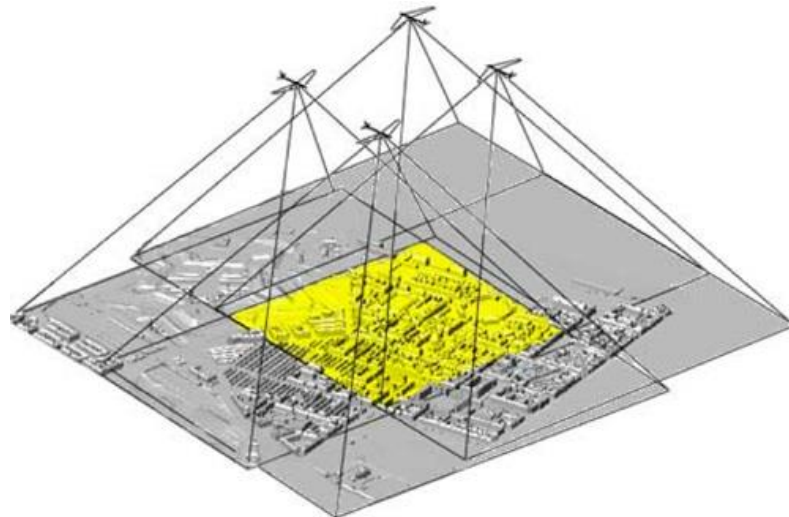
Figure 8. General acquisition scheme of overlapping aerial images for the photogrammetrical reconstruction of a 3D surface model.

Formerly, aerial photogrammetric surveys were performed using expensive and heavy optical devices, a thing that strongly limited the diffusion of the technique. In the last two decades, the diffusion of more powerful computers, allowing to handle huge amounts of data, along with the recent technological progresses in computer-graphics, allowed to perform the most part of the photogrammetric surveying in digital environment.

Indeed, the acquisition of remotely sensed data and aerial imagery from a range of cheap, lightweight platforms on which to deploy imaging sensors, such as *Unmanned Aerial Vehicles* (UAVs) (e.g. Lejot et al., 2007; Niethammer et al., 2012) and tethered kites and blimps (e.g.

Marzolff et al., 2003; Boike and Yoshikawa, 2003; Smith et al., 2009; Vericat et al., 2009) is gradually becoming more commonplace.

Photogrammetric surveying represents nowadays a valid alternative to conventional airborne surveys, including LiDAR and photography that often are of restricted use due to the high three-dimensionality of mountainous landscapes, which results in significant line of sight losses and image foreshortening (Westoby et al., 2012).

The 3D point clouds, processed using digital optcal images is comparable to that produced using active sensors such as laser scanners (e.g. Eisenbeiss and Zhang, 2006) but, in this case, the point density of the cloud is a function of the images resolution, the image coverage of the area and camera-object distance.

Digital photogrammetry is a well-established technique for acquiring dense 3D geometric information of terrain from stereoscopic overlaps of photo sequences. These captured by a calibrated digital camera set in a fixed position on the ground in front of scenario and without any physical contact (Zhang et al., 2004). During past few years, with the rapid development of digital photogrammetry techniques and the availability of ease-using, focusable and relatively cheap digital cameras, the method and device used in terrestrial photogrammetry changed greatly. Therefore, thanks to its increasing efficiency through time it gained wide applications in many fields such as 3D building reconstruction, heritage protection and landslides studies (Grussenmeyer et al., 2008; Travelletti et al., 2012; Scaioni et al., 2015; Fan et al., 2016). However, in spite of great development of traditional terrestrial photogrammetry over years, it is still necessary to set some control points on the slopes to be measured (Stavroulaki et al., 2016) if not supported by other technologies (Forlani et al., 2014). For the complex nature of the observed scenarios the setting control points around the objects is sometimes a very time-consuming and labour-intensive job. Principally, photogrammetry can be divided into two fields of activity depending on the lens-setting: long-range (with camera distance setting to indefinite) and close-range (with camera settings to finite values; i.e. up to about 300 m) (Gopi, 2007). In the landslide and disaster management studies, the first type is usually more exploited for landslide characterization and general mapping (Wolter et al., 2014), while the second type finds a wide applicability in high precision metrological and deformation monitoring applications (Cardenal et al., 2008; Scaioni et al., 2015).

In the last decade, the combination of rapid development of low cost and small UAVs with improved battery technology, and the recent improvements of conventional sensors (Optical and LiDAR) in terms of cost and dimensions, led to new, interesting scenarios in environmental remote sensing and surface modelling and monitoring (Colomina and Molina, 2014; James and Robson, 2012; Remondino et al., 2011; Eisenbeiss and Sauerbier, 2011). In particular, the UAV remote sensing has the following advantages: real-time, flexibility, high-resolution, low costs, and collection capacity of information in dangerous environments without risk to the operator (Chang-chun et al., 2011).

The exponential increase of UAV use for aerial video and photography, along with the development of numerous commercial and open-source software packages, opened new perspectives for landslide surveying. In particular, the recent development of new algorithms for digital photogrammetry, based on *Structure from Motion* (SfM) (Ulman, 1979; Turner et al., 2012; Westoby et al. 2012) and *Multi-View Stereo* (MVS) (James and Robson, 2012) techniques, allows to obtain high resolution 3-D models, point clouds and digital ortho-photos of landslides, even using compact and consumer-grade digital cameras (Lucieer et al., 2014; Niethammer et al., 2011; Niethammer et al., 2010; Rossi et al., 2016).

The traditional methods of softcopy photogrammetric (or digital photogrammetric) require the cameras 3-D location, or georeferenced ground control points. For more precision, both must be added. In contrast, the SfM method solves the camera pose and scene geometry simultaneously and automatically, using a highly redundant bundle adjustment based on matching features in multiple overlapping, offset images (Westoby et al. 2012). The bundling adjustment process is based on a database of features, automatically extracted from a set of multiple overlapping images (Snavely, 2008).

In the case of landslide characterization and monitoring (e.g. Eisenbeiss, 2008; Carvajal et al., 2011; Niethammer et al., 2012; Oda et al., 2016), the aerial imagery acquisition through UAV use permits to overcome some limits of ground-based photogrammetric surveying such as shadowing effects in presence of areas not visible from the observing position, due to high vegetation or topographical features of the slope, that can drastically reduce the accuracy of the resulting digital models.

2.2.1 Processing chain

Numerous software packages are available, both commercial and open source, to perform photogrammetric processing of sets of digital images. Some of them are difficult to use, allowing to set parameters and routines only by command line and with no GUI, whether others are developed by specialized companies for commercial use, with intuitive user interfaces, user manuals and well driven processing workflow.

Although every program has a different design, graphics, tools and computing requirements, they share the general workflow to reconstruct 3D data from overlapping digital images, along with the most commonly used routines.

In this paragraph, the SfM technique, one of the most diffuse approach for image matching and point cloud generation, is briefly treated. The general processing steps are illustrated in Figure 9 and described according to Turner et al. (2012).

The first step consists in selecting the photos to be used for the image matching and requires the manual elimination of any images outside the study region or of limited quality. The images could be optionally geotagged by adding a geographic coordinate of the shot point, obtained by onboard GPS, to the EXIF header of each photo. Subsequently the input images are aligned using *Bundle Block Adjustment* (BBA), a procedure necessary to reconstruct the exterior orientation of each photograph and, if required and provided the geometry of the block of photographs allows it, to compute additional parameters such as the interior orientation (Turner et al., 2012).

Tie/pass points are required to complete a BBA and are typically automatically generated in the case of traditional aerial photography by an interest point extractor algorithm, generally called *Scale-invariant Feature Transform* (SIFT). The SIFT algorithm has the potential to generate a large number of features that can be used as tie/pass points, supplying more redundant observations for a BBA and thus improving the accuracy of the results (Zhang et al, 2011).

SIFT feature descriptors are invariant for the scale and orientation, but affine to the distortion and partial illumination changes and can be matched across multiple images. Using the conjugate (matched) image points as input, the bundle block adjustment is applied to compute the exterior orientation (position and orientation) of each camera exposure station.

In addition, the bundle adjustment computes the interior orientation parameters (focal length and two radial distortion parameters) of each image, although if required these parameters can be implicitly defined and fixed for all images.
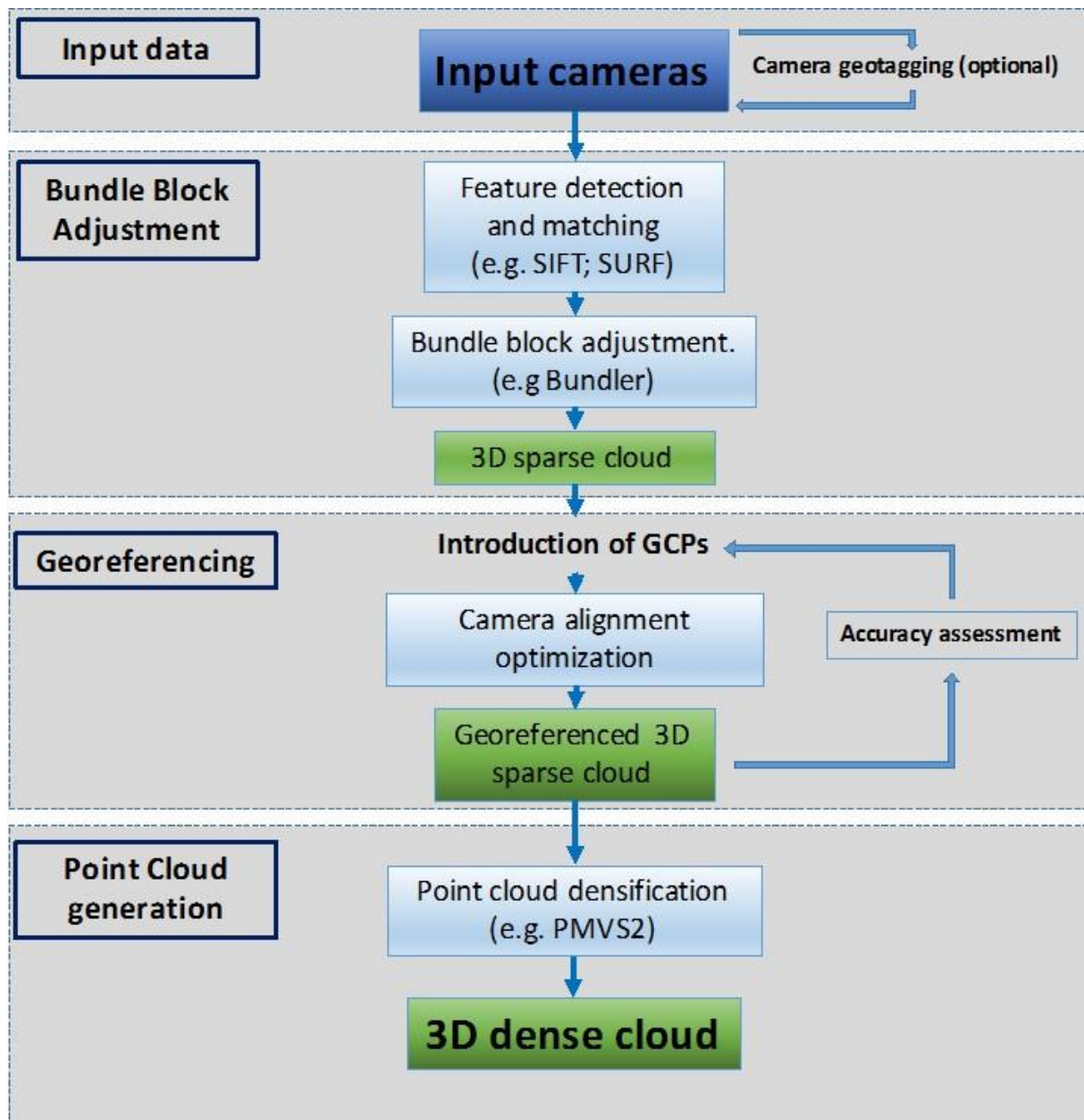
Figure 9. Flow diagram describing the main step of digital photogrammetric processing.

The result of the Bundle Block Adjustment is a sparse point cloud (Figure 10A) composed by all the points extracted by SIFT in overlapping images, in the three-dimensional space.

In case of using geotagged images the 3D coordinates of the exposure stations are extracted from the Bundler output and denoted px, py, pz. Image EXIF header information is then read to extract the matching GPS location. The GPS latitude, longitude and altitude (relative to the

WGS84 datum) can be subsequently converted into the UTM projected coordinate system, resulting in easting, northing, and ellipsoidal height coordinates. Transformation to an orthometric height system is also possible using a local geoid model if required.

Seven parameters of Helmert transformation (three translations, three rotations and one scale) could be used to describe the relationship between the point cloud coordinate system (model space) and a global (object space) coordinate system. The corresponding exposure station coordinates from the bundle adjustment and the GPS are then matched to provide a list of point pairs used to compute the parameters of the Helmert transformation.

If some ground control points (GCPs) are established prior to photography, then the global coordinates of these GCPs can be used to derive the parameters of the Helmert transformation, rather than rely on GPS data from the UAV. Accurate GCP coordinates can potentially improve the solution of the Helmert transformation and therefore result in a higher accuracy of the final point cloud and image features (Camera alignment optimization in Figure 9) (Figure 10B).

The point cloud generated by the BBA is relatively sparse and insufficient to reliably identify the GCPs. A novel multi-view stereopsis algorithm (Furukawa and Ponce, 2009) can be applied to the output from the Bundler software to densify the sparse point cloud (Figure 10C). This algorithm is implemented in the *Patch-based Multiview Stereo* (PMVS2) software. A detailed description of the algorithm can be found in Furukawa and Ponce (2009) and Lucieer et al. (2011). The resulting PMVS2 point cloud has extremely dense point spacing, typically around 1–2 cm (Lucieer et al., 2011).

In this thesis Agisoft Photoscan Software 1.2 .4 release (Agisoft LLC, 2016), one of the most known software packages for photogrammetric processing, was used to perform each step, obtaining digital point clouds of the selected test site in Ricasoli village.
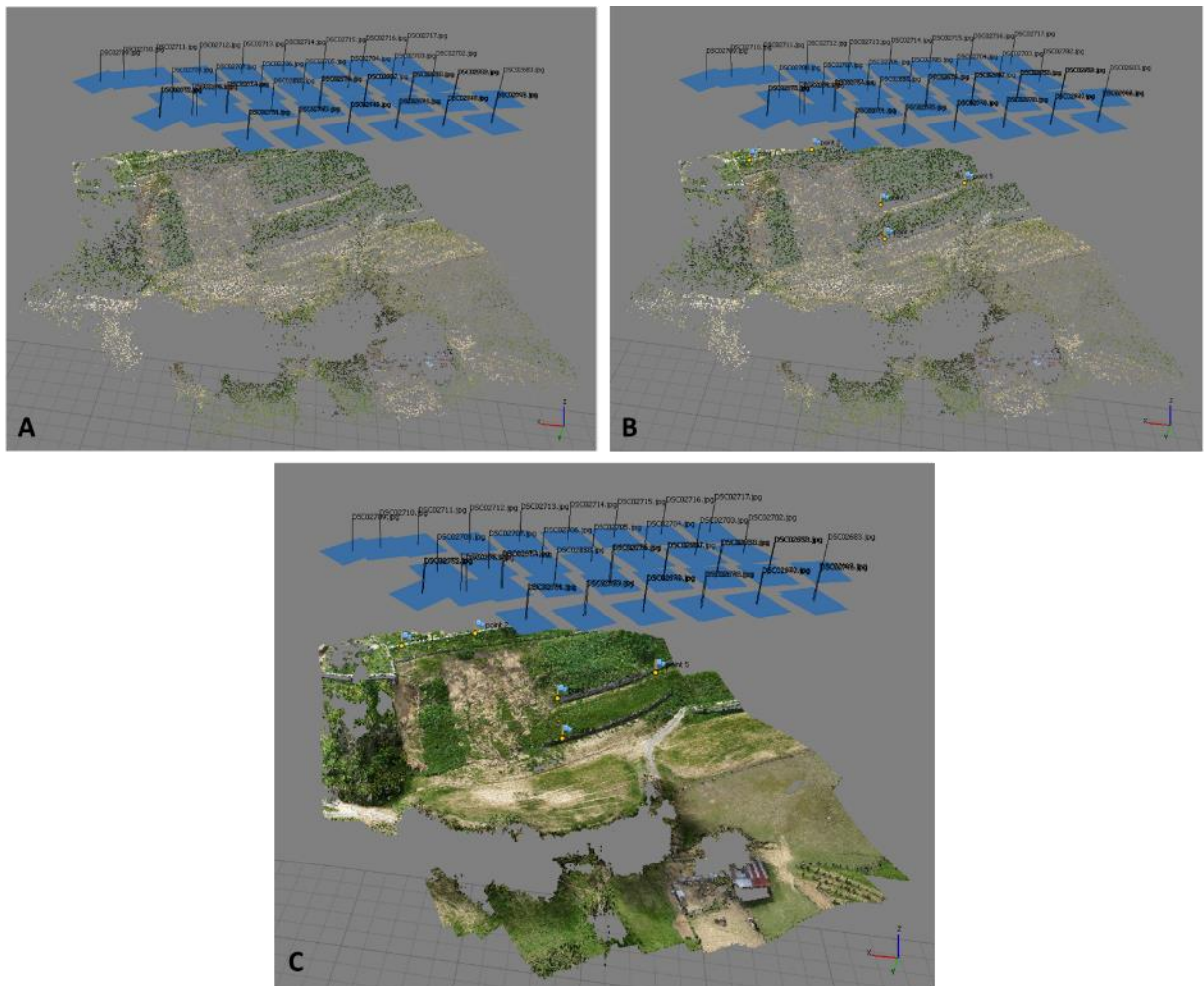
Figure 10. Main products of the digital photogrammetry processing: 3D sparse point cloud resulting from Bundle Block Adjustment (A); georeferenced 3D sparse point cloud (B); dense point cloud (C).

3. Point cloud comparison methods

Different techniques exist to analyse the space-time evolution of natural surfaces and to understand the geomorphological processes starting from point clouds data. Among a wide range of possible applications, the use of point cloud comparison to investigate the rock slope failure behaviour can be mentioned (Abellán et al., 2009; 2014; Oppikofer et al., 2009; Royan et al., 2014; Hutchinson et al., 2015) along with the evaluation of landslide displacements (Monserrat and Crosetto, 2008; Travelletti et al., 2008; Aryal et al., 2012), analysis of changes in permafrost environments (Barnhart et al., 2013) and changes in river topography (Lague et al., 2013).

The comparison procedures starting from point cloud data can be divided in two main groups (Figure 11):

i. tracking of homologous elements within consecutive point clouds to compute a displacement field;

ii. distance calculation between two point clouds when homologous elements cannot be individuated.

Comparison methods starting from point clouds

Feature tracking methods

- Oppikofer et al. (2009)
- PAM (*Piecewise Alignment Method*) method (Teza et al., 2007)
- LSSM (*Least Squares 3D Surface Matching*) method (Gruen and Acka, 2005)
- Cross-correlation method (e.g. Aryal et al., 2012; Travelletti et al., 2014)

Distance calculation methods

- DoD method (e.g. Wheaton, 2008)
- C2C (*Cloud-to-Cloud*) method (Girardeau-Montaut et al., 2005)
- C2M (*Cloud-to-Mesh*) method (Cignoni and Rocchini, 1998; Olsen et al., 2010)
- M3C2 (*Multiscale Model to Model Cloud Comparison*) method (Lague et al., 2013)
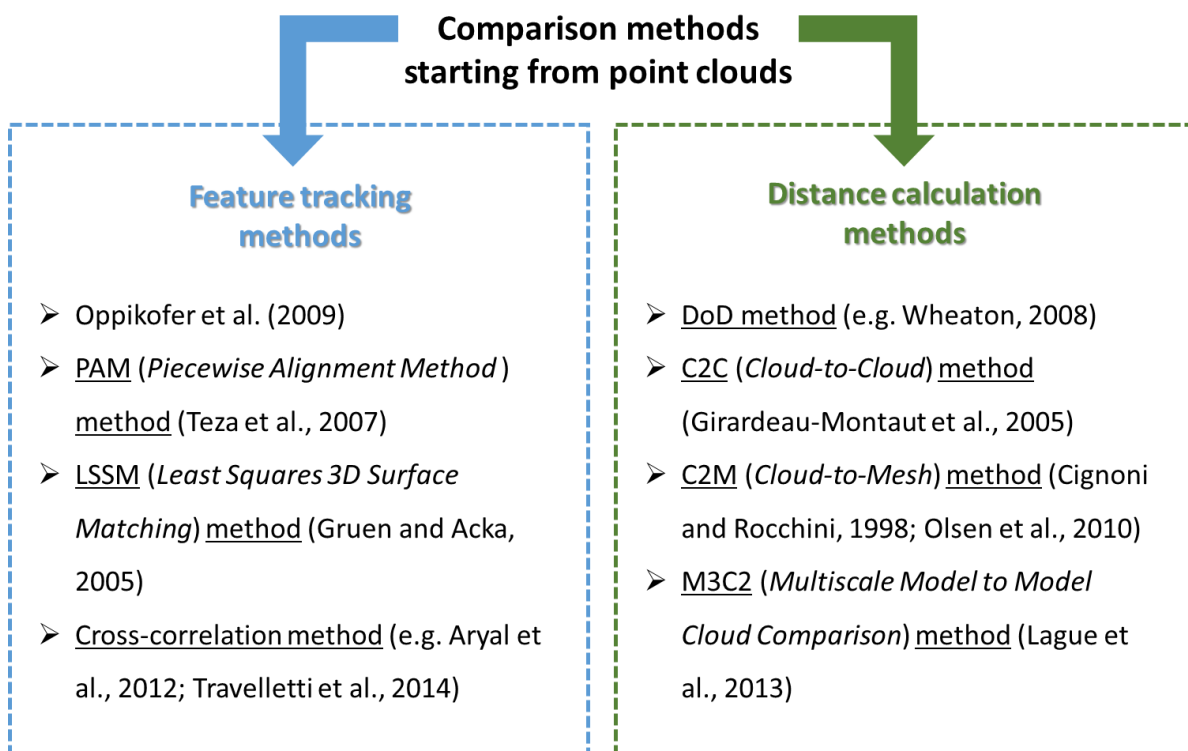
Figure 11. Main comparison methods involving point clouds.

Among the methods of the first category, Oppikofer et al. (2009) provides information on 3D displacements by analysing point pairs in successive clouds and computing the displacement vectors of selected objects. However this method present some significant drawbacks, since it is generally very difficult to track the same point in different point clouds and since the result precision depends on the point clouds resolution and on the deformation pattern of the selected objects (rigid, elastic or plastic) (Travelletti et al., 2014),.

More efficient methods are *Iterative Closest Point* (ICP) (Besl and McKay, 1992) and *Least Squares 3D Surface Matching* (LSSM) (Gruen and Acka, 2005) analyses, that permit an automatic characterization of 3D displacement field.

ICP algorithm was proposed by Besl and McKay (1992), Chen and Medioni (1992) and Zhang (1994), as surface matching in a 3D environment. The method was applied successfully to various objects (like point sets, curves and surfaces) with a common area and small differences due to noise, by minimizing iteratively the difference between them until convergence. The method is implemented for point clouds alignment purpose within the most common commercial processing software (e.g. RiSCAN PRO – RIEGL, 2010; CloudCompare - EDF R&D, 2011). The algorithm was employed with landslide monitoring purposes by Teza et al. (2007; 2008). In detail, Teza et al. (2007) presented an ICP-based *Piecewise Alignment Method* (PAM), in which the correspondence between two multi-temporal models of a landslide, acquired by TLS, is achieved by the piecewise application of the ICP algorithm with the aim to automatically compute the displacement field. This is done by computing the roto-translational matrix that describes the displacement and the rotation of an object. Unfortunately, the method can be relatively time consuming. With regard to digital photogrammetry point clouds, the method was applied in Oda et al., 2016.

The LSSM method (proposed by Gruen and Acka, 2005) estimates, given two overlapping 3D point clouds, the transformation parameters of one search surface with respect to a 3D template surface by minimizing the sum of squares of the Euclidean distances between the surfaces. Monserrat and Crosetto (2008) applied it to measure land deformation using repeated TLS acquisitions taking full advantage of the high data redundancy contained in the multi-temporal point clouds. After the global co-registration of the first and the second point clouds based on the stable areas of the scene analysed, the authors estimate the deformation parameters using a series of local matchings over scene pieces.

Another kind of technique belonging to the first category, consists in the analysis of high resolution Digital Terrain Models (DTMs) using cross-correlation functions. Initially, this was commonly employed for the analysis of optical images (e.g. White et al., 2003); its application to DTMs with natural environment monitoring purpose, was proposed by Duffy et al. (2004) to quantify the migration of submarine sand dunes using the sun-illumination values. Duffy and Hughes-Clarke (2005) indeed preferred the employment of most robust slope values to compute the displacement field. Even Daehne and Corsini (2013) used slope gradient of multi-temporal DEMs obtained from airborne LiDAR surveys, as a correlation parameter to quantify displacement and mass wasting process regarding an earthflow located in the northern Apennines in Italy, since this surface property remains often preserved during the earthflow motion.

Another example of cross-correlation applied to landslide displacement was proposed by Aryal et al. (2012): the authors made use of *Particle Imaging Velocimetry* (PIV) to correlate a set of DTMs interpolated from the original point clouds in which the data were gridded in the *xy*-plane and each *xy*-grid contains the *z*-value assigned. The approach is limited to relatively low displacement rates, because they are capable to preserve a nearly similar aspect of the raster datasets at different epochs.

Furthermore, regarding cross-correlation approaches, Travelletti et al. (2014) presented a 2D image-based correlation method to estimate the 3D displacement field with landslide monitoring purpose, taking advantage of the unique acquisition viewpoint of the multi-temporal point clouds. As for other techniques belonging to the first category, the deformation rate and the conservation of the surface morphology are the more critical factors.

When corresponding elements within successive surveys cannot be individuated, the point cloud comparison can be carried out by means of distance calculation between point data sets acquired at different times (second category, ii) (summarized in Figure 12).
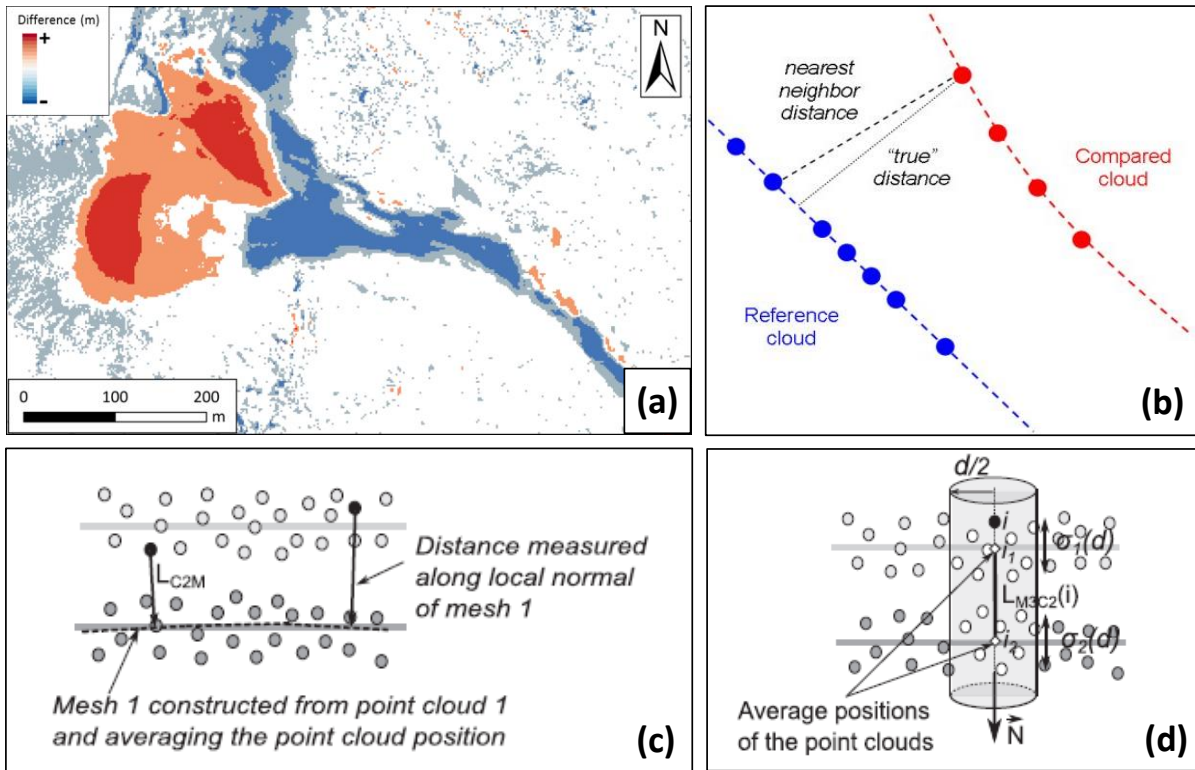
Figure 12. Main point cloud comparison methods belonging to category ii: (a) example of DEM of difference (DoD); (b) Cloud-to-Cloud (C2C) method (from: http://www.cloudcompare.org/doc/wiki); (c) Cloud-to-Mesh (C2M) method (from: Lague et al., 2013); (d) Multiscale Model to Model Cloud Comparison (M3C2) method (from: Lague et al., 2013).

The most commonly used is the conventional Digital Elevation Model (DEM) subtraction method (Figure 12a), in which the point clouds are gridded to generate two-dimensional DEMs and differentiated pixel-by-pixel, the result is a DEM of Difference (DoD).

DEMs of a surface can be considered as 2.5D models because, in those, each x, y coordinate is associated with single elevation value. DoD method allows to quantify accumulation or loss of material (Bitelli et al., 2004; Corsini et al., 2009; Prokop and Panholzer, 2009; Schürch et al., 2011) and it offers a good result when the large-scale geometry of the surface is planar (Lane et al., 2003; Milan et al., 2007; Abellán et al., 2010), but it shows some disadvantages: it provides information on changes only along the vertical direction (1D displacement) and it is not particularly suitable for overhanging parts (like rock cliffs or block faces). Furthermore, the gridding method implies a significant loss of 3D information and introduce a bias, especially in complex topography where point density and roughness may be extremely variable and occlusion can be commonplace (Schürch et al., 2011).

In this regard, the Geomorphic Change Detection (GCD) software was developed by Wheaton (Wheaton, 2008; Wheaton et al., 2010) as a plug-in for ArcGIS (www.esri.com). This tool was developed primarily for morphological sediment budget changing due to erosion and deposition on rivers (Wheaton et al., 2010; Picco et al., 2013) and it was sequentially also applied to debris flows (Scheidl et al., 2008; Theule et al., 2012; Blasone et al., 2014) and landslides (Burns et al., 2010; DeLong et al., 2012; Bossi et al., 2015). It allows an estimation of spatially variable DEM quality that is an indefinite function of survey data quality, influenced by sampling strategy, surface composition, topographic complexity and interpolation methods (Wise, 1998; Wechsler, 2003; Wechsler and Kroll, 2006). The surface representation uncertainty in the DEMs that are being compared, propagates into the DoD as (Brasington et al., 2003):

$$\delta u_{DoD} = \sqrt{(\delta z_{new})^2 + (\delta z_{old})^2} \qquad [6]$$

where δu_{DoD} is the propagated error in the DoD, and δz_{new} and δz_{old} are the individual errors in DEM$_{new}$ and DEM$_{old}$, respectively. The combined error can be computed region-by-region (Lane et al., 2003; Westaway et al., 2003) or cell-by-cell basis (Wheaton, 2008) considering a spatial variability in δz for both DEMs independently, or as a single value for the entire DoD if spatially-explicit estimates of δz_{new} and δz_{old} do not exist. The significance of DoD uncertainty can be expressed as a threshold elevation change or LoD$_{min}$ or, as an alternative, define a probabilistic threshold by means of an user-defined confidence interval (e.g. Brasington et al., 2003; Lane et al., 2003). The work introduces a spatially variable model of elevation uncertainty based on a fuzzy inference system (FIS) and the application of a spatial contiguity index to account for the spatial coherence of deposition and erosion units.

Because the DEM difference method remains limited to 2D surface, 3D point cloud comparison has become a widely investigated method in Earth Sciences environment. The simplest and high-speed method is the direct *Cloud-to-Cloud* (C2C) comparison (Figure 11b) with closest point technique (Girardeau-Montaut et al., 2005). The technique consists in computing for each point of the first cloud, the closest point in the second one and calculating the shortest distance (Hausdorff distance - Girardeau-Montaut et al., 2005). The method provides a rough comparison between two clouds and it often do not return signed distances, but, in the case of landslide investigation, it can be a rapid useful tool when the direction of movement is unknown (Travelletti et al., 2008). Improvements can be obtained by a local

model (e.g. Height function, Least squares plane, 2D ½ triangulation) of the reference cloud such as possible in the *CloudCompare* software (EDF R&D, 2011).

Another approach to perform change detection of multi-temporal point clouds is to compute *Cloud-to-Mesh* (C2M) distances (Figure 12c) (Cignoni and Rocchini, 1998; Olsen et al., 2010). This method is the most common technique in point cloud processing software packages (e.g. RiSCAN PRO - RIEGL, 2010; PolyWorks; the open source software CloudCompare - EDF R&D, 2011). In this case, the morphologic changes are highlighted and measured by computing the distance between a point cloud and a reference 3D mesh, obtained triangulating (e.g. using Delaunay triangulation) a cloud acquired in a different epoch. The approach is more suitable for nearly flat surfaces (such as rock cliff; e.g. Abellán et al., 2009; 2010) for which the processing of the data causes minor loss of information. However, generating a surface mesh is not simple for point clouds with significant roughness or missing data due to occlusion and shadow zones and can introduce uncertainties, as for the gridding methods in the DEM difference technique. For these reasons, in particular for complex topography, the C2M method commonly requires time-consuming manual examination.

In recent years, Lague et al. (2013) developed *Multiscale Model to Model Cloud Comparison* (M3C2) method (Figure 12d). The algorithm uses a set of calculation "core" points to calculate signed distances between two point clouds along the normal direction. The core points will generally be a sub-sampled version of the reference cloud, but all calculations use the original raw data.

A normal vector is defined for any given core point fitting a plane to the neighbours of the first cloud that are within a radius D/2 of that core point. The standard deviation of the distance of the neighbours to the best fitting plane is recorded and used as a measure of the cloud roughness $\sigma(D)$ at scale D in the vicinity of core points. This normal is used to position a cylinder inside which equivalent points in the other cloud will be searched for; the diameter of this cylinder is called projection scale d. All elements in both point clouds located in the cylinder are spatially averaged to compute mean surface positions along the normal direction in each point clouds. The distance between these two average distributions is the local distance between the two clouds and the two standard deviations give a local estimate of the point cloud roughness $\sigma(d)$ along the normal direction ('apparent' roughness) (Lague et al., 2013).

A confidence interval, taking the cue from DoD method (Wheaton et al., 2010), allows to estimate the distance uncertainty accuracy, based on the registration error, the local point cloud roughness measured along the normal direction and point uncertainty. The user can input the error associated with the registration of two point clouds to common coordinate system and it will be take into account during the computation of the significant change map. It's important remembering that the registration won't be generally isotropic (Bae & Lichti, 2008) and spatially uniform.

The normal scale D and the projection scale d are specified by the user. D is based on point cloud density and local roughness: Lague et al. (2013) notes that to verify that the normal orientation is unaffected by smaller scale roughness at the chosen scale, D should be at least 20 to 25 times larger than the roughness $\sigma(D)$; even if it must be small enough to capture large scale modification.

The local roughness $\sigma(d)$ of each point cloud depends on the real surface roughness, the exact orientation of the normal with respect to the considered cloud and instrument related noise (Lague et al., 2013).

4. Matlab tool

The proposed semi-automatic analysis tool is composed of two different routines (Figure 13), which can be run separately:

i. Routine 1: given a point cloud chosen as *reference* data set and a point cloud chosen as a *compared* one (both in geographic coordinate system), firstly the tool performs an analysis on the *reference* cloud to investigate the morphometric characteristics of the acquired 3D surface; secondly, it permits to carry out a comparison between the two clouds computing the distance values along the local normal.

ii. Routine 2: once defined the Level of Detection and identified the significant distances, a cluster analysis allows to automatically extract the sub-clouds characterized by significant distances and compute their area.
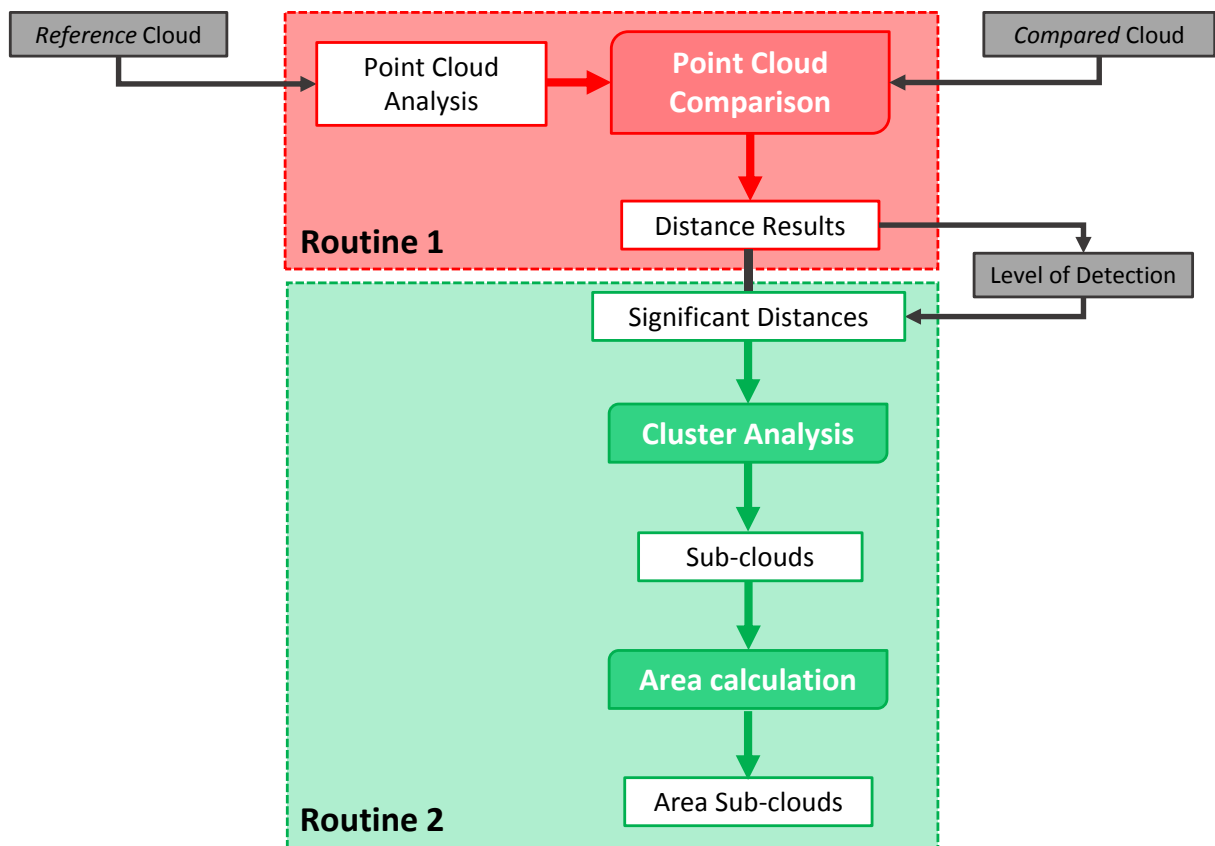

Figure 13. Schematic flow chart of the proposed framework.

4.1 Routine 1

4.1.1 Factors influencing the change detection

4.1.1.1 Terrestrial Laser Scanning technique

The factors controlling the laser scanning point cloud change detection results involve systematic and random errors, that influenced the accuracy and precision of the measurements, respectively (see paragraph 2.1.1). Frequently, the quality of involved point cloud data is already strongly variable within one point cloud (Soudarissanane et al., 2011). Among the main uncertainty sources there are: errors intrinsic to the instrument (Reshetyuk, 2006; Pirotti et al., 2013); survey design and methodological errors such as object-scanner distance (that, in its turn, influences the resolution and the laser beam footprint, see paragraph 2.1.3), incidence angle (more details in aforementioned paragraphs), atmospheric conditions (Beckmann, 1965), alignment and registration uncertainty (Lichti et al., 2005; Oppikofer et al., 2009; Teza et al., 2007), point density variation; object factors such as vegetation, surface reflectance (Pesci et al., 2008) and roughness (Schurch et al., 2011; Lague et al., 2013). As a result, the noise level in a point cloud is different for each single point.

An in-depth analysis of the error sources in the measurements with pulsed time-of-flight TLS is available in Reshetyuk (2006).

Analysing these errors in detail, the terrain roughness due to the complex topography can cause local occlusion bias in the point cloud. Furthermore, an artificial roughness resulting from survey design errors, such as the difficulty to reoccupy the same scanning position between surveys and position uncertainty, can also occur (Hodge, 2010; Schürch et al., 2011; Barnhart & Crosby, 2013; Lague et al., 2013). This factor influences also the computation of the surface normal orientation (Mitra and Nguyen, 2003; Lalonde et al., 2005).

Roughness along with instrumental errors contribute to random noise. Because this factor is normally distributed, it can be reduced by means of averaging. Until now, two possible averaging approaches were applied to raw point cloud data: those concerning the averaging of the point cloud position (such as M3C2, Lague et al., 2013) and those involving the averaging of distances between point clouds, in spatial domain (such as Abellán et al., 2009; Royán et al., 2014) or in spatial and temporal domain (Kromer et al., 2015).

Regarding occlusion (shadow), it happens when the laser beam is obstructed and not able to hit the object or when some surfaces are semi-parallel to laser beam (that is the incidence angles is highly oblique to the surface), therefore some portions of the observed area result hidden. The occlusion effect can induce artificially surface changes in points adjacent to occlusion itself (Girardeau-Montaut et al., 2005; Zeibak and Filin, 2007; Lague et al., 2013). The dense vegetation with large leaves can also hide parts of the investigated surface, the situation can be improved acquiring multiple scans or using a laser scanner that records numerous numbers of echo. Generally, the presence of vegetation creates a noisy point cloud but, if it is not much dense and discernible from ground data, it can be removed.

The quality of the measurements even depends on atmospheric conditions (temperature, humidity, ambient light and so on) as a function of the laser wavelength in use. Therefore, laser beam can be attenuated, distorted or deviated (Soudarissanane, 2016).

The point density decreases with increasing distance to the scanner and local variations in point density affect the comparison results, in particular concerning C2C comparison. This error makes it difficult to distinguish real changes from differences induced by noise (Lague et al., 2013).

Among the uncertainty source, the process of registration and/or georeferencing adds to the error budget. Moreover, system calibration and errors in the positioning of the sensor, contribute to systematic errors that could lead to false change detection.

As opposed to random noise, that could be removed by the averaging, systematic errors cannot be eliminated with statistical techniques. This kind of error depends on the method to georeferenced the clouds, the number of the stations used in a survey and the instrumental characteristics (Lichti et al., 2005; Bae and Lichti, 2008; Olsen et al., 2011) and they can be removed by means of self calibration (Lichti and Skaloud, 2010); however, an effective survey design must be pledged. In the case of practical application, the definition of a suitable level of detection (see paragraph 4.2) based on the analysis of the comparison data where no changes have occurred (Abellán et al., 2009; Kromer et al., 2015), can help to neglect not reliable change results.

4.1.1.2 UAV Digital Photogrammetry technique

The three-dimensional point cloud yielded by multi-view stereopsis technique and consequently, the comparison between point clouds, can suffer from variable vegetation cover and texture, strong topographic relief, occlusions, illumination changes and acquisition geometry (Remondino et al., 2006; Harwin and Lucieer, 2012), in particular in the case of complex natural environments.

The point clouds generated by UAV images processing have the limitation that these do not represent the ground in the landscape where the vegetation is dense and complex (e.g. bushes with many overlapping branches) and when the surface has a homogeneous texture (e.g. water or a tin roof), as these results in gaps or sparse areas in the cloud (Harwin and Lucieer, 2012). Compared to LiDAR clouds, this technique does not penetrate the dense vegetation. For this reason, the effects of the vegetation could be not reliably removed (Remondino et al., 2006; Dandois and Ellis, 2010). Furthermore, automatic image matching methods for surface reconstruction or tracking points suffer from the presence of vegetation (Scaioni et al., 2014).

Comparing with terrestrial laser scanner products, in the nadir UAV-acquired images shadowing effects due to the oblique view point of ground-based platform are minimised (Niethammer et al., 2012).

The systematic errors convolving the generated point clouds depend on adjustments performed in triangulation phase (bundle adjustment process) (Oda et al., 2016) but even on georeferencing technique (Turner et al., 2012), as about laser scanner point cloud.

The density, sharpness, and resolution of the photoset, combined with the range of natural scene textures will determine, in the first instance therefore, the quality of the output point cloud data (Westoby et al., 2012).

4.1.2 Approach

Taking the cue from the M3C2 method (Lague et al., 2013), the approach presented in this thesis is based on the computation of the distances, along the local surface normal, between pair of point clouds acquired in different epochs. Since the tool works directly on the point cloud, no data structuring (triangulation or approximation) is required. The point cloud comparison along a local normal has been employed in different geomorphological studies (Lague et al., 2013; Barnhart and Crosby, 2013; Kromer et al., 2015; Fey and Wichmann, 2016).

As highlighted by Lague et al. (2013), the geomorphic processes tend to depend on surface geometry.

The local normal is defined for each point of the *reference* point cloud (it can be the first point cloud i.e. the first data acquisition, or the second one) by fitting a plane to the neighbouring points within an user-defined search neighbourhood cube half-side *R* centred on that point, thus for each group of choose points, a cluster is defined. The point cloud used for the comparison is called *compared* point cloud.

The dimension of the cube half-side depends on the point density and the roughness and geometry of the scenario. In particular, the local normal should be unaffected by smaller scale roughness at the chosen scale, but small enough to capture large-scale modification. In the case of complex topography, the choice of the scale at which the normal should be evaluated is particularly important.

4.1.2.1 Point cloud analysis

The point cloud analysis allows to quantitatively characterize the *reference* point cloud from the morphological point view, extracting the main morphometric indices, which in this case are azimuth, inclination and roughness of the surface. Furthermore, also the density of the points in the point cloud is evaluated. These parameters are obtained from the calculation of the best fitting plane given a set of points included within the search neighbourhood cube, without significant loss of information.

The best fitting plane, according to the least squares method, is found by applying the *Singular Value Decomposition* (SVD) (Golub and Reinsch, 1970; Golub and Van Loan, 1980; Golub and Van Loan, 1996; Demmel, 1997; Lay 2002) MATLAB function. The function allows transforming correlated variables into a set of uncorrelated ones that better express the relationships between the original data items reducing them to a lower dimensional space and permitting to identify the dimensions along which data points show the most variation. The function is usually applied for image processing (Muller et al., 2004), point cloud segmentation and geomechanical features extraction (Ferrero et al., 2009; Gigli and Casagli, 2011) purposes.

Basing on a theorem from linear algebra, let A be a real rectangular m x n matrix, it can be broken down into the product of three matrices (*matrix factorization*) (Figure 14):

$$A_{mn} = U_{mm} \, S_{mn} \, V_{nn}^T \qquad\qquad [7]$$

where U is an orthogonal matrix and its columns are orthonormal eigenvectors of AA^T (called *left-singular vectors* of A); S is a diagonal matrix containing the square roots of the non-zero eigenvalues (also called *singular values* of A; they are always real and nonnegative even if A is complex) from U or V in descending order; V is the transpose of an orthogonal matrix and its columns are orthonormal eigenvectors of $A^T A$ (called *right-singular vectors* of A); and $U^T U = V^T V = VV^T = I$.

If A has many more rows than columns ($m > n$), U can be quite large, but most of its columns are multiplied by zeros in S. In this circumstance, the *economy-sized* or *reduced* decomposition produces an U_{mn}, an S_{nn} and the same V, saving both time and storage (www.matlab.com) (Figure 14).
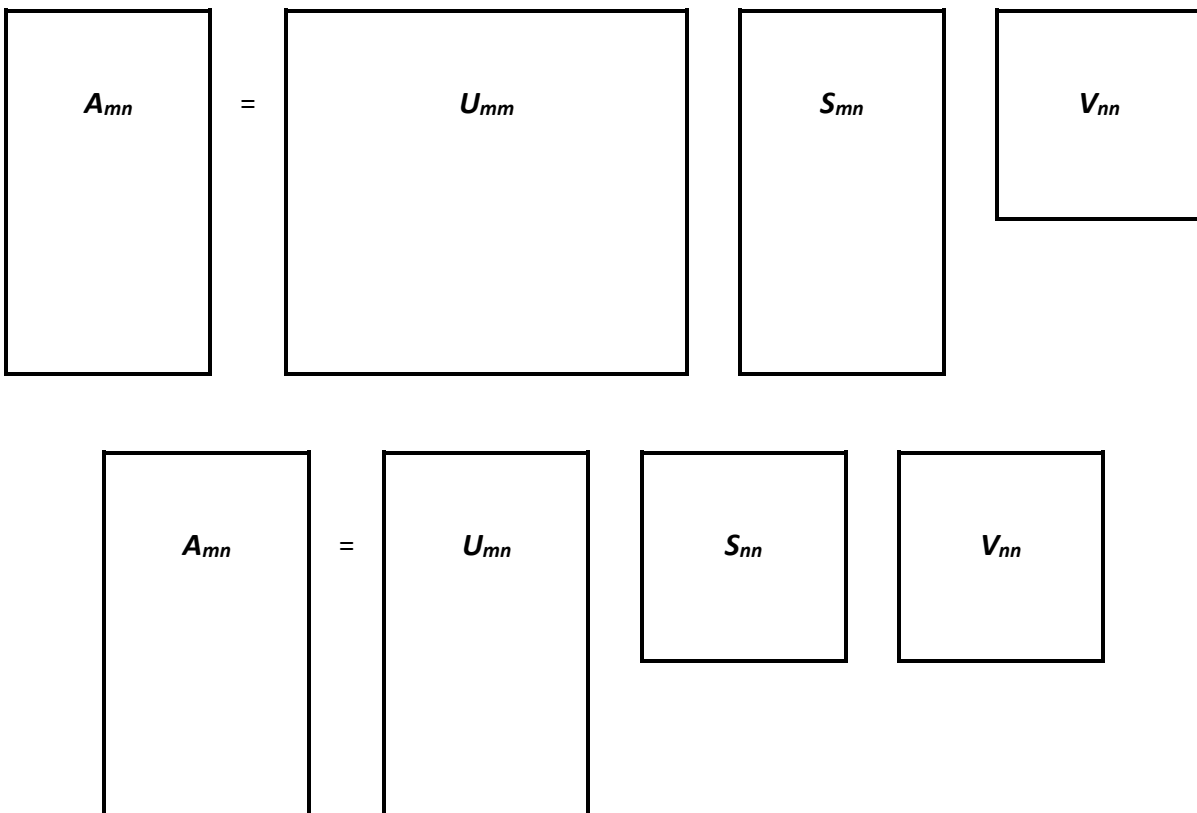

Figure 14. Full (top) and economy (bottom) Singular Value Decomposition of an mxn matrix.

Applications of the SVD include solving least squares problems. The linear least squares problem has the general form as $Ax \approx b$ where A is a rectangular *m* x *n* matrix with $m \geq n$ the vector $\bar{x} \in \mathbb{R}^n$ is the least square solution such that

$$\| \, b - A\bar{x} \, \| \leq \| \, b - Ax \, \| \qquad\qquad [8]$$

for each $x \in \mathbb{R}^n$.

According to another theorem from linear algebra, $\bar{x}$ is a least square solution of $Ax \approx b$ if and only if $\bar{x}$ is a solution of normal equation system

$$A^T A \bar{x} = A^T b \qquad\qquad [9]$$

and if A has linearly independent columns (that is the rank of A is maximum), the solution that minimizes the sum of the square differences between the left and the right sides is unique and it is

$$\bar{x} = (A^T A)^{-1} A^T b \qquad\qquad [10]$$

the matrix $A^+ = (A^T A)^{-1} A^T$ is defined the pseudoinverse of A. Therefore, the least square solution is

$$\bar{x} = A^+ b. \qquad\qquad [11]$$

The solution of the least square problem can be resolved with the singular value decomposition in the following way:

$$A^+ = V S^+ U^T. \qquad\qquad [12]$$

This means that the solution of the least squares problem is given by the matrix of eigenvalues ($\lambda \in S$) and the matrix of the eigenvectors ($v \in V$) of the $A^T A$ matrix. In particular, the solution $\bar{x}$ that minimizes the least squared error is given by the eigenvector v_n of the $A^T A$ matrix corresponding to the smallest singular value $\lambda_{\min}$. Therefore, the eigenvector v_n provides the planar parameters like direction cosines which define the direction of maximum slope of the plane (Figure 15a).

The above is correct only if A is centred. Therefore, for each cluster, the centroid is calculated and the points within the cluster are shifted to the centroid.

The plane is defined by its direction cosines (m, l, n) and has a general equation of the type

$$ax + by + cz + d = 0 \qquad\qquad [13]$$

The associate plane orientation, such that the polar coordinates α (azimuth – the clockwise angle with respect to North direction and it varies between 0 to 360°) and β (inclination – that

is the angle between a horizontal plane and the considered plane and it varies between 0° to 90°) (Figure 15b), are found by applying the following equations:

$$\alpha = arctan\left(\frac{m}{l}\right) + Q \qquad\qquad [\ 14\ ]$$

$$\beta = arctan\left(\frac{n}{\sqrt{l^2+m^2}}\right) \qquad\qquad [\ 15\ ]$$

where m, l and n are the direction cosines along x-axis, y-axis and z-axis, respectively; Q is a constant, which assumes the next values: $Q = 0°$ if $l > 0$ and $m > 0$; $Q = 360°$ if $l > 0$ and $m < 0$; $Q = 180°$ if $l < 0$ and $m < 0$ or if $l < 0$ and $m > 0$. In the global coordinate reference system, the y-axis represents the North direction.
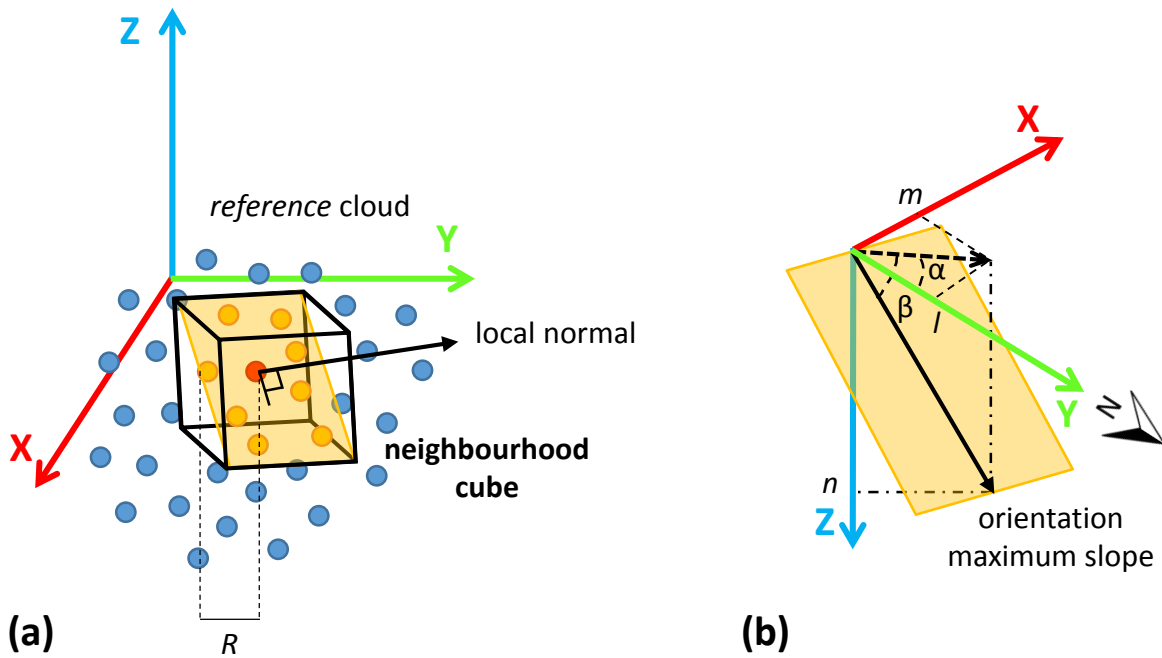

Figure 15. Schematic representation of the neighbourhood cube (a) and of the plane orientation (b).

The residual distances of the neighbour points to the fitted plane are calculated multiplying the left-eigenvector ($u \in U$) corresponding to the smallest singular value by the smallest singular value λ_{min}. Then the standard deviation (σ) of the selected points concerning the best fitting plane is calculated. The standard deviation is used as a measurement of the local roughness at scale R around the selected points (e.g. Rychkov et al., 2012, Lague et al., 2013) (Figure 17). Furthermore, for each cube-cluster the point density is calculated (Figure 17).

4.1.2.2 Point cloud comparison

Once the normal vector is defined for each *reference*-cluster, a subset of points in the *compared* cloud (called selection-cluster) is selected for each point of the *reference* cloud; it is equivalent to intercepting a parallelepiped whit a quadratic base of size 2*r* (the user-defined selection base half-side *r* is equivalent to the projection scale of M3C2) and axis equal to normal vector defined for each cube-cluster (Figure 16). This is done by roto-translating the *compared* cloud about the selected point of the *reference* cloud in the local coordinate reference system of the defined cluster. The rotation is a combination of a rotation around a z-axis by β angle [16] and a rotation about *x-y* plane by α angle [17].

$$Rot1 = \begin{bmatrix} cos\,\alpha & -sin\,\alpha & 0 \\ sin\,\alpha & cos\,\alpha & 0 \\ 0 & 0 & 1 \end{bmatrix} \qquad [\,16\,]$$

$$Rot2 = \begin{bmatrix} 1 & 0 & 0 \\ 0 & cos\,\beta & -sin\,\beta \\ 0 & sin\,\beta & cos\,\beta \end{bmatrix} \qquad [\,17\,]$$

The result is a selection-cluster in the *compared* cloud, on which the position of the barycentre is computed. The maximum length of the parallelepiped is defined by the user to speed up the calculation (as in Lague et al., 2013).

The distance between each point of the reference cloud and the barycentre of the corresponding selection-cluster is calculated through plane-point distance along the normal vector of the *reference* cluster. Distances in the same direction as the normal vector are positive; on the contrary, negative distances indicate differences in the opposite direction from the normal.

With the aim to establish a sign convention for the local normal vectors, the semi-space including the sensor position is chosen. In this way, the distance value along the normal vector is oriented positively towards upward direction and negatively in downward direction.

The sign (positive or negative) of the resulting distance depends on the chosen of the *reference* cloud: if the point cloud corresponding to the first survey is selected, negative distances show loss in the material, depletion or detachment zones and positive ones are related to material accumulation or precursory deformation (Kromer et al., 2015); otherwise, if the cloud corresponds to the second data acquisition, negative and positive distances indicate the contrary.

The distances projected along *x*-axis, *y*-axis and *z*-axis are also computed (Figure 17) to evaluate the different components of the change.
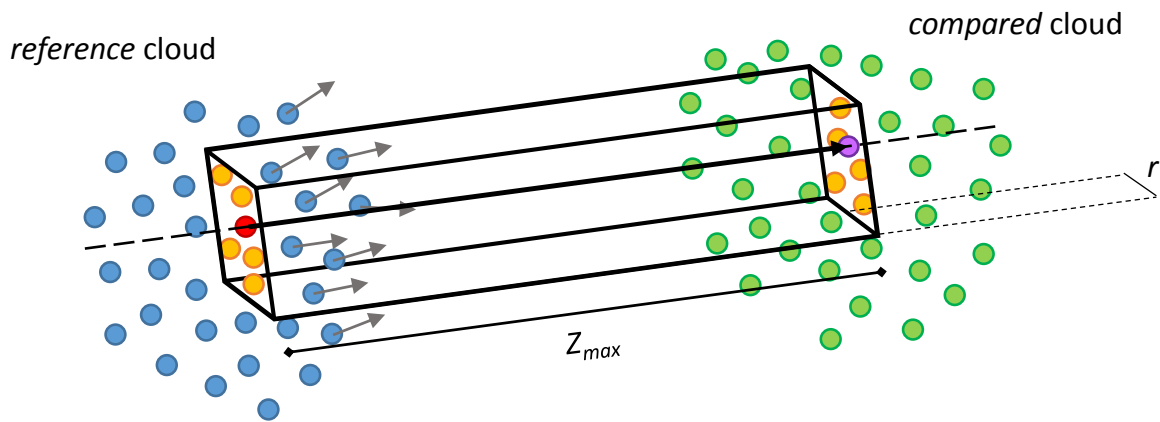

Figure 16. Schematic representation of the point clouds comparison.

As highlighted in several works (Abellán et al., 2009; Lague et al., 2013; Royán et al., 2014; Kromer et al., 2015), the averaging approach is useful to reduce random Gaussian noise or artificial roughness, usually resulting from a combination of instrumental error and surface roughness (see paragraph 3.1.1), and to take into account the information contained in neighbouring points. The highest is the point density in the neighbourhood of the selected point, the best is the result.

In this work, a spatial averaging of the distances is chosen using an average cube half-side R_a defined by the user. The result is an average distance along the local normal (Figure 17).

In conclusion, for each point of the *reference* point cloud, the computed features are reported as attributes and saved as a .txt file readable in commonly 3D point cloud processing software, such as the open source software CloudCompare (EDF R&D, 2011).
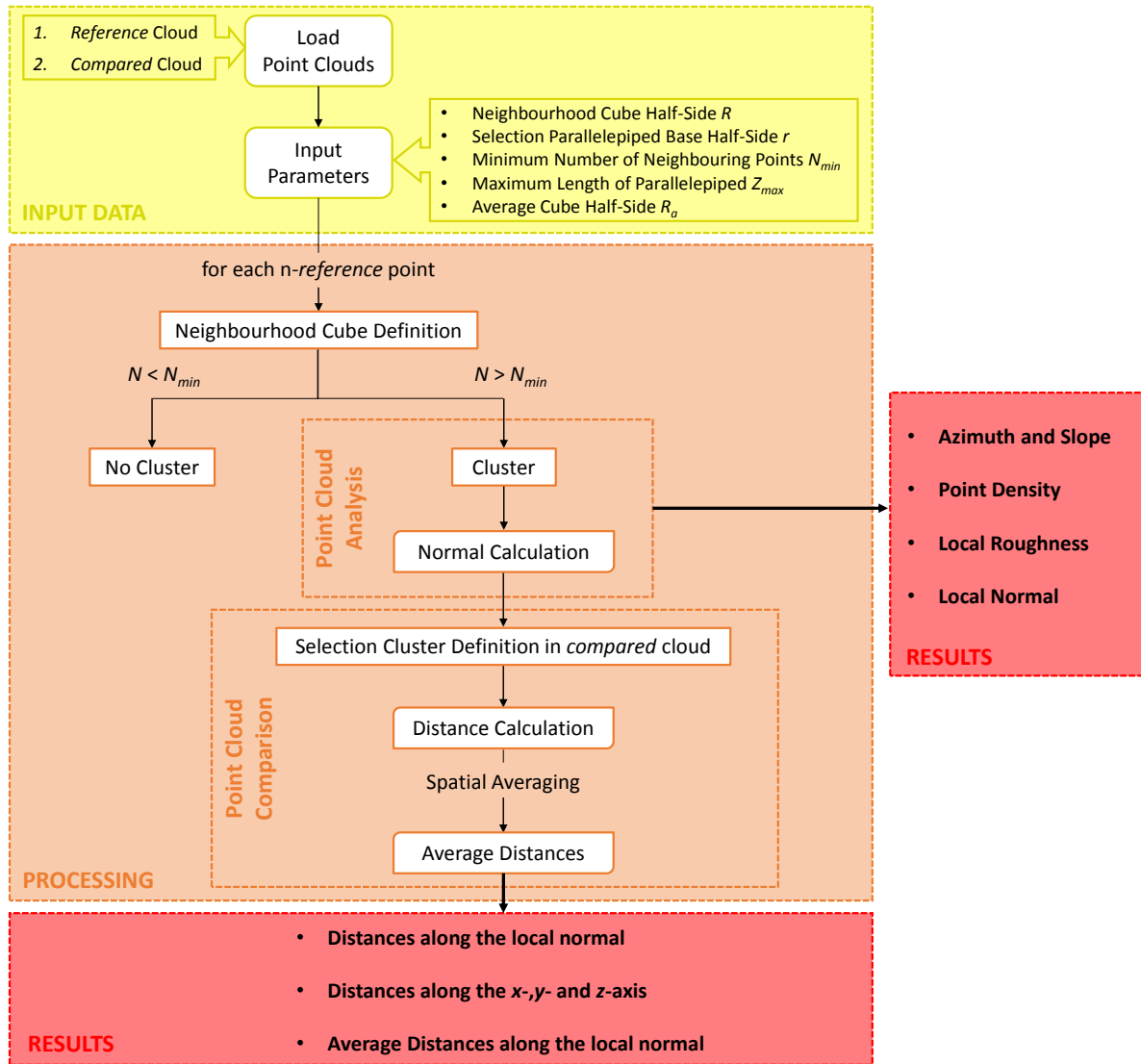
Figure 17. Flow chart of Routine 1.

4.2 Level of Detection

The Level of Detection (usually indicated as LoD acronym) is the minimum threshold differentiating real changes from data noise, over this value the signal-to-noise ratio is supposed to be plus than one. As already treated in the paragraph 3.1.1, among the point cloud comparison uncertainties, position and registration errors and uncertainties related to the surface roughness are the main ones.

The threshold can be selected according to errors in data collection and processing and to uncertainty sources connected to survey or characteristics of the scenario. For example, Lague et al. (2013) that constructed the LoD inspired by the DoD technique (see chapter 3) defining a spatially variable confidence interval related to each measurement. The approach take into account the spatially variable local point cloud roughness and the registration error as isotropic and uniform. Whereas Fey and Wichmann (2016) also considered the positional uncertainty in the error budget calculation.

Either way, it is important to remember that the position and registration uncertainties cannot be easily modelled (Soudarissanane et al., 2011; Bae and Lichti, 2008).

The threshold is even typically set using a confidence interval based on the differences deriving from the point cloud comparison in data collected on the areas considered stables during the monitoring period, such as in Abellán et al. (2009) and Kromer et al. (2015).

In both threshold evaluation procedures, LoD is based on a confidence interval at 95%.

In the context of this thesis, the choice of the LoD was evaluated on a case by case basis as a function of the considered instability phenomena and characteristics of the scenario.

4.3 Routine 2

4.3.1 Cluster analysis

Once defined LoD value, the algorithm extracts the points characterized by significant distances (negative and positive) and successively a cluster analysis for both negative and positive subset can be performed to automatically segregate them. The cluster analysis allows grouping the statistical units of a population basing on similarities among the individual data.

The cluster analysis technique used for this routine (Figure 18) is a kind of agglomerative hierarchical clustering, in which the minimum Euclidean distance (*minDist*) between the points (*xyz* location) respect to the mean of the smallest distances (*mean(minDist)*) are chosen as measure of dissimilarity. Therefore, first of all the proposed algorithm computes the Euclidean distance between an arbitrary point of the cloud (in this case the first one was chosen) and the other points. Later, the minimum distance (*minDist*) is calculated. If the *minDist* is lower than *mean(minDist)* multiplied by a user-defined factor *F*, the algorithm labels each point as belonging to *cluster n*, on the contrary the point is labelled as belonging to a new cluster (*cluster n+1*) (Figure 19). Therefore, each point of the point cloud characterized by distance values over the chosen level of detection, is labelled as belonging to a cluster (or sub-cloud).

In the case of the point cloud corresponding to the first survey is selected as the *reference* one, the resulting positive sub-clouds represent deformation zones or areas characterized by accumulation of material; obviously in the case of steep rock face, positive sub-clouds cannot indicate material accumulation zones. On the other hand, the negative sub-clouds represent areas characterized by the depletion or detachment of material.
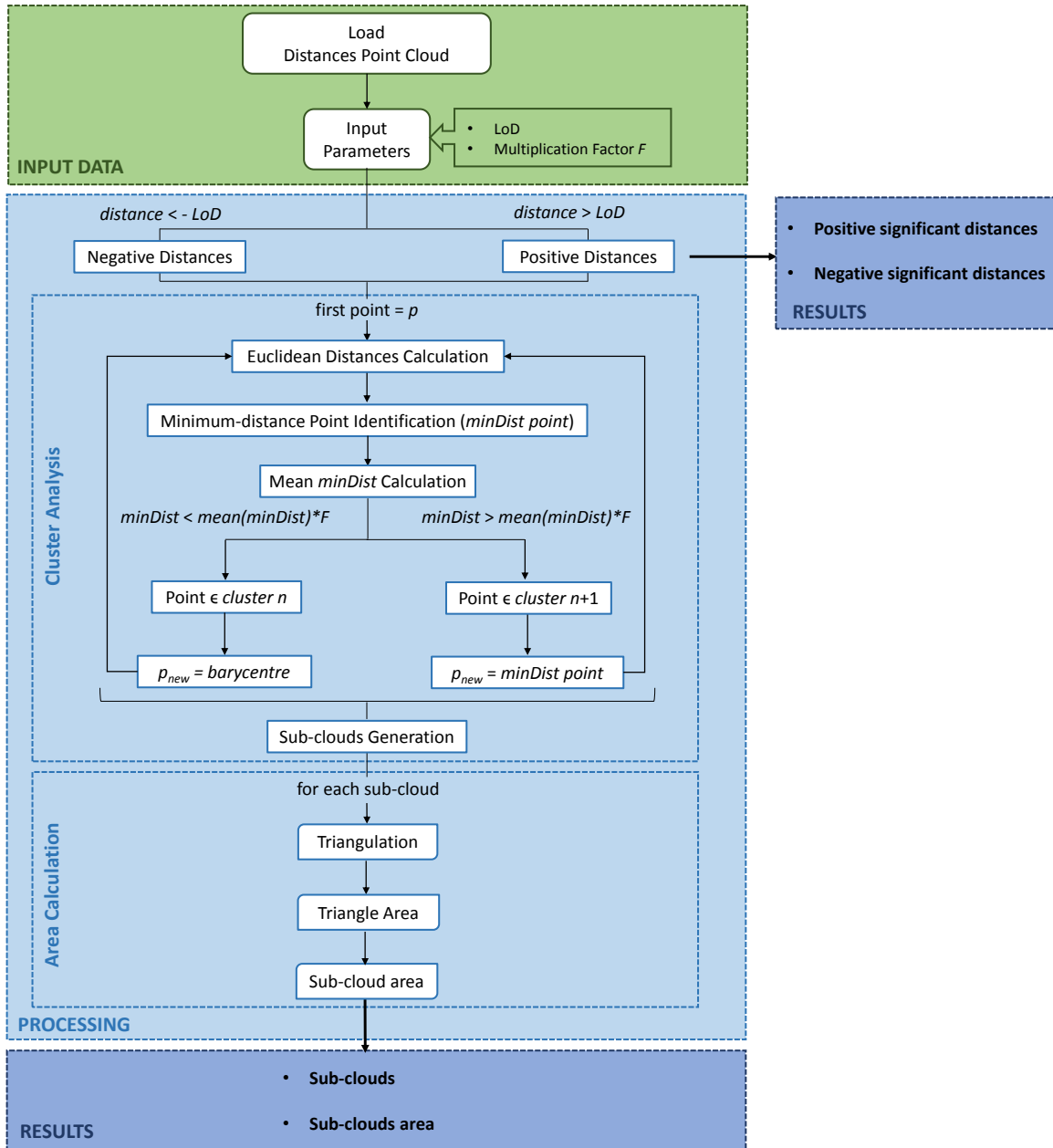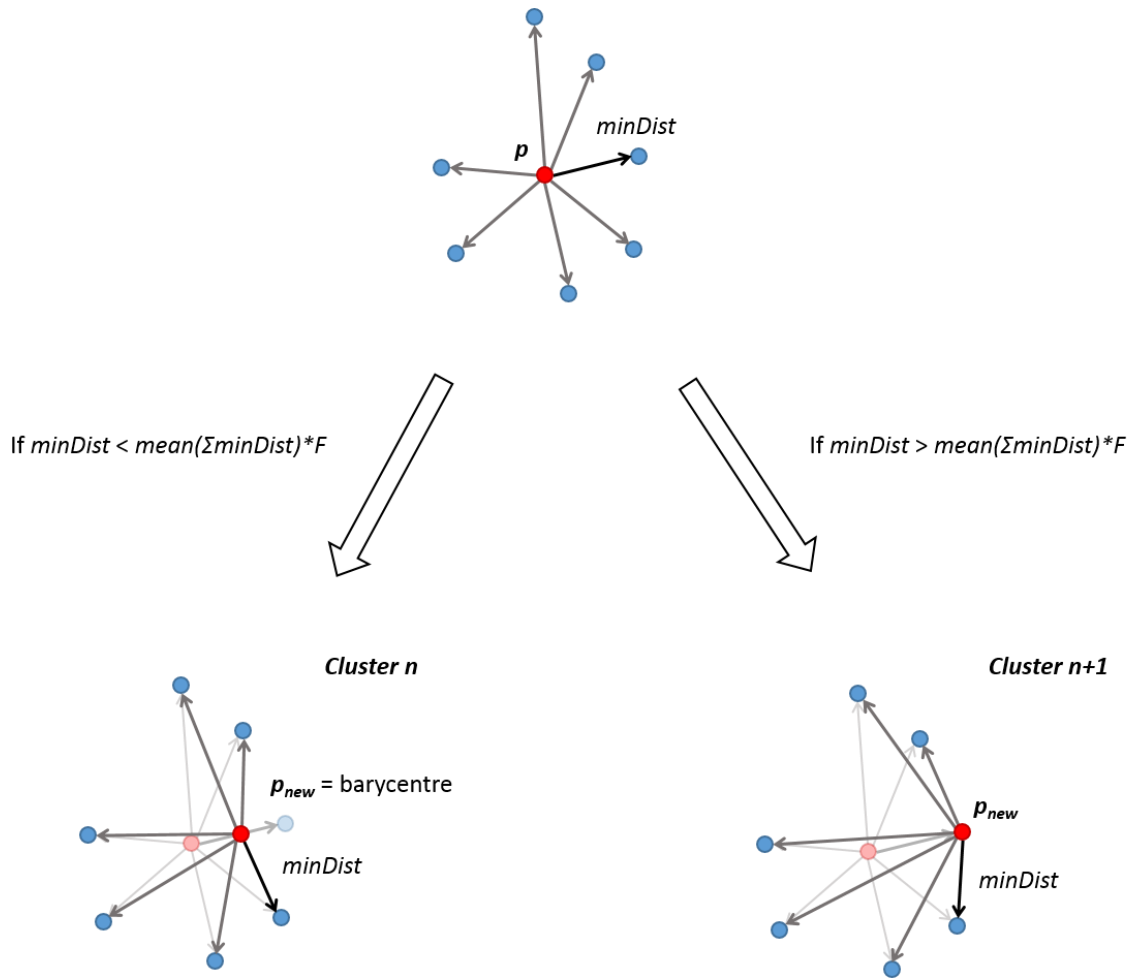
Figure 18. Flow chart of Routine 2.

Figure 19. Cluster analysis schematic process.

4.3.2 Area calculation

Once sub-cloud generation is performed (Figure 18), for each of them, the polar coordinate α and β ([14] and [15]) through SVD function (see paragraph 4.1.2.1) is computed shifting the points within the cluster to its centroid. Therefore, for each sub-cloud, the routine applies a combination of rotation counter-clockwise around a z-axis by β angle [16] and a rotation counter-clockwise about *x-y* plane by α angle [17] changing the coordinate system of the sub-cloud to local. Therefore, the points of the sub-cloud will result in the new coordinate system, where the new origin *O'* coincides with the centroid of the sub-cloud and the new *x'* and *y'* axes coincide with the main plane parameter axes.

Successively, the *Convex Hull* (Preparata and Hong, 1977) MATLAB function (www.matlab.com) is applied to points within the sub-cloud. The convex hull of a set of points *X* in *n* dimensions is the intersection of all convex sets containing *X* or the smallest convex set that contains *X*; it is given by the expression:

$$Conv(X) = \left\{ \sum_{i=1}^{|X|} \alpha_i x_i \,\middle|\, (\forall i: \alpha_i \geq 0) \wedge \sum_{i=1}^{|X|} \alpha_i = 1 \right\} \qquad [\,18\,]$$

the convex hull of a finite point set $X \subset \mathbb{R}^n$ forms a convex polygon when n=2; each point x_i in *X* that is not in the convex hull of the other points is called a vertex of *Conv(X)*.

In the case of this approach, the convex hull function is applied to the sub-clouds in 2D dimensions to obtain the "hull" in the *x'-y'* plane. Consecutively, Delaunay Triangulation is automatically employed to triangulate the set of points of each sub-cloud in the two-dimensional space. Therefore, the area for each constructed triangle is computed by Heron's formula (Dunham, 1990), given the lengths of the sides *a*, *b* and *c* and the semiperimeter *s* by requiring no arbitrary choice of side as base or vertex as origin.

$$A = \sqrt{s(s-a)(s-b)(s-c)} \qquad [\,19\,]$$

The lengths of the sides *a*, *b* and *c* are calculated by Euclidean distance. Once computed each triangle area, the tool adds together the several areas to calculate the area of the sub-cloud.

In conclusion, the final output of the routine is a database including the number of recognized zones, the area of these sectors and, for every zone, it provides the features obtained from the point cloud analysis and comparison (that is azimuth, slope, local normal vector, roughness, point density, distance along the local normal, distance along the x-, y- and z-axis).

5. Test sites

5.1 San Leo test site

The San Leo rock mass is located in the northern Appennines, on the right side of the mid Marecchia River valley, in the SE sector of the Emilia Romagna region (Figure 20). The town lies at about 650 m a.s.l, at the top of a slab of about 0.3 km² in extension, bordered by vertical and overhanging cliffs up to 100 m high. The site is delimited on the west, north and south sides respectively by creek valleys of small tributaries of the Marecchia River (Figure 20A). The geomorphology of the rock plate resembles a "cuesta", with the highest elevation towards east, where the renowned medieval fortress is located, and sloping toward west, where the downtown developed (Borgatti et al., 2015).
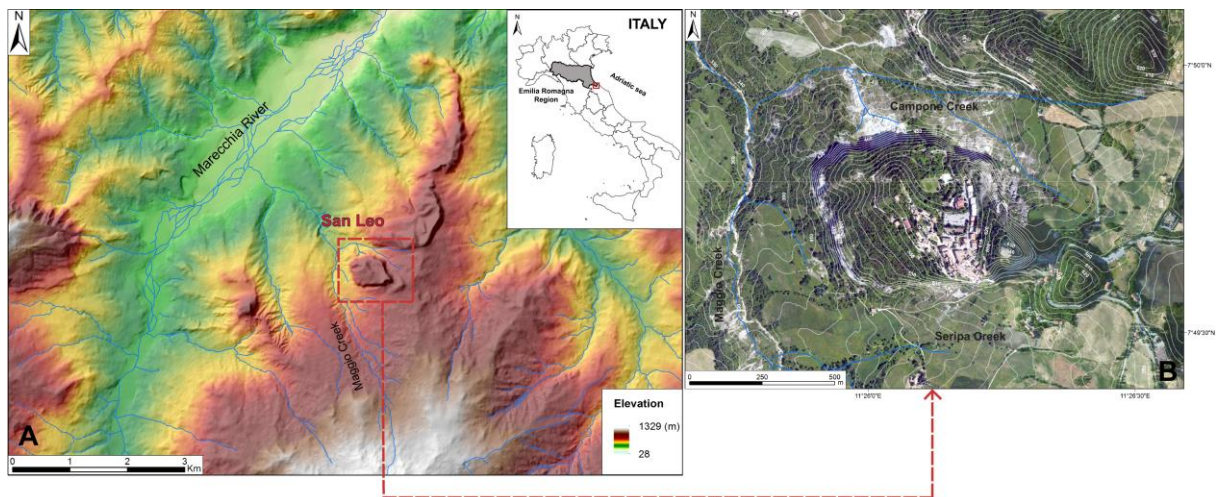

Figure 20. Location map of the San Leo rock massif. (A) Geographic and morphological framework. (B) Contour map projected on an orthophoto.

5.1.1 Geological and structural setting

From a geologic point of view, the rock slab is composed by Epiligurian and Ligurian Units, dating back to Oligocene and Pliocene; the latter abundantly outcrop in the hills and surrounding badlands. The Epiligurian Units consists of limestone-arenaceous formations, in particular, they are represented by the Mt. Fumaiolo Formation (glauconitic sandstone with thin siltstone interlayers and calcarenite), which mainly constitute the top of the rock mass, and the San Marino Formation (thick bedded calcirudite layers and calcarenite), at the base (Conti, 1989, 2002; De Feyter, 1991; Conti and Tosatti, 1996; Cornamusini et al., 2010). The

cliff lies on top of the Argille Varicolori formation (tectonized clay with marly and limy sanstone), belonging to the Ligurian Units bedrock (Figure 21). In the south-eastern sector of the site, these Units crop out as the Sillano (mudstone with thin layers of limestones and marls) and the Mt. Morello Formations (carbonate turbidites) (Ponzana, 1993; Cornamusini et al., 2010) (Figure 21).

The structural setting of the San Leo plate is characterized by faults and fractures with orientation NW-SE and WSW-ENE that control the morphology of the area. Bedding layers mainly dip SW from low to middle angles (Conti and Tosatti, 1996).

During the last four centuries, the San Leo site and the surrounding area was affected by several large landslides (rock falls, earth flows and complex landslides) (Benedetti et al., 2013; Spreafico et al., 2013; Giardino et al., 2015; Borgatti et al., 2015) due to its peculiar geological and geomorphological setting.

The typical slope instability phenomena can be described as "a lateral spread involving the brittle rock slab overlying a more ductile terrain" (Spreafico et al., 2016). In greater detail, the soft clayey substratum is involved in earth flows and weathering-erosional processes leading to the progressive undermining of the overlying rock cliff. This phenomenon causes the opening of the vertical joints in the rock plate and the resulting rock fall and topple at the edge of the rock mass.

Two quite recent examples are the landslides occurred on 11th May 2006 (Figure 22A) and the night between the 29th and the 30th November 2008. The former rock fall of approximately 50,000 m^3 affected the north face of the cliff, reactivating an earth flow in the underlying clay shales, which in turn, evolved in other landslides downstream (Benedetti et al., 2013). The latter was a small-scale rock fall and pertained to the northern cliff as well, involving a volume of about 6 m^3 (Spreafico et al., 2015).
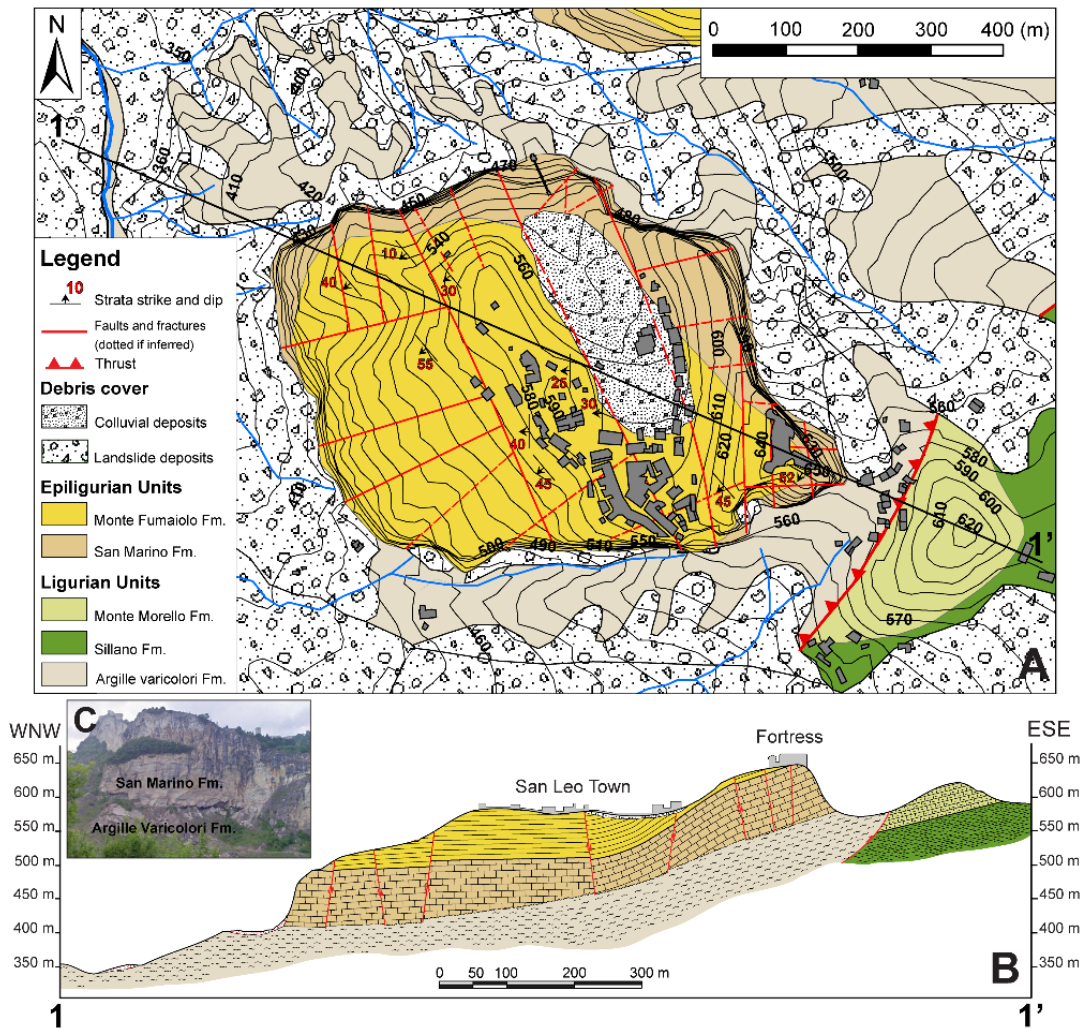
Figure 21. Geology of the San Leo site (from: Frodella et al., 2016). (A) Geological map. (B) Cross section (modified after Conti and Tosatti, 1996). (C) Picture of the NE rock slab sector bordering the slope wall prior to the landslide event.

5.1.2 The landslide

On 27th February 2014, a rock mass of about 0.33 Mm^3 (Borgatti et al., 2015) detached from the north-eastern cliff of San Leo rock plate and collapsed onto the underlying valley (Figure 22B). The rock fall event caused a retreat of the cliff of 30 m (Spreafico et al., 2015) and threated some buildings but fortunately, the collapse occurred in an unpopulated area. As a precautionary measure, the access to the medieval fortress and provincial SP 137 roadway (Figure 22A) were temporarily interdicted (Frodella et al., 2016), and ten private buildings (Figure 22A), a police station and the elementary school were evacuated (Borgatti et al., 2015).

The reconstruction of the temporal evolution of the event was described by Borgatti et al. (2015) in four principal steps and simulated by Spreafico et al. (2016): 1) the progressive

detachment of the cliff along a vertical pre-existing fracture due to the undermining at the toe of the slope; 2) the block toppling; 3) the breakdown and 4) the following debris avalanche with boulders up to 10,000 m^3 expanding in the Campone Creek valley below. After the event, the reactivation of the earth flow in the clayey substratum was hypothesize.

The landslide can be considered as a composite of two movement types: rock slide and rock topple (Spreafico et al., 2016).
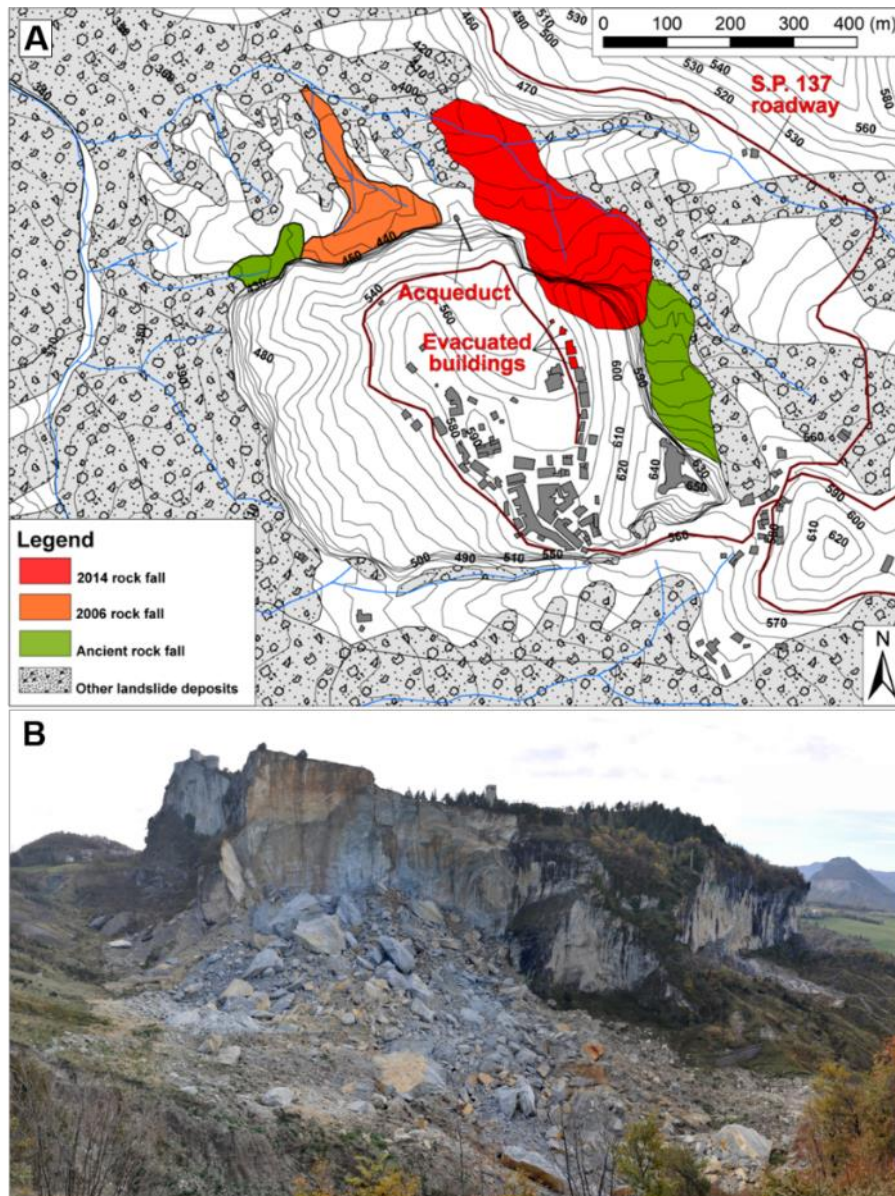

Figure 22. (A) Map of the instability phenomena affecting the San Leo rock plate boundaries. Modified after the IFFI project to produce an inventory of landslides in Italy, carried out by ISPRA (Istituto Superiore per la Protezione e la Ricerca Ambientale) (Triglia et al., 2010). (B) Rock fall caused on 27th February 2014, mapped as red polygon in A. (from Frodella et al., 2016 modified)

After the landslide, the Earth Sciences Department of the Florence University (DST-UNIFI) implemented an integrated monitoring system based on remote sensing techniques in order to measure the possible ground deformations of the investigated area and to evaluate the residual risk (the monitoring results are described in detail in Frodella et al., 2016).

The post-event displacement analysis was performed through a real-time *Ground Based Interferometric Synthetic Aperture Radar* (GB-InSAR) monitoring coupled with TLS surveys.

The GB-InSAR system is composed of a coherent microwave transceiver unit, characterized by a transmitting and receiving antenna, operating in the k_u-band (wavelength range of 2.5–1.67 cm; central frequency of 17.2 GHz and 200 MHz bandwidth). Synthetic aperture is achieved by moving a motorized sled hosting the radar head along a mechanical linear rail (parallel to the azimuth direction). The working principle of the GB-InSAR technique involves radiating microwaves toward the investigated area and measuring the backscattered signal, obtaining a SAR image. The SAR image is created by combining the spatial resolution along the direction perpendicular to the rail (range resolution, *ΔRr*) and the one parallel to the synthetic aperture (azimuth, or cross-range resolution, *ΔRaz*) (Luzi, 2010) and contains amplitude and phase information of the backscattered echo from the examined scenario objects. The evaluation of the phase difference, pixel by pixel, between two pairs of sequential SAR images, allows to obtain a 2D displacement map of the investigated area, called interferogram (Bamler and Hartl, 1998). The measured movement is that component parallel to the instrument line of sight (L.O.S. – direction connecting the sensor and the object), while the displacements occurring in the direction perpendicular to the LOS are missed. Furthermore, cumulative displacement maps (Figure 23) of selected period can be obtained.

Taking advantage of TLS survey (see following paragraph), three-dimensional model was merged with the GB-InSAR cumulative displacement data to obtain a 3D GB-InSAR cumulative displacement map, in which the detected LOS displacements can be directly visualized on the 3D representation of the investigated area. In this work, the 3D GB-InSAR cumulative displacement map for the period between 7th March 2014 and 6th June 2015 is reported (Figure 24).
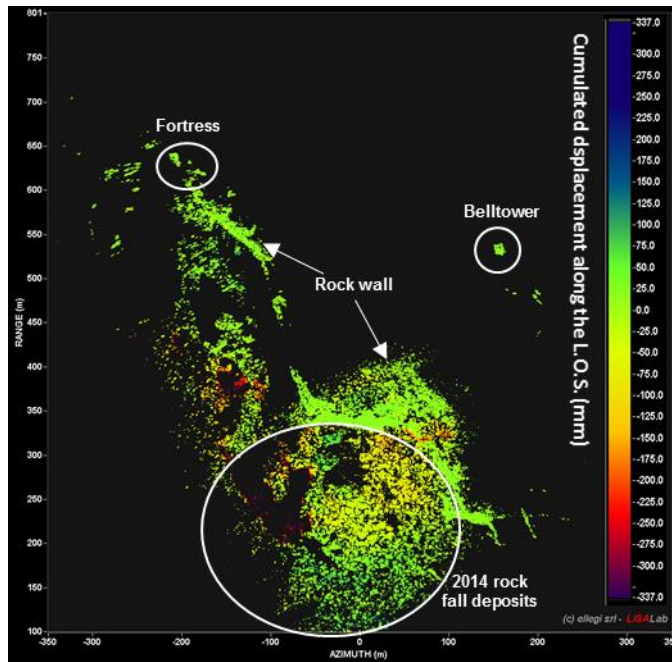
Figure 23. GB-InSAR cumulative displacement map of San Leo study area measured from 7th March 2014 to 7th March 2015 (modified from Frodella et al., 2016).
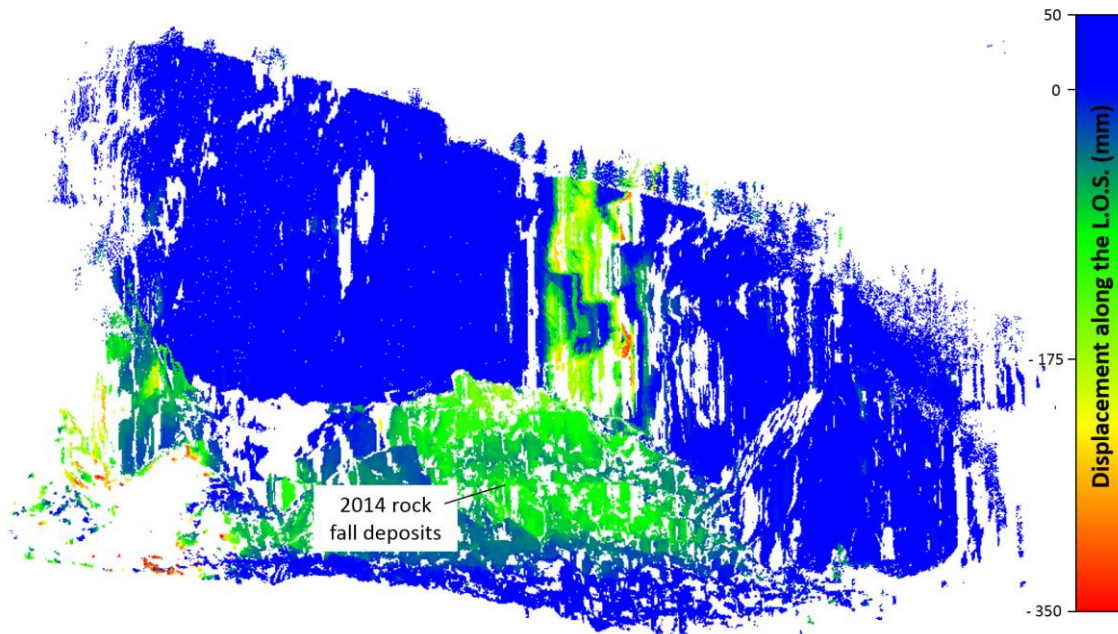

Figure 24. 3D GB-InSAR cumulative displacement map of the San Leo cliff.

5.1.3   TLS monitoring activity

5.1.3.1   TLS survey

The employed terrestrial laser scanner (property of DST-UNIFI) is a long-range and high-accuracy 3D time-of-flight instrument (model Riegl LMS-Z420i; RIEGL 2010a) coupled with calibrated digital camera (Figure 25). This device is able to acquire the position of up to 12,000 points/s by operating in the near-infrared wavelength, with a maximum angular resolution of 0.008°, a single point accuracy of ± 10 mm (one σ at 50 m range under RIEGL test conditions) and from a maximum distance of 800 m.

During the monitored period, five different laser scanner surveys (7th March 2014, 11st June 2014, 18th December 2014, 3th June 2015, 9th September 2015) were performed from different viewpoints (Figure 26). With change detection purpose, four monitoring periods in which each scan was compared with the first one were selected (Figure 26). The specifications for each survey are listed in Table 1.

The acquired point clouds were linked to a global reference system by performing a RTK-GPS survey (Table 2) of several laser reflectors placed in the surveyed area (Figure 26). The resulting georeferencing standard deviation is 0.03 m.
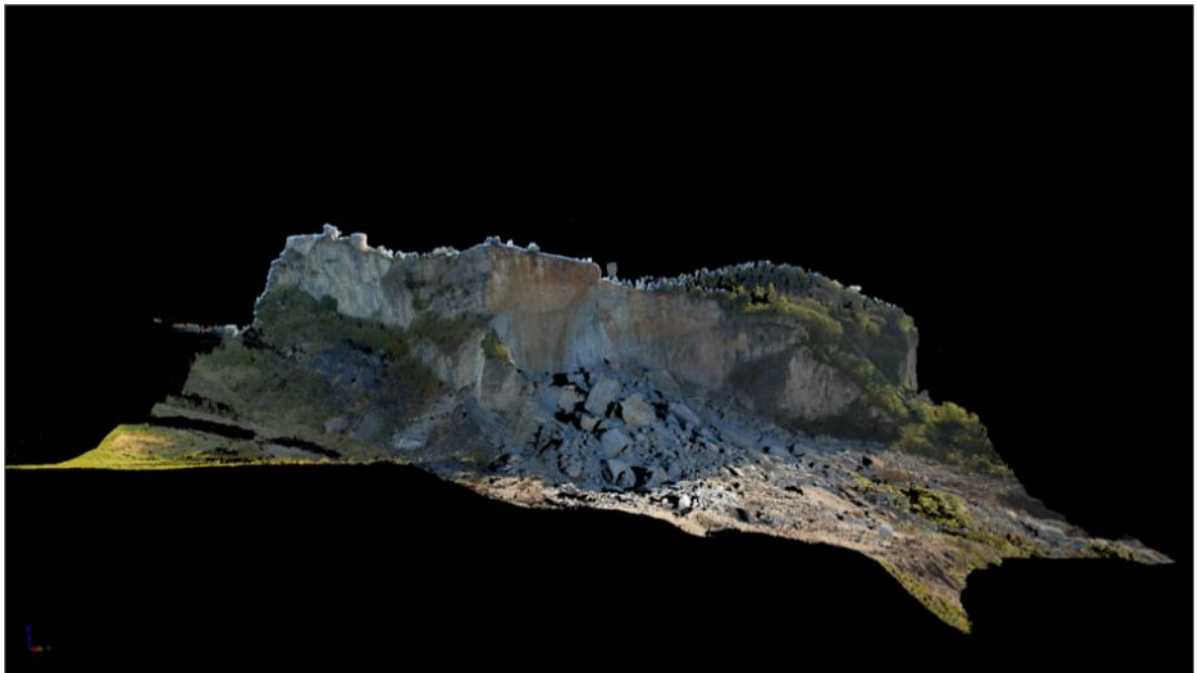

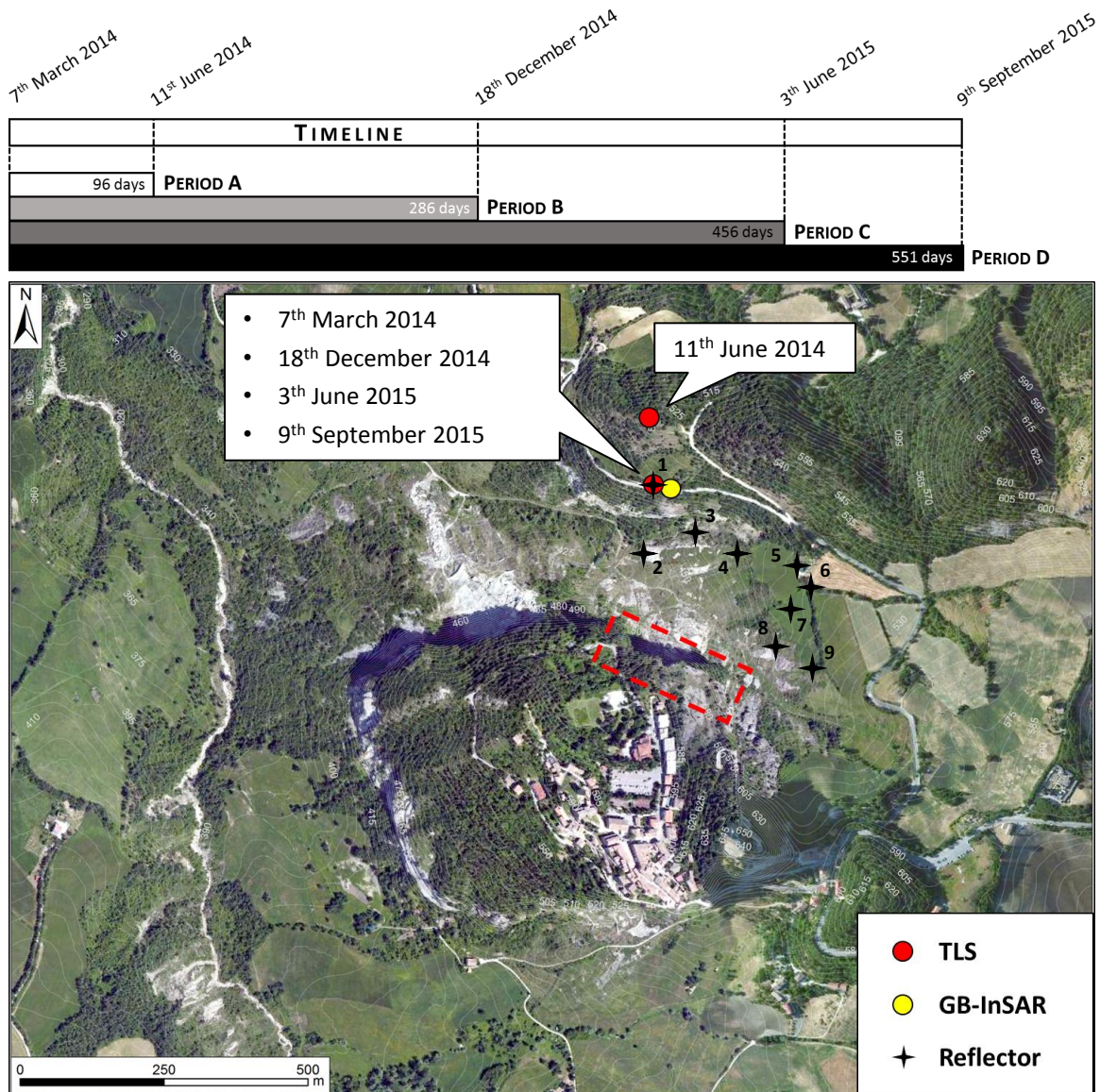*Figure 25. Coloured point cloud of San Leo cliff.*

Figure 26. Schematic workflow of the survey dates and periods of study and location of the employed terrestrial monitoring devices and reflectors. The collapsed cliff sector is highlighted with a dashed red rectangular.

Table 1. Specifications for each laser scanner survey.

	Theta (°)			Phi (°)			Points	Range (m)
	min	max	inc	min	max	inc		
7th March 2014 survey	64.999	124.843	0.031	62.031	239.925	0.031	10˙785˙924	about 320
11st June 2014 survey	65.000	127.384	0.028	80.706	239.466	0.028	12˙640˙659	about 420
18th December 2014 survey	65.119	125.029	0.030	108.484	199.366	0.030	6˙068˙964	about 320
3th June 2015 survey	50.000	129.870	0.070	0.000	359.870	0.070	5˙872˙164	about 320
9th September 2015 survey	65.000	128.990	0.030	60.010	241.940	0.030	10˙497˙982	about 320

Table 2. Global coordinates for each reflector (UTM-WGS84) and corresponding precision.

	X (m)	Y (m)	Z (m)	Coordinate quality (m)
Reflector 1	286757.928	4864414.178	493.822	0.0335
Reflector 2	286749.712	4864277.048	454.335	0.0252
Reflector 3	286806.451	4864294.014	466.838	0.0203
Reflector 4	286861.737	4864270.858	480.437	0.0223
Reflector 5	286938.254	4864224.778	503.555	0.0213
Reflector 6	286953.197	4864211.323	506.022	0.0159
Reflector 7	286934.400	4864193.797	498.780	0.0282
Reflector 8	286905.349	4864125.901	486.662	0.0237
Reflector 9	286962.583	4864108.027	510.059	0.0226

5.1.3.2 Data pre-processing

Raw point clouds were processed using RiSCAN PRO software package (RIEGL, 2010b). This concerned, first of all, the manual removal of sporadic vegetation and outliers points. Furthermore, Multi Station Adjustment (MSA) tool was used to align each acquisition to the first one (7th March 2014). This tool modifies the orientation and position of each scan position in several iterations in order to calculate the best overall fit for them and it operates, as best it can, with well-defined surfaces. The MSA can use tiepoints, tieobjects and polydata objects to detect the closest point (ICP algorithm, see chapter 2) of the other point clouds for each point of a point cloud and to align the scan positions.

To speed up the process it's necessary to preprocess the data, to make this the filter "Plane patch filter" was used. This filter looks for planar areas in the selected point cloud dividing the space into equal sized cubes of certain size and for each one trying to estimate a best-fit plane from all points inside the cube. If the standard deviation of the normal distances between all points and the plane is less than "Maximum plane error" then the plane is added to the resulting list of plane patches. If this condition is not fulfilled, the cube's points are divided into eight small cubes, each having the half edge length of the current cube; for each sub cube the plane estimation is repeated. The reiteration is stopped when either a valid plane was found, the user can choose the number of points inside the cube or the cube size.

5.1.4 Tool application and results

Both routines were applied to San Leo cliff test site. The resulting 3D point cloud maps colored as a function of the computed features, were visualized within the open-source software CloudCompare v. 2.6.2 (EDF R&D, 2011).

5.1.4.1 Point cloud analysis

Since the first data scansion was considered as the *reference* cloud in the comparison, a preliminary point cloud analysis of the 7th March 2014 survey was performed. In order to choose which input parameters were more appropriate for this case study, a trial and error procedure was performed. A neighbourhood cube half-side *R* of 1 m, a selection parallelepiped base half-side *r* of 0.5 m, a minimum number of neighbouring points per cluster N_{min} of 10 were selected as more suitable.

The resulting morphometric characterization of the *reference* cloud is shown in Figures 27 to 30. For each feature, the related frequency histogram is presented; the frequency was computed as the number of points belonging to a certain feature class. In detail, the Figure 27 shows the distribution of the values of orientation with respect to the north (azimuth angle), associated to the corresponding frequency histogram. The map shows a general orientation of the rock faces towards NE and SW, well highlighted by a bi-modal distribution of the values in the histogram of frequency. The result of slope angle analysis (Figure 28) is globally characterized by nearly vertical values excepted some limited areas in the central and upper parts of the cliff and, in particular, on the northern side where the rock faces are less steep (≈45°).
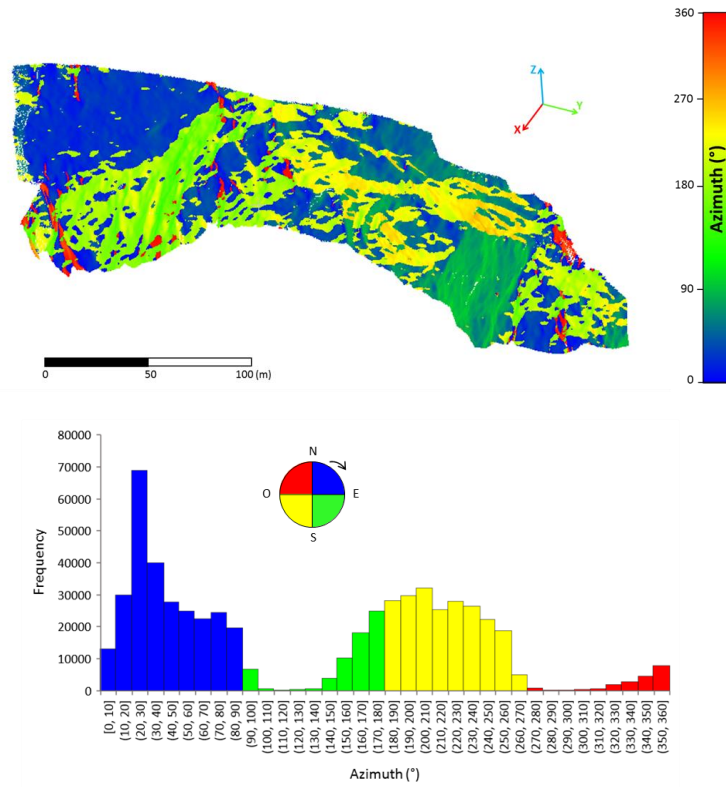
Figure 27. Azimuth angle map and related frequency histogram about San Leo rock cliff (7ᵗʰ March 2014 survey point cloud).
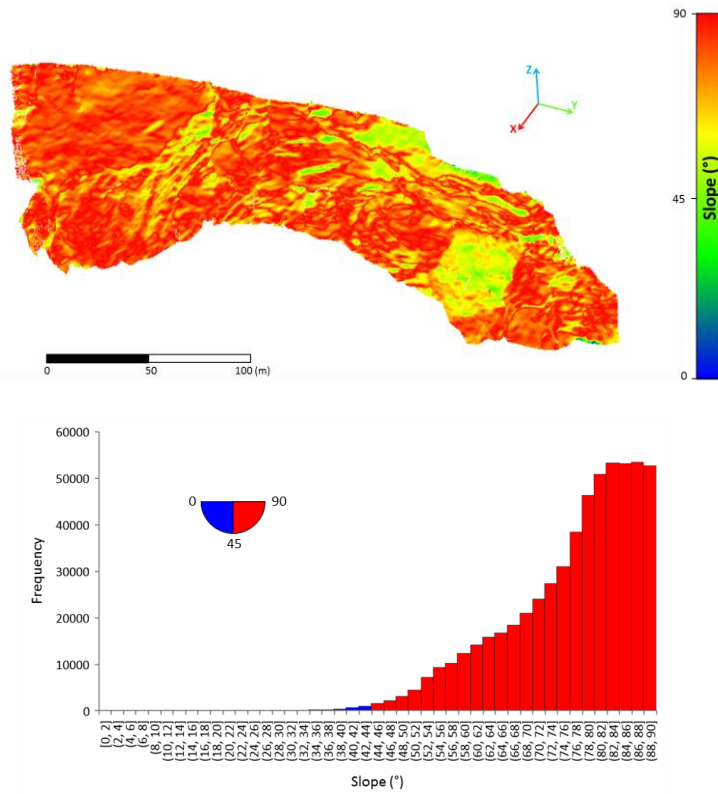

Figure 28. Slope angle map and related frequency histogram about San Leo rock cliff (7ᵗʰ March 2014 survey point cloud).

The map shown in Figure 29 represents the distribution of the roughness index in the observed scene. The frequency histogram show a unimodal distribution, centred on values between 0.04 and 0.07 meters, reaching a maximum of 0.46 m although values of such entity are present in very limited areas, that will be further analysed in the chapter 6.

The last output parameter of the point cloud analysis is the point density, a function of the distance between the sensor and the cliff, the slope orientation with respect to the laser beam direction and the backscattering properties of the surface. The spatial distribution of the point density is shown in Figure 30, with the respective histogram of frequency. Generally, the point cloud obtained in San Leo have a mean density of 60 points per cubic meter, reaching maximum values of more than 130 points per cubic meter in the part of the scene, closer to the device.
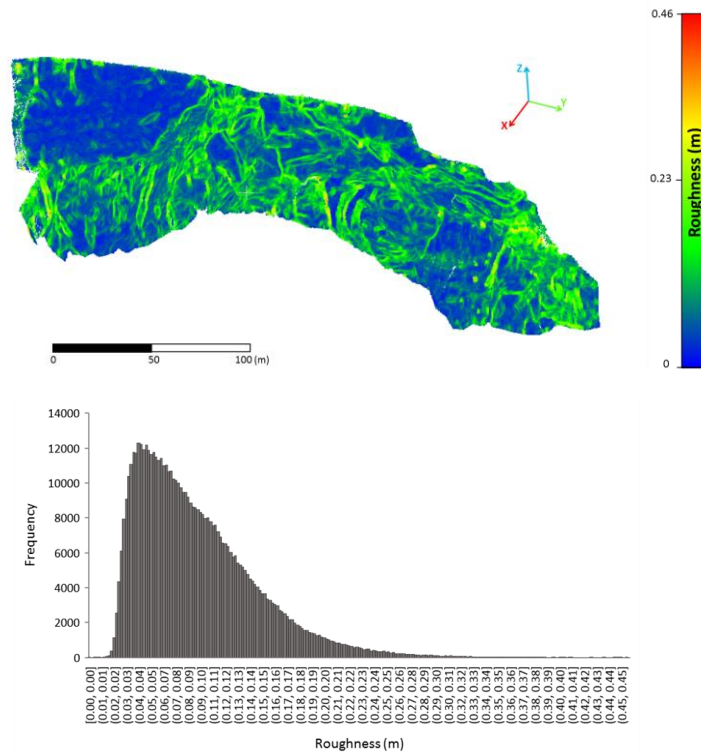

Figure 29. Roughness index map and related frequency histogram about San Leo rock cliff (7th March 2014 survey point cloud).
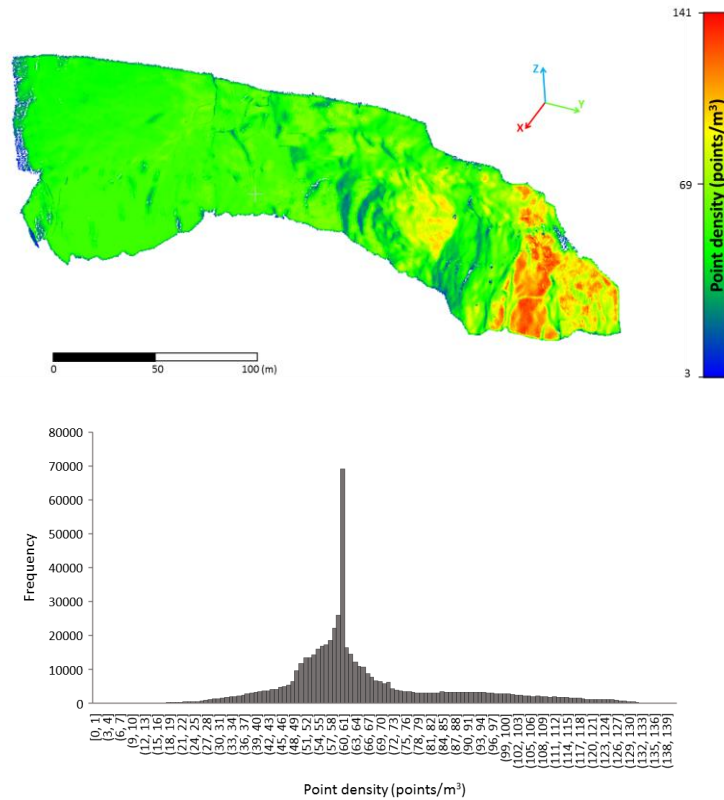
Figure 30. Point density map and related frequency histogram about San Leo rock cliff (7th March 2014 survey point cloud).

5.1.4.2 Point cloud comparison

To perform the comparison, the same values of the input parameters chosen for the point cloud analysis were selected. The values are: a neighbourhood cube half-side R of 1 m, a selection parallelepiped base half-side r of 0.5 m and a minimum number of neighbouring points per cluster N_{min} of 10. Furthermore, a maximum length of parallelepiped Z_a of 5 m and an average cube half-side R_a of 1 m were selected.

The resulting temporal variations with respect to the *reference* cloud (7th March 2014), are represented as distances (calculated along the local normal and projected along x-, y-, z-axis) for each monitoring period and shown in Figure 31 (Period A), Figure 32 (Period B), Figure 33 (Period C) and Figure 34 (Period D). The distance values on the maps are associated to a colorbar, in which values around zero are shown in green; positive distances increasing (in module) from yellow to red; negative distances increasing (in module) from light blue to dark blue. The grey colour indicates no-distance value.

The map of distances along the local normal considering the first monitoring period (Period A) (Figure 31a) shows a central zone of the rock mass (red dashed shape) characterized by positive distances around 0.2 m reached in 96 days. The decomposition of the normal vector along the three principal axes (Figure 31 b, c and d) highlights a predominant movement in north direction (y-direction) for this area. Similar values are also detected in the northern upper part of the cliff (indicated by an arrow) but they correspond to noise, due to presence of the vegetation. The highest values (around 2 m) of positive distances (red colour) are concentred in a small portion of the upper part of the cliff (indicated by a dashed arrow) and in the borders of the yellow central zone. The negative distances were computed in several areas, reaching the maximum value of around -1.3 m in correspondence of a well-defined zone indicated by a black dashed oval. Most of these distances are concentrated along the x-axis.
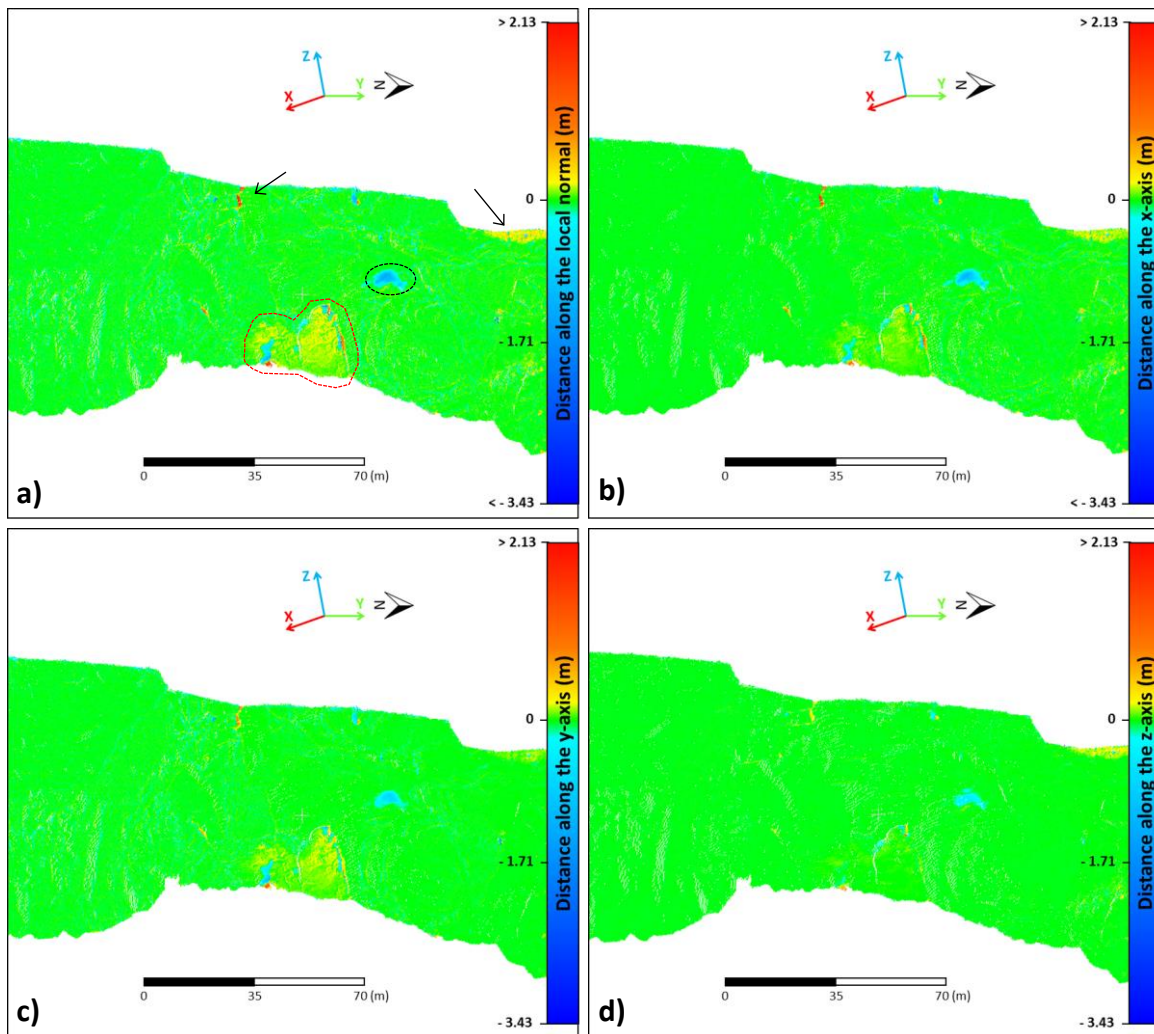

Figure 31. Point cloud comparison for Period A (7th March - 11st June 2014): a) distance along the local normal, b) distance along the x-axis, c) distance along the y-axis, d) distance along the z-axis.

Considering Period B (Figure 32), the positive distances in the formerly recognized zone (red dashed shape) reach the value of approximately 0.4 m during 286 days of monitoring with an increased spatial extent. The areas coloured in blue (negative distances) are increased in number, involving a greater surface area. Four main areas can distinctly distinguished (black dashed ovals), in addition to the formerly recognized area (balck dashed oval in Figure 31), with distances of up to -2 meters, in some small portions.
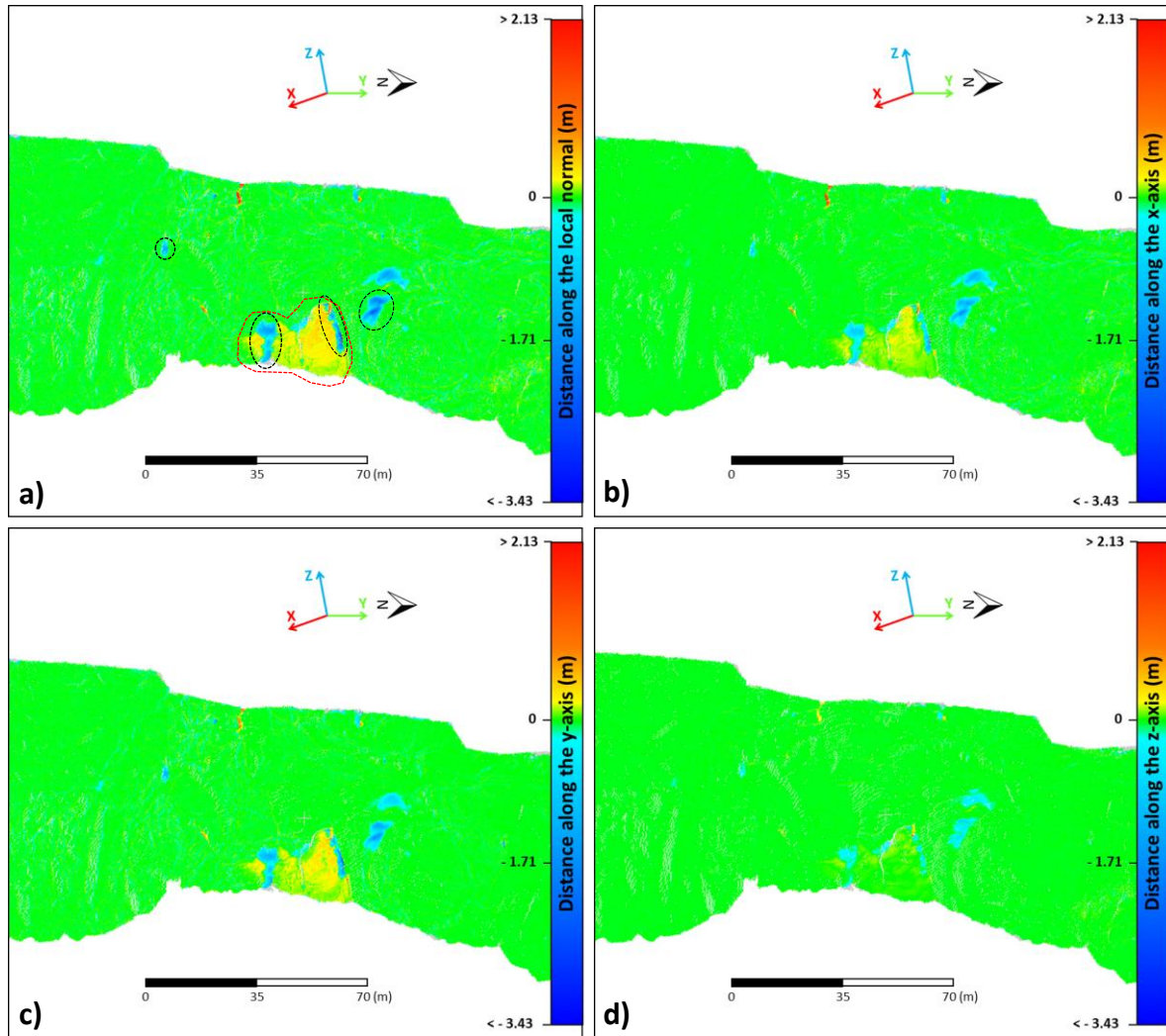

Figure 32. Point cloud comparison for Period B (7th March - 18th December 2014): a) distance along the local normal, b) distance along the x-axis, c) distance along the y-axis, d) distance along the z-axis.

The comparison map about the positive distances computed along the local normal during the Period C (Figure 33a) shows a slightly increased extent of the formerly recognized zone indicated by a red dashed shape, with nearly constant distances of around 0.4 m.

Also the areas characterized by negative distances are increased, reaching values of around -2.4 m in the area located at the base of the rock mass (black dashed oval). The major distance

values, both positive and negative, are calculated along the x- and y- axes, with considerably smaller movements along the vertical axis (z-).

In the northern upper part of the cliff, the noisy effect of the vegetation can be observed.
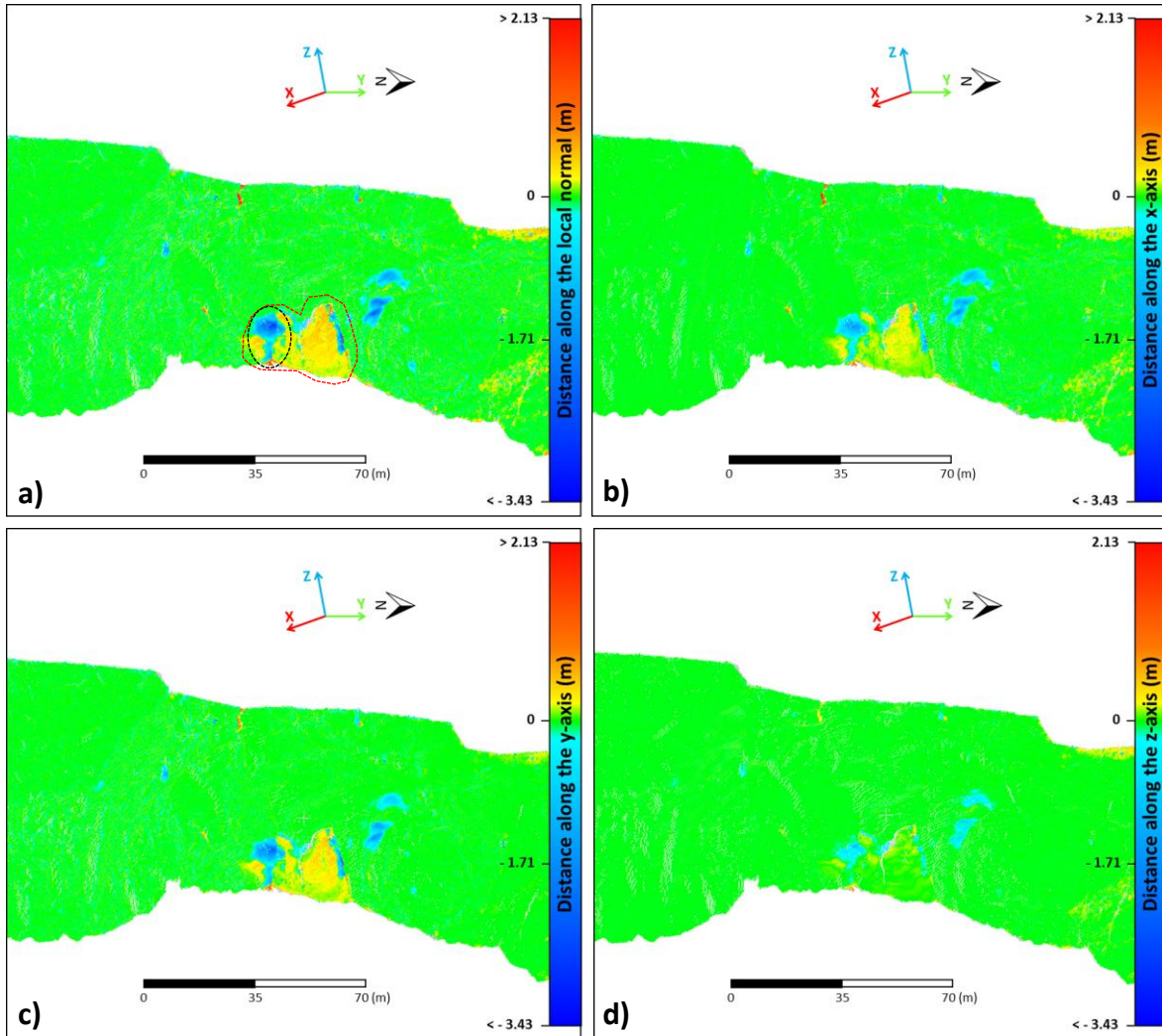

Figure 33. Point cloud comparison for Period C (7th March 2014 – 3th June 2015): a) distance along the local normal, b) distance along the x-axis, c) distance along the y-axis, d) distance along the z-axis.

The last monitoring period (Period D, Figure 34) does not show significant changes with respect to previous period.

The small portion in the upper part of the cliff recognized in the first monitoring period (indicated by a black dashed arrow in Figure 31), is present in each period of study with values comparable to those detected in Period A.
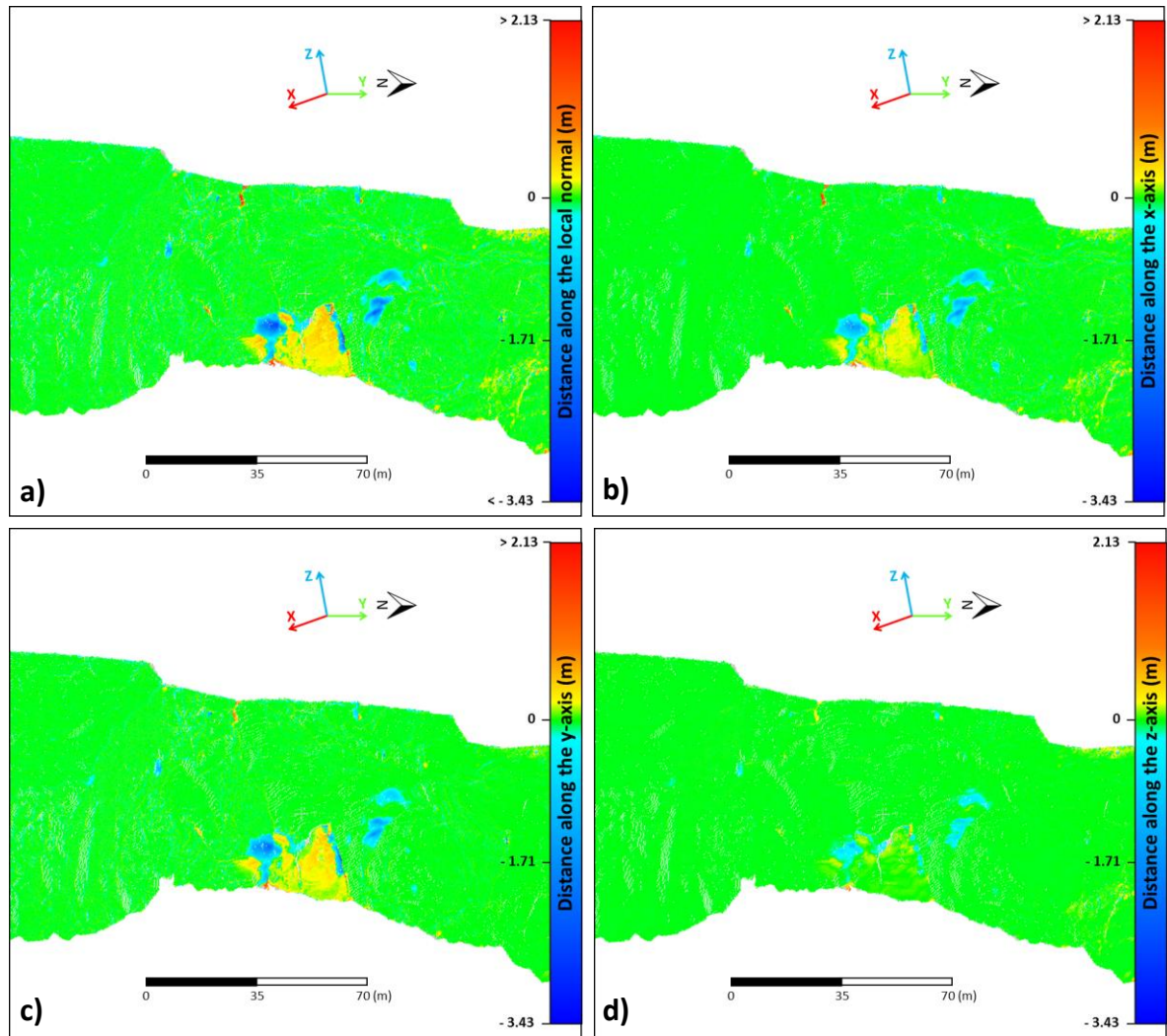
Figure 34. Point cloud comparison for Period D (7th March 2014 – 9th September 2015): a) distance along the local normal, b) distance along the x-axis, c) distance along the y-axis, d) distance along the z-axis.

The influence of the rock surface roughness on comparison results is visible causing, in some cases, a noise affecting the results of the comparison. For this reason, an averaging process was performed to reduce the random Gaussian noise effect, due to instrumental error and roughness. Furthermore, the averaging allows to clearly distinct the previously recognized areas.

The average distances calculated along the local normal are presented for each period (Figures 35 to 38), in association with the corresponding frequency histograms that show a normally distribution of the resulting distances. The average distance values on the maps are associated to a colorbar, in which values around zero are shown in green; positive distances increasing

(in module) from yellow to red; negative distances increasing (in module) from light blue to dark blue. The grey colour indicates no-distance value.

Figure 35. Average distance computed starting from distance along the local normal for Period A and related frequency histogram.

Figure 36. Average distance computed starting from distance along the local normal for Period B and related frequency histogram.
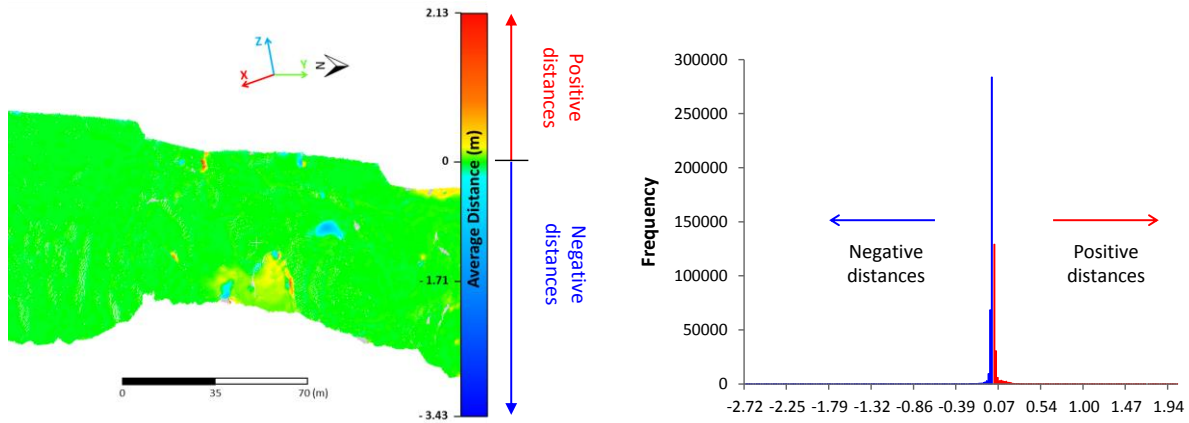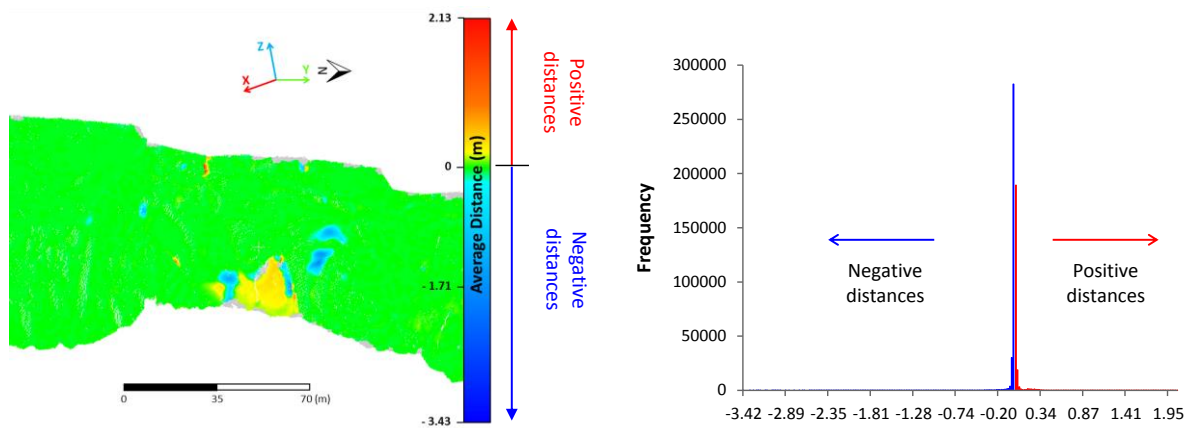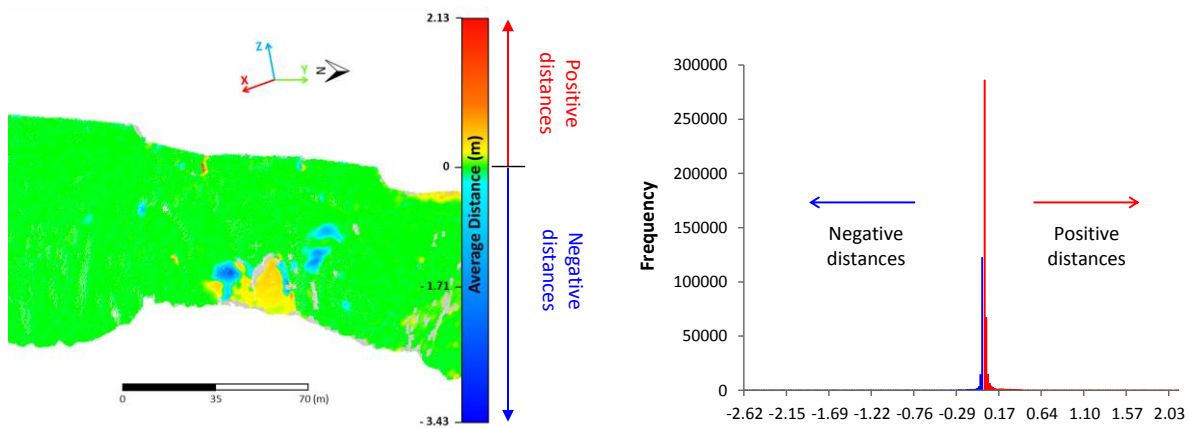

Figure 37. Average distance computed starting from distance along the local normal for Period C and related frequency histogram.
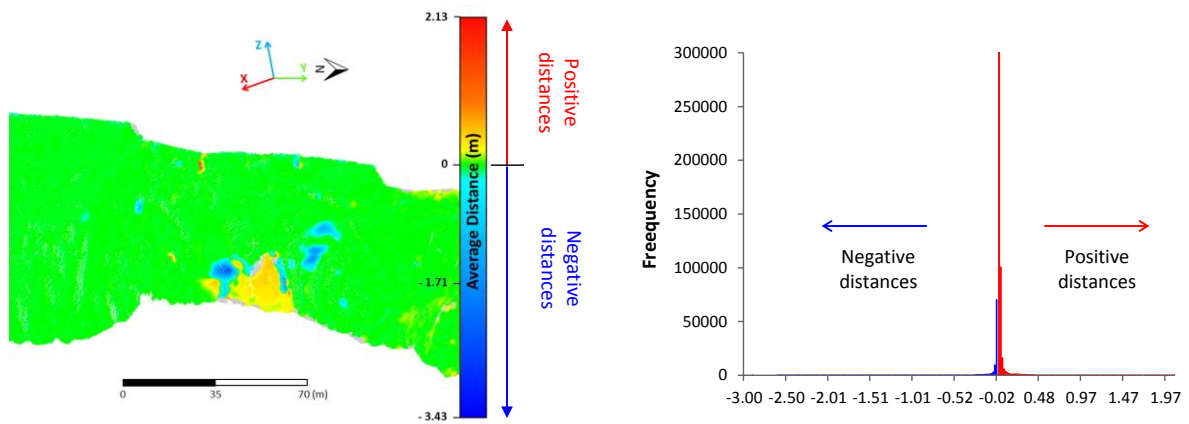
Figure 38. Average distance computed starting from distance along the local normal for Period D and related frequency histogram.

5.1.4.3 LoD and significant distances

The minimum threshold to distinguish changes from noise was defined based on the average distance results on the areas considered as stable during the different monitoring periods (the areas are indicated in Figure 39). The substantial stability of these areas was even confirmed by GB-InSAR monitoring (see Figure 24 in paragraph 5.1.2).

For each monitoring period, the resulting standard deviation of the averaged distances was 0.13 m (Figure 40) and this value was selected as Level of Detection.

Figure 39. Areas considered to be stable during the different monitoring periods.
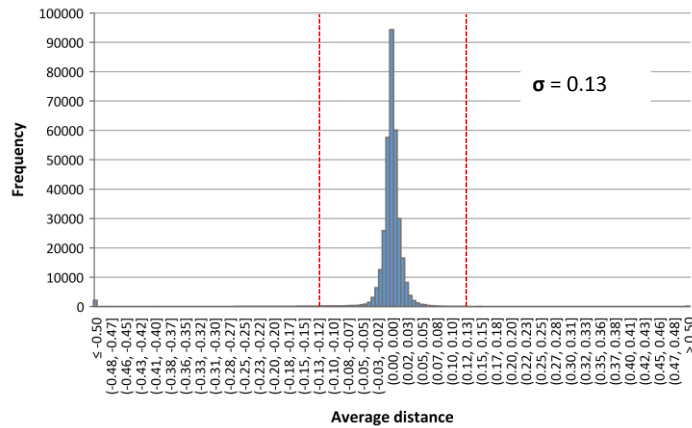
Figure 40. Histogram representing the frequency of the average distances on the areas considered to be stable during the different monitoring periods. The standard deviation is indicated by red dashed lines.

Once provided LoD value to Routine 2, the positive and negative significant distances were extracted from the point cloud. Positive distances (in red in Figure 41) represent areas characterized by displacements, whereas negative distances (in blue in Figure 41) represent detachment zones.
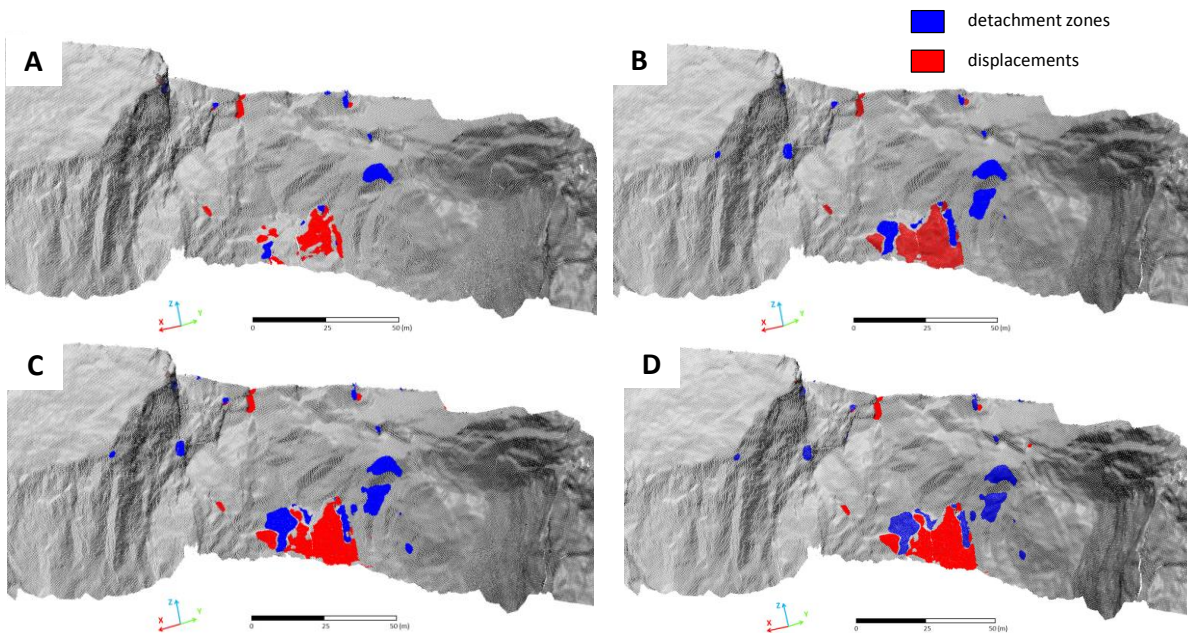
Figure 41. Detachment zones (in blue) and displacements (in red) for Period A (A), Period B (B), Period C (C), Period D (D).

5.1.4.4 Cluster analysis

In order to automatically segregate the significant distance zones outcoming from the cloud comparison, and to compute their area, a cluster analysis was performed within the Routine 2. The multiplication factor which better fits to the investigated point cloud is selected by means of trial and error procedure.

The result of the routine is the creation of a database including the number of recognized zones, the area of these sectors and for every zone provides the information obtained from the point cloud analysis and comparison (that is azimuth, slope, local normal vector, roughness, point density, distance along the local normal, distance along the x-, y- and z-axis).

The cluster analysis for recognized deformations zones, considering the entire monitoring period (Period D), is shown in Figure 42. The identified zones and the corresponding areas are reported in the map with a colour scale ranging from 0 square meters (yellow colour) to 300 square meter (dark red colour). The automatically computed areas for each recognized zone are reported in Table 3. The multiplication factor *F* that resulted as the more suitable for this analysis was equal to 12.8.
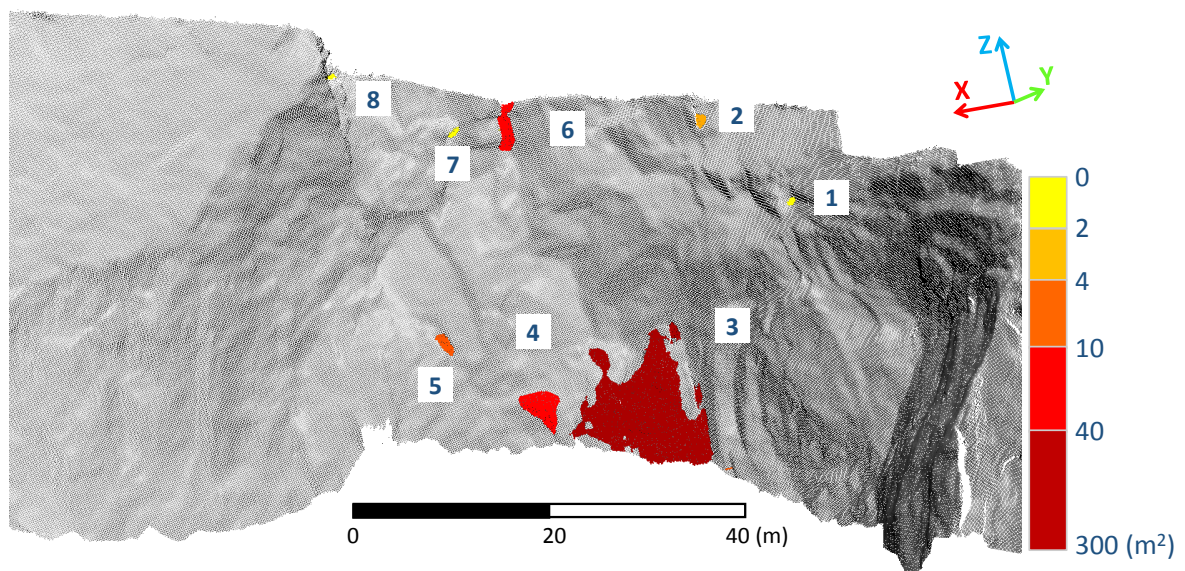
Figure 42. Cluster analysis results for recognized deformations zones.

Table 3. Area for each recognized deformation zones.

	Area (m^2)
Zone 1	1.4
Zone 2	3.7
Zone 3	270.0
Zone 4	33.6
Zone 5	9.9
Zone 6	27.3
Zone 7	1.7
Zone 8	1.6

The resulting cluster analysis for recognized detachment zones about the entire monitoring period (Period D) is shown in Figure 43. The identified zones and the corresponding areas are reported in the map with a colour scale ranging from 0 square meters (light blue colour) to 300 square meters (dark blue colour). The corresponding computed areas are reported in Table 4. The multiplication factor *F* that resulted as the more suitable for this analysis was equal to 13.
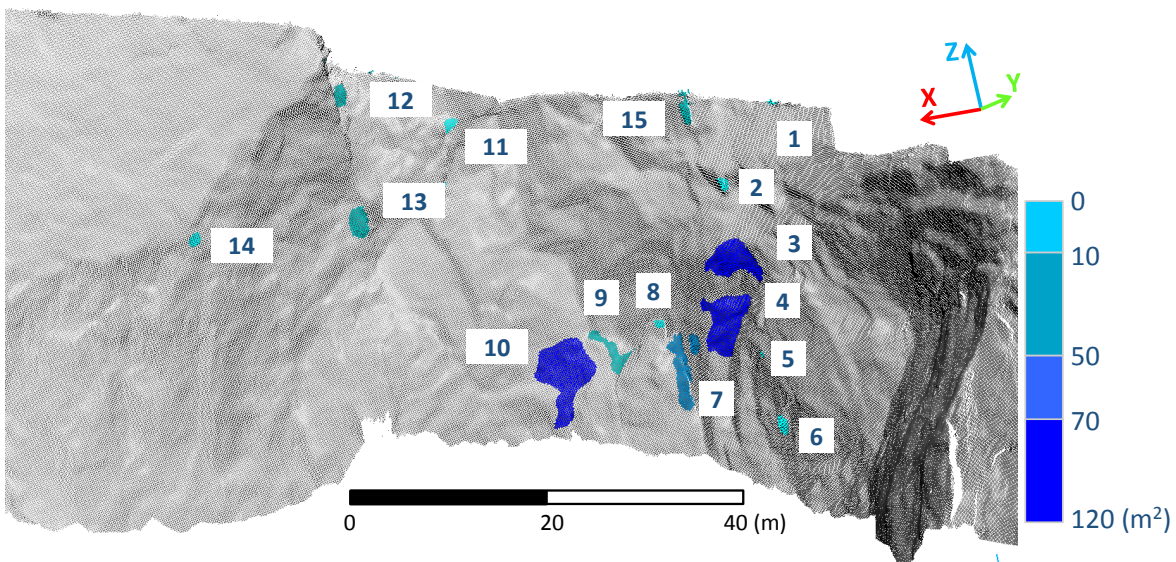
Figure 43. Cluster analysis results for recognized detachment zones.

Table 4. Area for each recognized detachment zones.

	Area (m^2)
Zone 1	0.8
Zone 2	2.8
Zone 3	70.5
Zone 4	108.2
Zone 5	0.5
Zone 6	8.2
Zone 7	69.0
Zone 8	14.6
Zone 9	45.0
Zone 10	112.7
Zone 11	8.2
Zone 12	11.0
Zone 13	19.0
Zone 14	7.7
Zone 15	15.3

5.2 Ricasoli test site

Ricasoli is a village located in a morphological high in the Upper Arno river Valley (Tuscany) (Figure 44), an area historically subject to widespread slope instability phenomena. The village is located in a typical NW-SE oriented intramontane basin formed during the extensional phase of the Neogene-Quaternary evolution of the Tyrrhenian side of the Northern Apennines (Abbate, 1983).
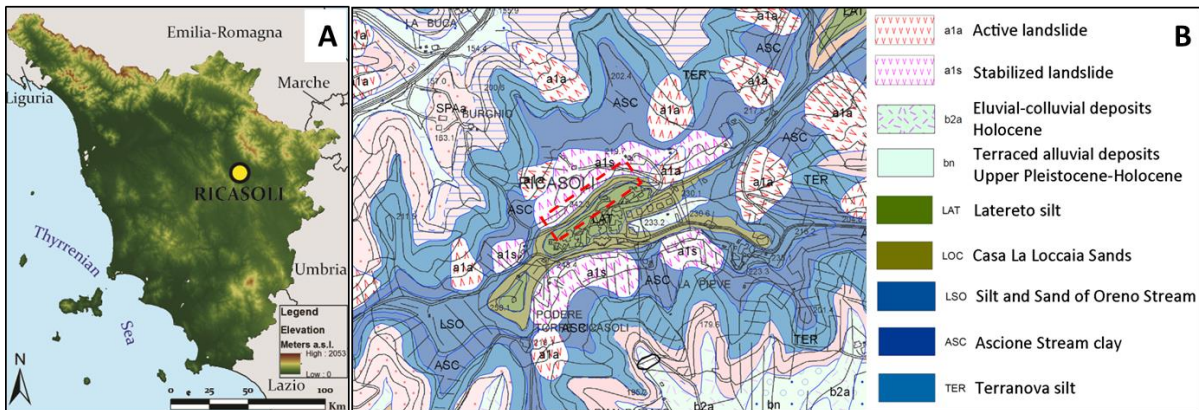
Figure 44. Location (A) and geological map (B) of Ricasoli village (modified from Rosi et al. 2013). The dashed red rectangular highlights the study area.

5.2.1 Geological setting

The substrate of the basin is composed of Cervarola-Falterona Unit (eastern side) and Macigno Formation (western side). The fluvial-lacustrine sediments were deposited in this area in three phases between Lower Pliocene and Upper Pleistocene and can reach a 500 m thickness (Fidolini et al., 2013).

Ricasoli is located above sediments of the fluvial-lacustrine phase (second phase) overcome by the sediments of the fluvial phase (third phase). In particular, from the bottom to the top the second phase consists of (Figure 44):

Terranova silt (TER): grey clayey silts in lower part followed upward by medium-fine clayey sands. These sediments have been deposited in a lacustrine environment and the maximum outcrop thickness is 25–30 m.

Ascione Stream Clay (ASC): this unit consists of peaty silty clays deposited in lacustrine environment and they are characterized by the presence of decimetric layers of lignite. The thickness of the outcrops is 15 m.

Silt and Sand of Oreno Stream (LSO): grey silts, occasionally clayey silts or arenaceous silts, which superimpose yellowish fine and medium grained sands. In the inner part of these sediments residual paleosoils and some levels of conglomerates with pebbles of sandstones are present. The origin of this unit can be referred to a lacustrine environment subject to recurrent fluvial episodes and emersion stages. The thickness of the outcrops is 50 m.

The third phase consists of (Figure 44):

Casa La Loccaia Sands (LOC): Sands and gravels with arenaceous clasts with intercalations of reddish arenaceous silts that often present pedogenesis phenomena.

Latereto silt (LAT): massive silts highly pedogenized, these sediments are deposited in a fluvial plain environment.

This morphological high and the surrounding slopes result to be affected by numerous landslides, which cause the retreat of the escarpments surrounding the village, involving infrastructures and buildings. According to the Cruden and Varnes (1996) classification, in the area predominantly compound slides and falls can be recognized. In particular, compound slides causing the retreat of the escarpments affect the slope surrounding the village and are triggered by heavy and continuous rainfalls.

In the area, many evidences of instability phenomena can be recognized (cracks, fissures on the wall of the buildings and on the streets, small escarpments, corrugation of the soil surface), in particular in the northern slope (Rosi et al., 2013), characterized by a deep movement affecting the clay formations and by the presence of several shallow phenomena. The slope is recently reprofiled and stabilized.

5.2.2 TLS and Digital Photogrammetry survey

In the last years, several shallow landslides (few meters) involved the northern slope of Ricasoli village. For this reason, with the aim to obtain the three-dimensional reconstruction of the topography of the area and to monitor the scenario, a TLS survey and an UAV photogrammetric survey, were carried out in correspondence of the northern slope of Ricasoli, on 30th March 2015 and 30th July 2015, respectively.

The used terrestrial laser scanner (property of DST-UNIFI) is the time-of-flight Riegl LMS-Z420i (RIEGL, 2010a). The resulting point cloud consisted in 1,500,000 points with angular resolution of 0.034 °.

The comparison between these two survey by means of Surface Comparison tool (RiSCAN PRO; RIEGL, 2010) has been presented in **Annex 1**.

Recently, the eastern part of the northern slope was characterized by two new shallow landslides occurred in 1st March and 9th March 2016 as a consequence of intense rainfall, involving a part of a superficial recent landfill (Figure 45).

Figure 45. Northern slope of Ricasoli village with indicated the two landslides occurred in 1st March (on the right) and 9th March 2016 (on the left), respectively.

Therefore, two aerial photogrammetric surveys were carried out in correspondence of the northern slope, respectively on 2nd March 2016 and 6th April 2016 (Figure 46).

Photogrammetric survey was performed using a conventional digital RGB photocamera with 8 MPix resolution mounted on the multicopter drone, named *Saturn*, designed and developed by the Department of Earth Sciences. This UAV has an innovative perimetric chassis that supports flight dynamics and it has onboard a complete and fully configurable acquisition system with frame grabber for scientific instruments. See **Annex 1** for details about the main features of *Saturn* drone.

The first stage of the survey consisted in the adoption of the flight plan, that have to be created ad-hoc to ensure the best coverage of the target area, with an optimal photo overlap in frontal (overlap) and lateral direction (sidelap), taking into account the camera footprint at a certain quote. To optimize flight time, spatial coverage and ground resolution the multicopter drone was programmed to fly at a constant altitude of around 70 m a.g.l. with sidelap and overlap respectively set to 50% and 60%, in order to guarantee a sufficiently redundant coverage of the area of interest. To optimise flight time, spatial coverage and ground resolution the multicopter UAV was programmed to fly at a constant altitude of around 70 m a.g.l. with

sidelap and overlap respectively set to 50% and 60%, in order to guarantee a sufficiently redundant coverage of the area of interest.

In order to have a georeferenced and calibrated 3D model, a sufficient number of Ground Control Points (GCPs) were collected using a RTK-GPS in correspondence of objects on the ground that can be easily recognized in the aerial photos with a homogeneous spatial distribution on the scene (Figure 47). The images were processed using the software Agisoft Photoscan Professional (Agisoft LLC, 2016). The resulting accuracy assessment for each global coordinate and the total error (root mean square error) provided by the software are shown in Tables 5, 6 and 7.

The whole monitoring period was subdivided in four periods of study (Figure 46), in which comparisons between the several surveys were performed.
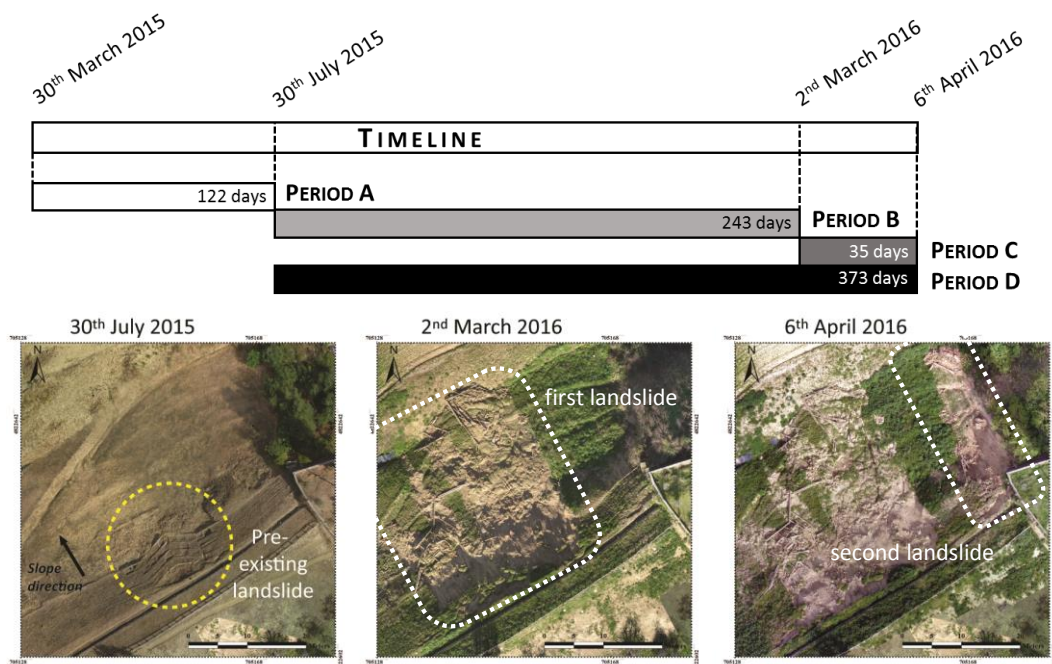
Figure 46. Schematic workflow of the survey dates and periods of study and orthophotos acquired during the three surveys.
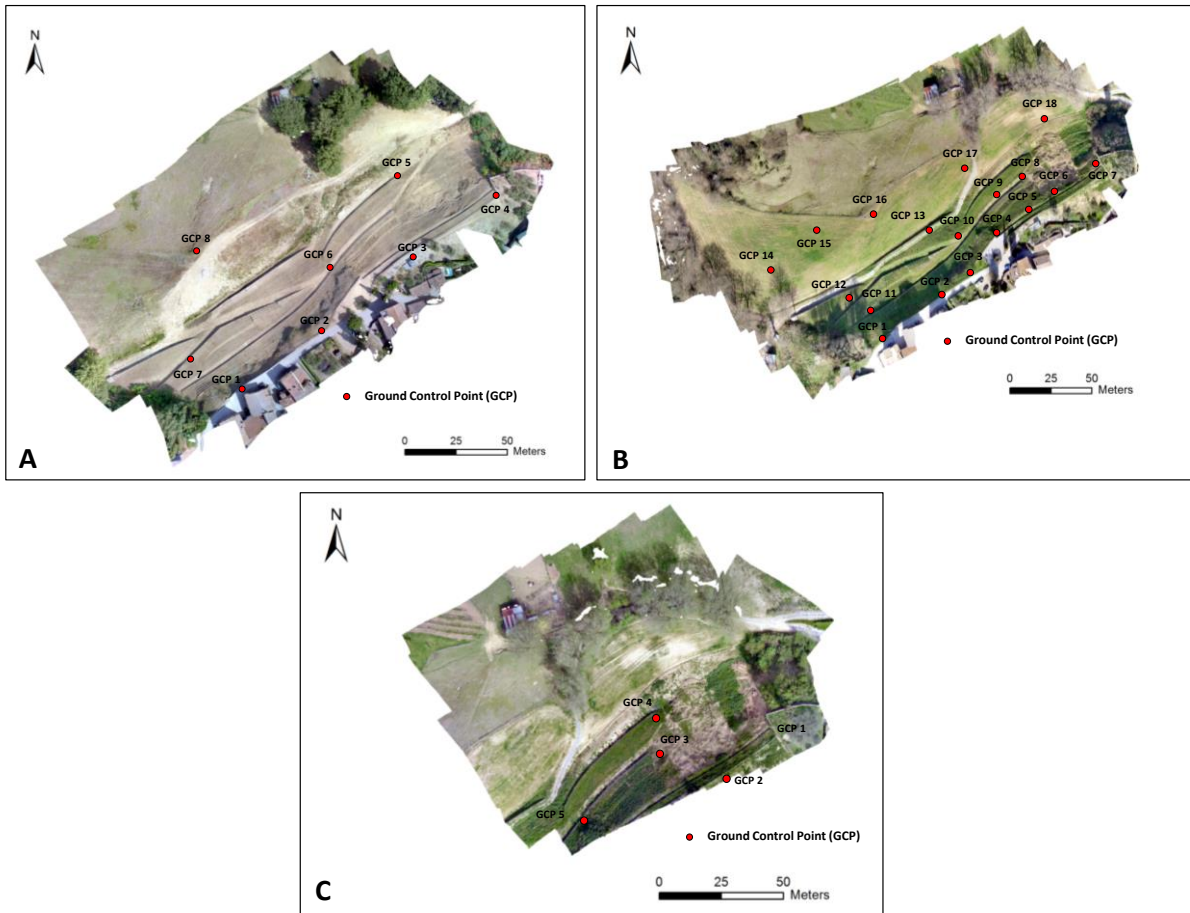
Figure 47. Location of Ground Control Points (GCPs) on the orthophotos about first (30th July 2015) (A), second (2nd March 2016) (B) and third (6th April 2016) (C) surveys.

Table 5. Ground Control Points error for each global coordinate and Ground Control Points total error for the first survey (30th July 2015).

	X error (cm)	Y error (cm)	Z error (cm)	Total error (cm)
GCP 1	-0.718984	1.16923	0.316583	1.40864
GCP 2	0.620463	1.13402	0.787053	1.51341
GCP 3	-0.85015	-1.1875	-0.591576	1.57571
GCP 4	-1.13978	1.6382	0.980768	2.22367
GCP 5	0.583492	-2.6819	-0.600052	2.80947
GCP 6	1.76861	-0.0437532	-0.542086	1.85034
GCP 7	-0.237291	-1.20608	-1.9535	2.30805
GCP 8	-0.255	1.00829	2.25342	2.48185
Total	**0.902327**	**1.43234**	**1.2031**	**2.07683**

Table 6. Ground Control Points error for each global coordinate and Ground Control Points total error for the second survey (2nd March 2016).

	X error (cm)	Y error (cm)	Z error (cm)	Total error (cm)
GCP 1	-0.418813	1.48399	2.10324	2.60792
GCP 2	-1.88304	-1.03575	0.702414	2.26098
GCP 3	-1.57501	1.2246	-1.34038	2.40352
GCP 4	-2.21679	-1.6969	0.617138	2.85911
GCP 5	3.07706	-1.24848	0.0918945	3.32196
GCP 6	2.49995	-2.57911	0.563559	3.63581
GCP 7	1.18189	-1.26442	0.622033	1.83917
GCP 8	-0.059071	0.898904	0.996707	1.34348
GCP 9	-1.15392	-0.400153	-2.91473	3.16027
GCP 10	5.37694	-1.53628	0.539036	5.61802
GCP 11	-2.52805	1.80115	-1.84954	3.6133
GCP 12	0.479137	-8.16205	0.351232	8.18364
GCP 13	4.17298	5.68189	0.76657	7.09121
GCP 14	3.67769	-1.87969	0.465573	4.15637
GCP 15	-4.80768	1.08321	-0.97274	5.02328
GCP 16	5.66021	7.50653	-0.0335757	9.40144
GCP 17	-6.55026	-1.38705	0.570064	6.71973
GCP 18	-4.9614	1.50641	-0.813062	5.24841
Total	**3.48577**	**3.23339**	**1.15154**	**4.89198**

Table 7. Ground Control Points error for each global coordinate and Ground Control Points total error for the second survey (6th April 2016).

	X error (cm)	Y error (cm)	Z error (cm)	Total error (cm)
GCP 1	-2.00613	-8.03309	3.90436	9.15418
GCP 2	4.2379	5.05333	-0.217671	6.59874
GCP 3	3.99553	0.463557	-2.5857	4.78174
GCP 4	-5.54365	-3.52763	1.54063	6.74906
GCP 5	-1.80685	1.62567	-0.418152	2.46625
Total	**3.79329**	**4.59061**	**2.21475**	**6.35357**

5.2.3 Tool application and results

Both routines were applied to the northern slope of Ricasoli village. The resulting point cloud maps colored as a function of the computed features, were visualized within the open-source software CloudCompare v. 2.6.2 (EDF R&D, 2011).

5.2.3.1 Point cloud analysis

In order to investigate the morphological features about the first UAV survey surface, a point cloud analysis of the 30th July 2014 survey, chosen as *reference* cloud, was performed (Figures 48, 49, 50 and 51). Analogously to the previous case study, the more appropriate input parameters were selected by means of a trial and error procedure. A neighbourhood cube half-side *R* of 0.5 m, a selection parallelepiped base half-side *r* of 0.5 m and a minimum number of neighbouring points per cluster N_{min} of 10 were selected as more suitable.

In detail Figure 48 shows the distribution of the values of orientation with respect to the north (azimuth angle), associated to the corresponding histogram of frequency. The map shows a general orientation of the slope towards NW, well highlighted by the distribution of the values in the frequency histogram. The result of slope angle analysis (Figure 49) is globally characterized by low values of inclination (<45°) except for some limited areas corresponding to the main stabilization walls and, some of them, to pre-existing landslide scarps.
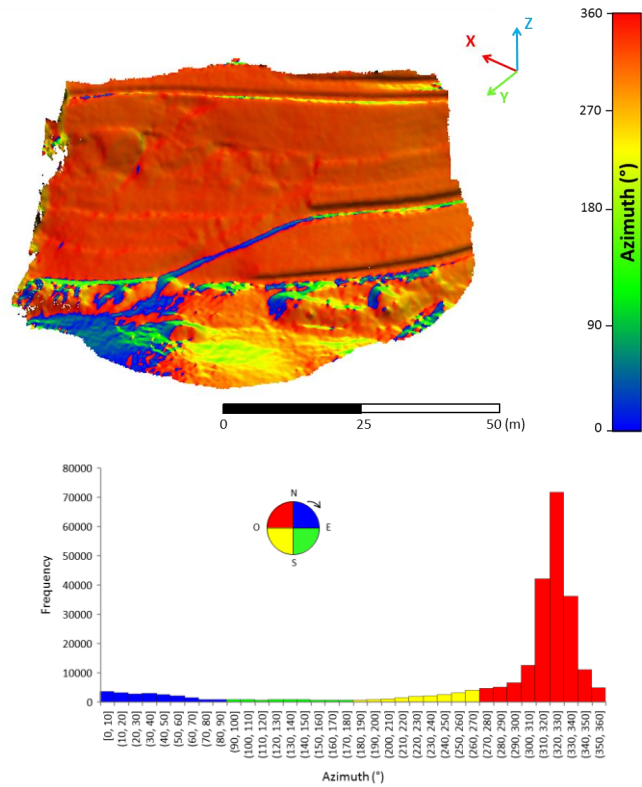
Figure 48. Azimuth angle map and related frequency histogram about the northern slope of Ricasoli (30th July 2015 survey point cloud).
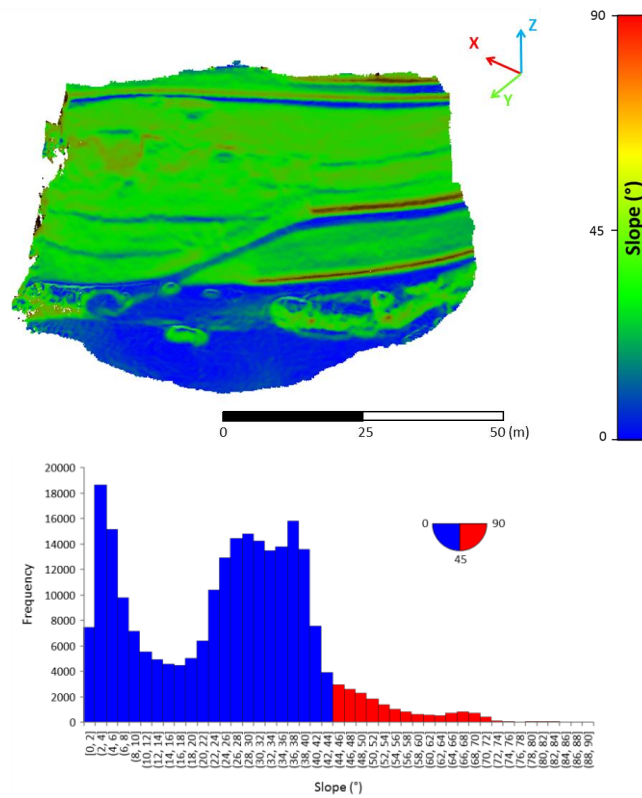

Figure 49. Slope angle map and related frequency histogram about the northern slope of Ricasoli (30th July 2015 survey point cloud).

The distribution of the roughness index in the investigated area is shown in Figure 50. The frequency histogram show a distribution centred on values between 0.01 and 0.02 meters, reaching a maximum of 0.22 m in correspondence of areas with high vegetation, that originate noise in the point cloud.

The last output parameter of the point cloud analysis is the point density (Figure 51), that also in the case of UAV survey depends on the distance between the sensor and the investigated object and therefore on the resolution of the images. The frequency histogram of the point density highlight bimodal distribution of the values centered on 46 and 58 points per cubic meter.
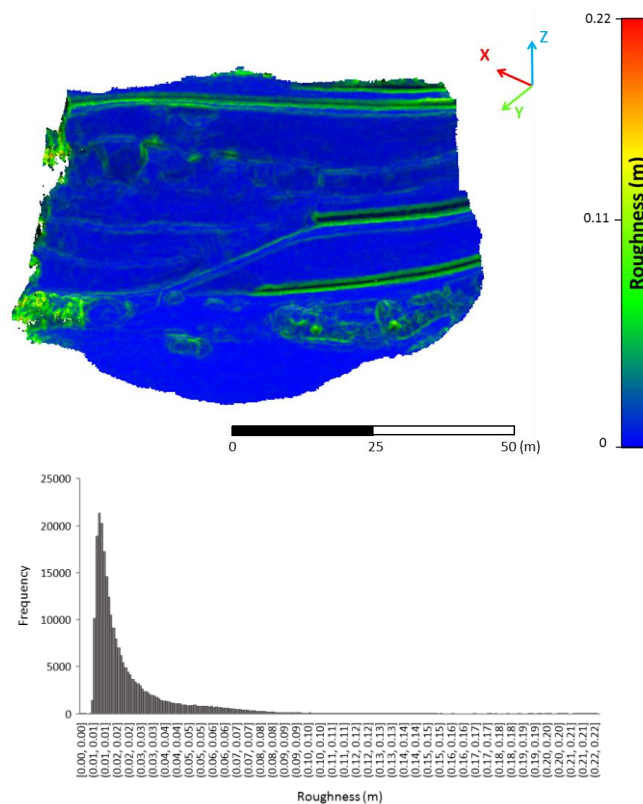

Figure 50. Roughness index map and related frequency histogram about the northern slope of Ricasoli (30th July 2015 survey point cloud).
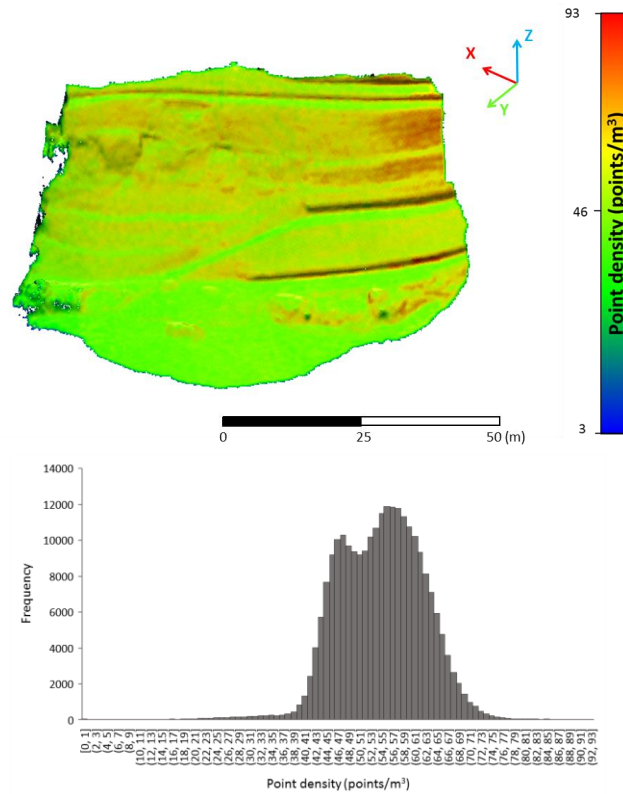
Figure 51. Point density map and related frequency histogram about the northern slope of Ricasoli (30th July 2015 survey point cloud).

5.2.3.2 Point cloud comparison

To perform the comparison, a neighbourhood cube half-side *R* of 0.5 m, a selection parallelepiped base half-side *r* of 0.5 m, a minimum number of neighbouring points per cluster N_{min} of 10, a maximum length of parallelepiped Z_a of 5 m, an average cube half-side R_a of 1 m were selected as more suitable.

The resulting distances (distance along the local normal and distances along x-, y-, z-axis) for each monitoring period are shown in Figure 52 (Period A), Figure 53 (Period B), Figure 54 (Period C) and Figure 55 (Period D). In the first comparison, the point cloud used as *reference* is the one acquired by TLS, while in the further cases the changes are analysed based on only photogrammetric clouds.

The distance values on the maps are associated to a colorbar, in which values around zero are shown in green; positive distances (in module) increasing from yellow to red; negative distances (in module) increasing from light blue to dark blue. The grey colour indicates no-distance value.

The map of distances considering the first monitoring period (Period A) (Figure 52a) reporting the comparison between the TLS survey and the first UAV survey, show values of distance mainly distributing around zero with some sparse areas characterized by positive and negative values due to anthropic works.

The comparison map about the distances computed along the local normal during the Period B (Figure 53a) highlights a well-defined area (black dashed oval) characterized by negative distances (around -0.4 m) in the upper part of the slope. The decomposition of the normal vector along the three principal axes (Figure 53b, c and d) points out a predominant movement in vertical direction (z-direction) for this sector.

With regard to positive distances, they are concentrated in a portion that extends along the slope (red dashed oval) reaching maximum values of 1.5 m. Furthermore, a positive stripe (characterized by value around 0.2-0.3 m) located on the left of the slope (indicated by an arrow) is observed and it probably due to the growth of the vegetation between the two surveys. Negative and positive values are also concentred at the bottom of the slope that corresponds to atrophic material removal and accumulation in the time interval between the two surveys.
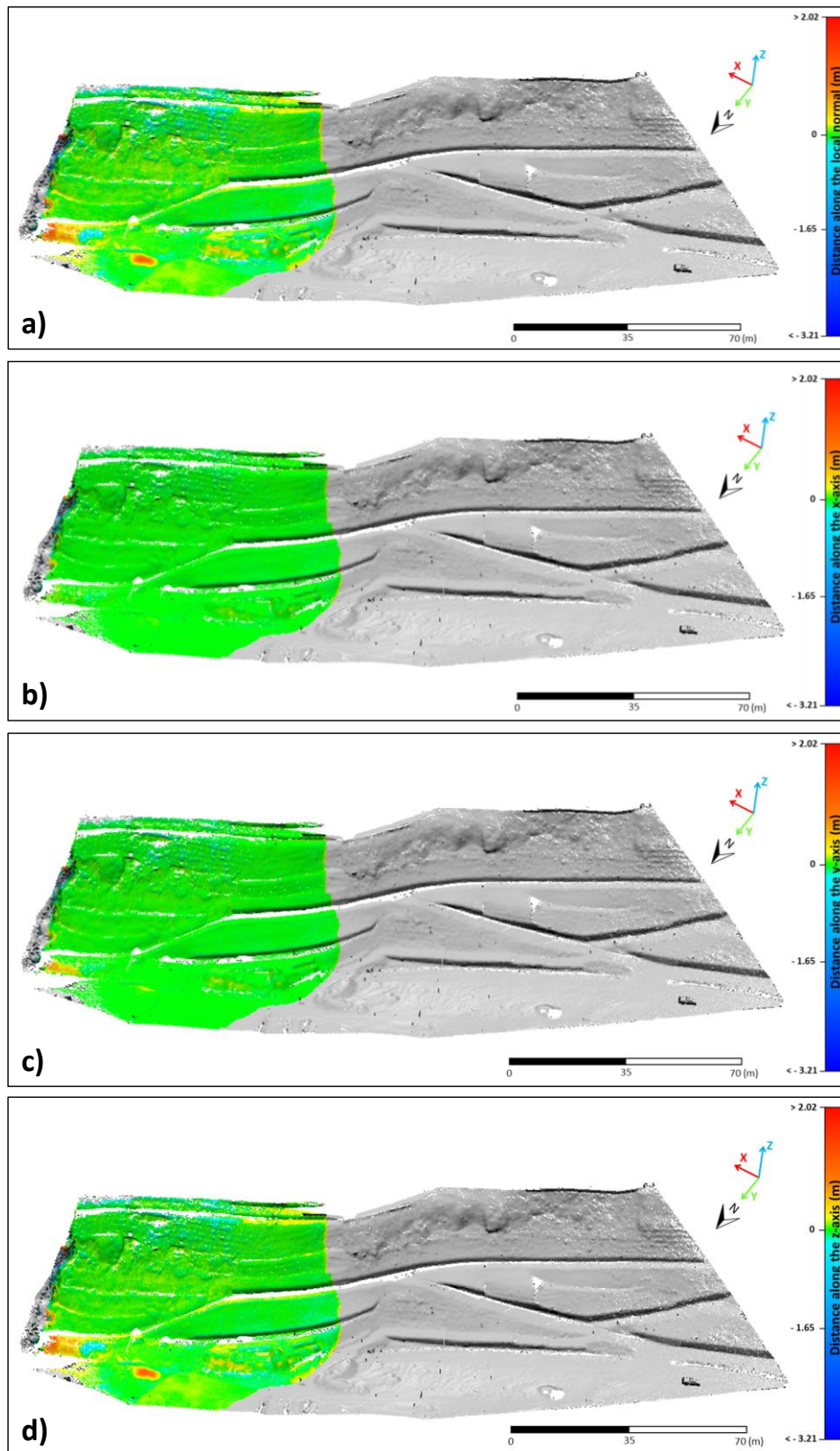
Figure 52. Point cloud comparison for Period A (30th March - 30st July 2015): a) distance along the local normal, b) distance along the x-axis, c) distance along the y-axis, d) distance along the z-axis.

Figure 53. Point cloud comparison for Period B (30th July 2015 – 2nd March 2016): a) distance along the local normal, b) distance along the x-axis, c) distance along the y-axis, d) distance along the z-axis.

Considering Period C (Figure 54), the positive values are only concentrated on small areas. Whereas negative distances are observed in different parts of the slope; in particular, two different areas can be distinguished (black dashed ovals) characterized by maximum values of about 0.5 m. Also in this case the movement is concentrated on vertical direction (see Figure 54b).

The last period of study (Period D, Figure 55) compares the first and the last UAV surveys and shows the areas characterized by negative distances and recognized within the Period A and Period B (black dashed ovals). In this case the upper central part reaches the maximum value of -0.68 m. About the positive values, the area recognized during the first survey is clearly visible (red dashed oval).

The effect of the vegetation between the analysed surveys is still present and indicated on the figure by an arrow.
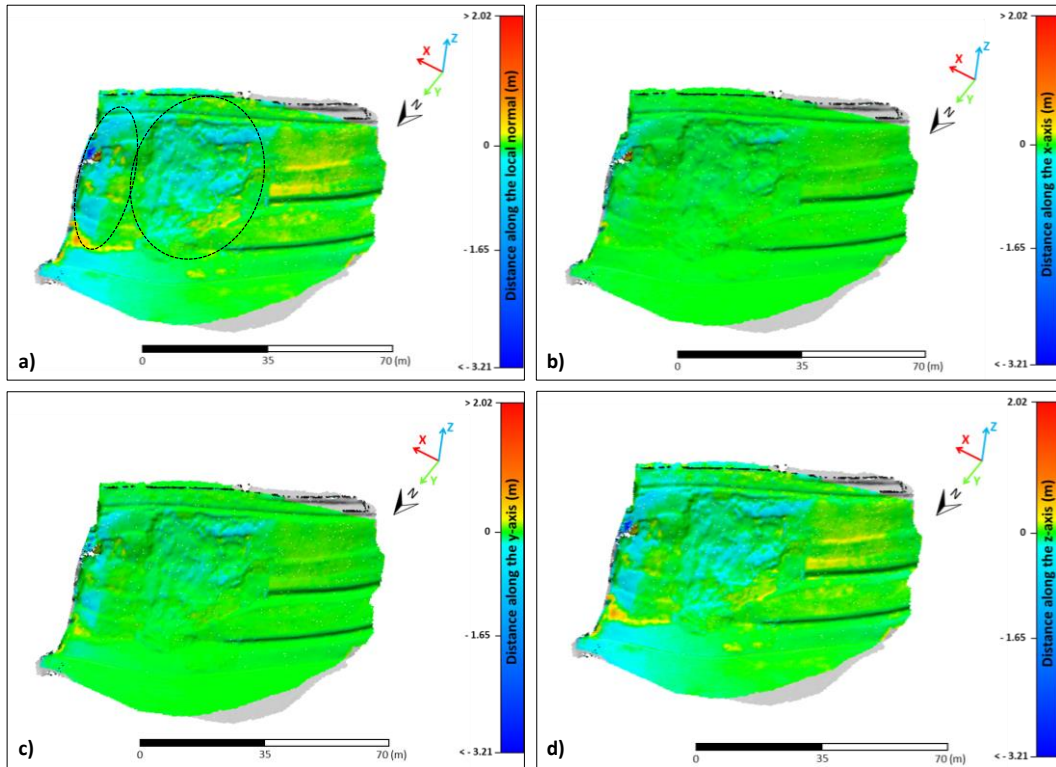
Figure 54. Point cloud comparison for Period C (2ⁿᵈ March – 6ᵗʰ April 2016): a) distance along the local normal, b) distance along the x-axis, c) distance along the y-axis, d) distance along the z-axis.
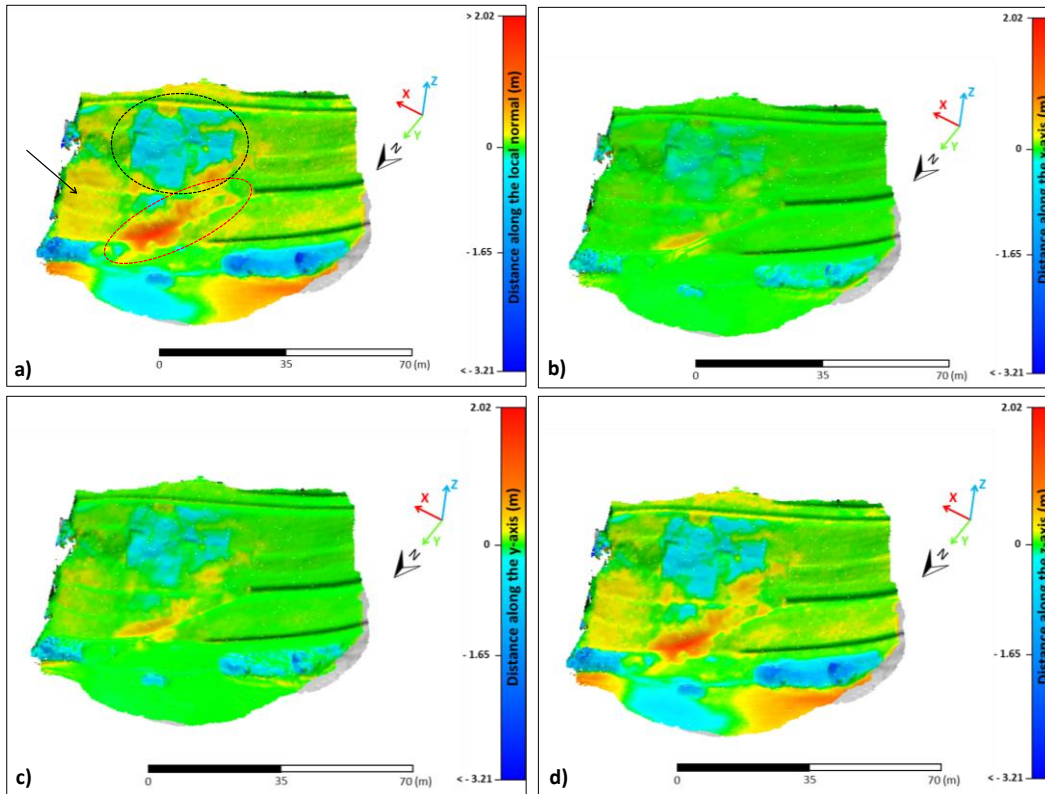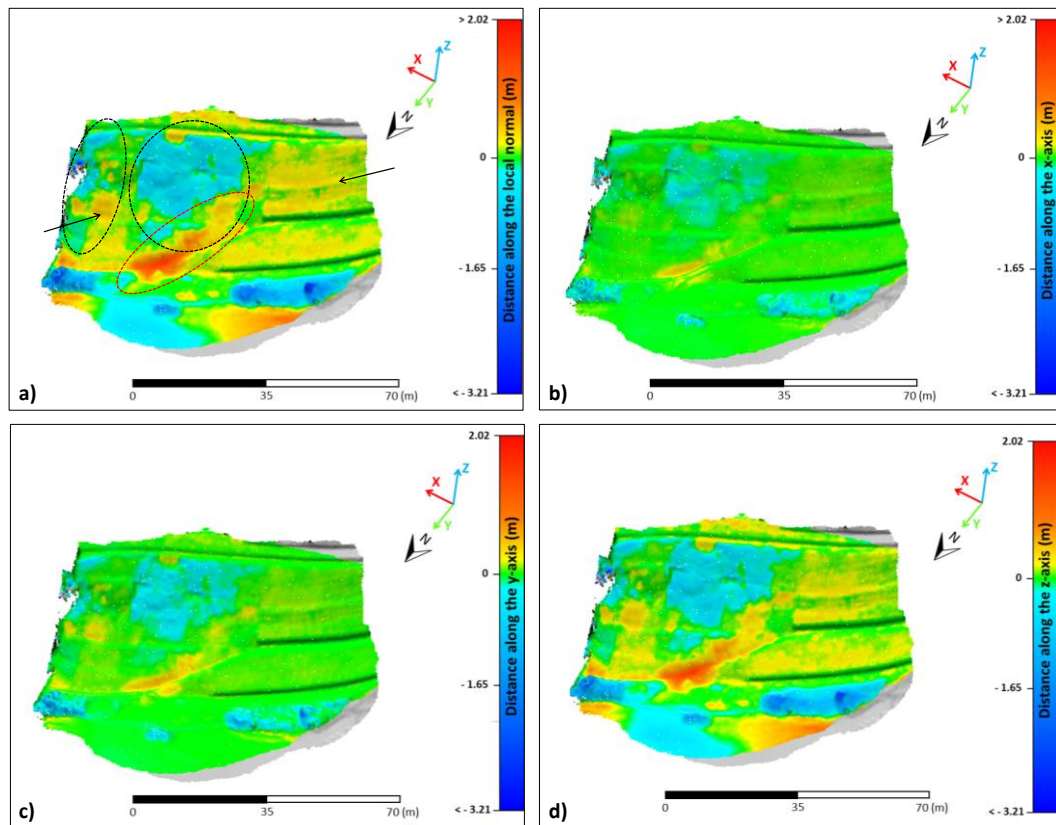

Figure 55. Point cloud comparison for Period D (30ᵗʰ July 2015 – 6ᵗʰ April 2016): a) distance along the local normal, b) distance along the x-axis, c) distance along the y-axis, d) distance along the z-axis.

Furthermore, the average distances for each period are presented (Figures from 56 to 59). The average distance values on the maps are associated to a colorbar, in which values around zero are shown in green; positive distances increasing (in module) from yellow to red; negative distances increasing (in module) from light blue to dark blue. The grey colour indicates no-distance value.
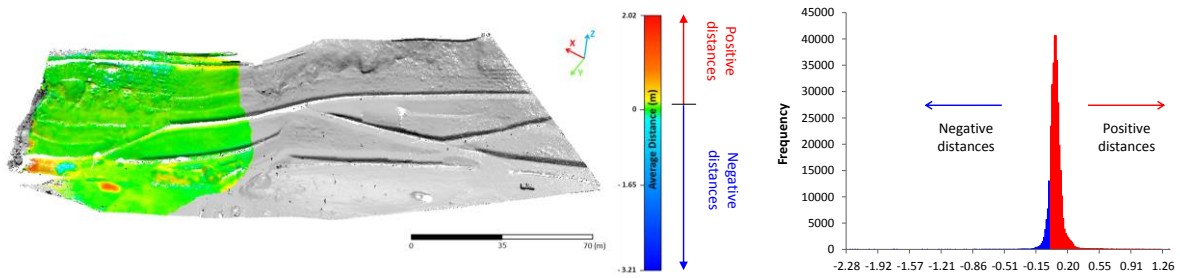
Figure 56. Average distance computed starting from distance along the local normal for Period A and related frequency histogram.
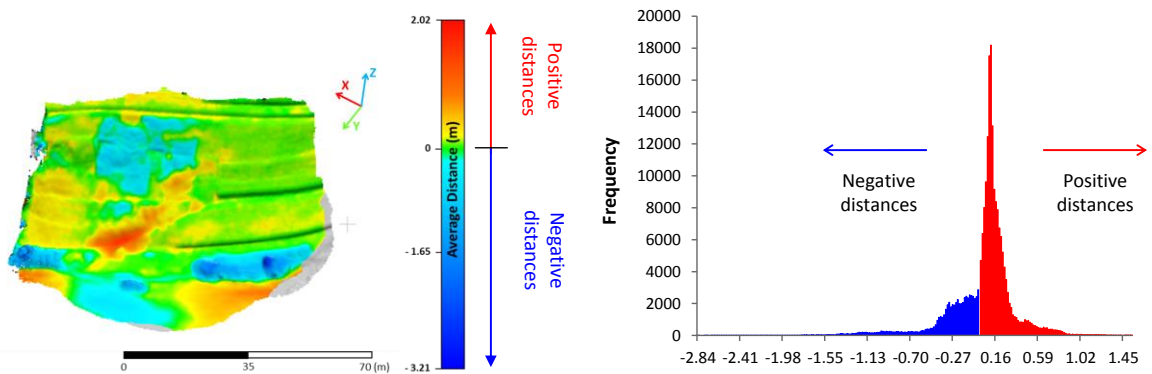
Figure 57. Average distance computed starting from distance along the local normal for Period B and related frequency histogram.
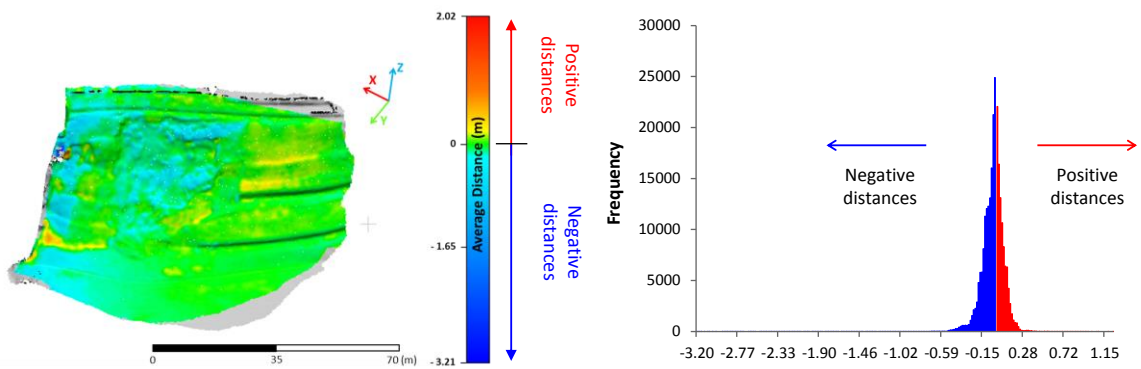
Figure 58. Average distance computed starting from distance along the local normal for Period C and related frequency histogram.
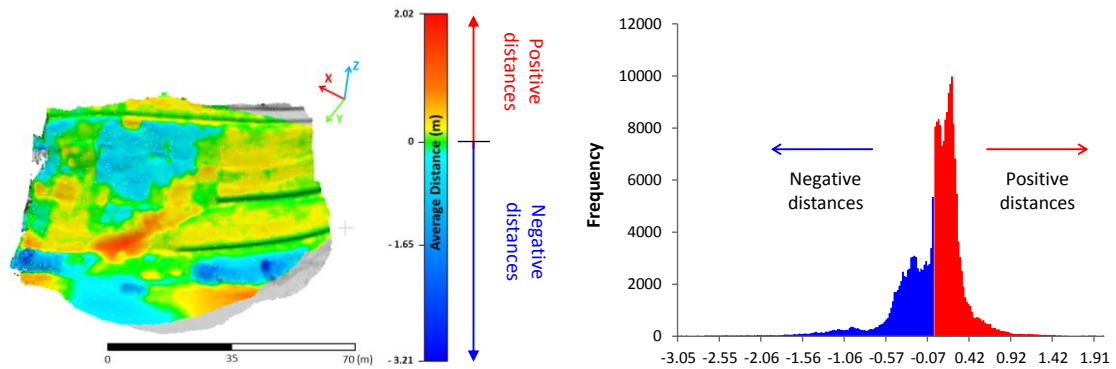
Figure 59. Average distance computed starting from distance along the local normal for Period D and related frequency histogram.

5.2.3.3 LoD and significant distances

Unlike San Leo test site, in the case of the clayey slope of Ricasoli village the choice of a minimum threshold as Level of Detection based on the analysis of the stable areas was not achievable. This is due to the presence of dense and uniform vegetation that cannot be easily removed and it does not permit to distinguish the changes from the vegetation. Indeed, because of the vegetation, the reconstruction of the ground below a dense coverage and the individuation of some stable areas is not simple and often impossible. Furthermore, this effect results in a diffuse increase of altitude in all the grassy areas (from 20 to 30 centimetres). For this reason, a threshold of 0.2 m was chosen as Level of Detection.

The resulting detachment and accumulation (blue zones) and deformation zones (red zones) are shown in Figure 60, in which can be distinguished the two instability phenomena interesting the slope.
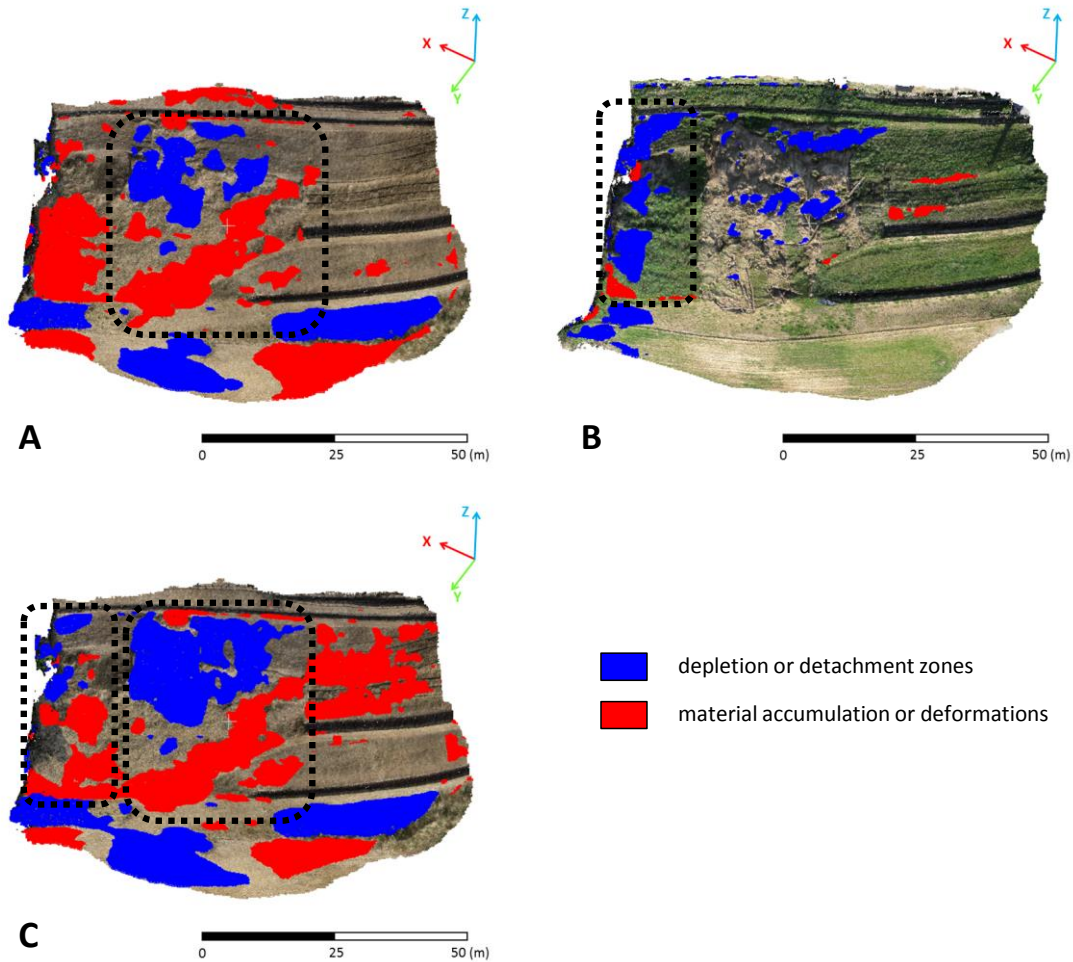
Figure 60. Depletion or detachment zones (in blue) and material accumulation or deformations (in red) for Period B (A), Period C (B), Period D (C).

5.2.3.4 Cluster analysis

To automatically segregate the significant distance zones outcoming from the cloud comparison, and to compute their area, a cluster analysis was performed within the Routine 2. Contrary to the movements affecting a rock mass that are characterized by distinct spatial distribution, the automatic isolation of detachment and accumulation zones on an earth slope is not simple as showed in Figure 61.
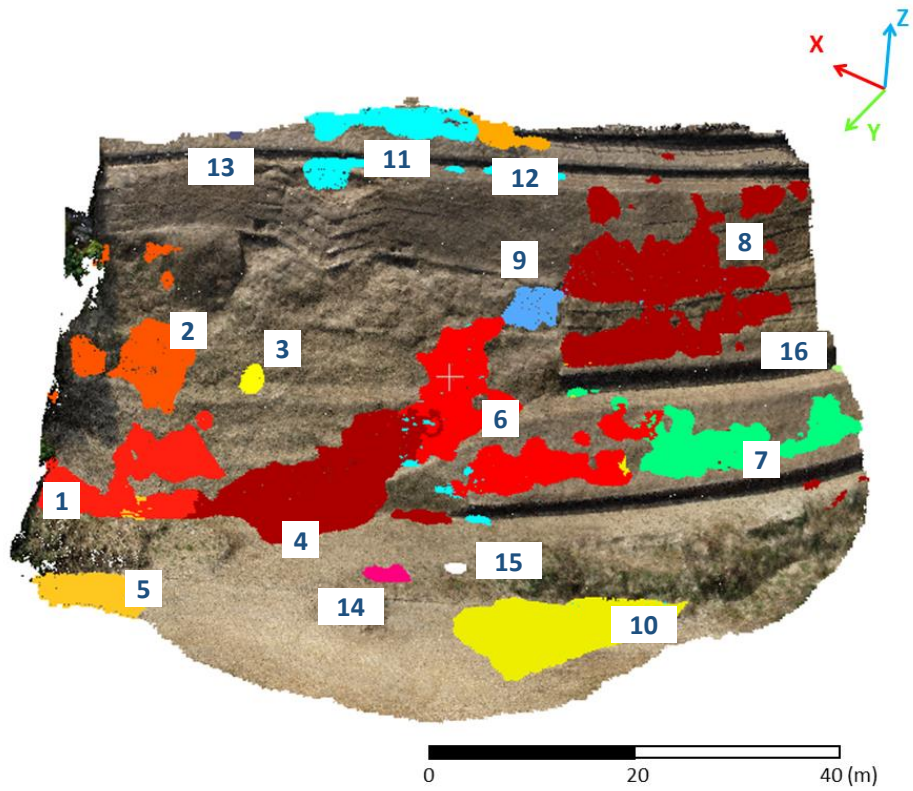
Figure 61. Cluster analysis results for recognized areas with positive distances in Ricasoli.

6. Discussion

The tool proposed in this study consists of two different routines that can be run separately. The Routine 1 was planned with the aim to achieve a morphometric characterization of the investigated unstable slope and therefore, to perform a comparison between the point cloud carried out at the first time and that one at the second time. The comparison is carried out based on distance computation and it provides, for each point of the first cloud, the distance along the local normal and its projection along *x*-axis, *y*-axis and *z*-axis. The Routine 2 permits to automatically isolate the significant distances and to compute the area of these significant zones. This is possible thanks to a cluster analysis, in which the level of detection is chosen by the user along with a multiplication factor that amplify the mean of the smallest Euclidean distances.

6.1 Applicability to test sites

The tool was applied to two test sites characterized by different geological setting and instability phenomena, San Leo rock mass and a clayey slope of Ricasoli village.

San Leo test site is a rock cliff historically affected by several types of landslides (rockfalls, earthflows and complex landslides). These are caused by its geological and geomorphological setting involving a rock slab overlying a soft clayey substratum. Among the most recent instability events, a large rock detachment (about 0.33 Mm^3), involving the north-eastern part of the cliff, occurred in 27th February 2014. In this case, the tool allowed to investigate the spatio-temporal changes that involved the north-eastern rock cliffafter the catastrophic event. To do this, the full period of monitoring, carried out by means of a Terrestrial Laser Scanner, was subdivided in four periods of study (Figure 26), in which each scan acquisition is compared to the first one.

The second test site is the morphological high of Ricasoli village historically interested by numerous instability phenomena. Subsequently to several shallow landslides that affected the northern slope of the village in the recent years, a TLS survey and three UAV surveys were performed to monitor the slope. The monitoring period is here subdivided in four periods of study (Figure 46) with the aim to compare, respectively TLS scan with the first UAV point cloud and the UAV surveys between them.

The azimuth and slope indices permit to rapidly characterise the investigated scenario, from a morphometric and geometrical point of view. Such parametrization is particularly useful to provide input data for stability analysis, based on these predisposing factors. Furthermore, local variations of these indices are useful to point out morphological elements of interest such as scarps, fractures and other possible feature can be related to ongoing processes on the slopes.

Regarding San Leo rock wall, the corresponding maps (Figure 27 and 28) pointed out a general orientation of the rock faces towards NE and SW and a slope angle mostly characterized by nearly vertical values, along with other limited portions with anomalous values, better characterized with the further steps of analysis.

In case of a subvertical cliff, like in San Leo site, it is important to underline that the investigated rock wall shows, in some portions, overhanging sectors that can barely be visible in the slope angle map since this latter represents only angle values with a range between 0 to 90° with respect to the horizontal plane, in absolute value.

The routine allows to extract another morphometric index that is the roughness (Figure 29). Since the roughness is characterized by a scale effect, as discussed in paragraph 4.1.2, it plays an important role, influencing the surface normal computation at the chosen R scale.

Indeed, the search neighbourhood cube half-side R should be not affected by smaller scale roughness, as suggested by Lague et al. (2013). For these reasons, the value of the roughness should be considered in the choice of a suitable half-side R of the neighbourhood cube, that must be aimed at minimize the effect of the small or large scale roughness and at capture the changes.

Furthermore, high roughness values on the surface can cause occlusions within the point cloud due to local shadowing effects, originating areas with lack of points or, however, inadequate point density.

The last output parameter of the point cloud analysis is the point density which variations within the map are primarily related to the distance between the sensor and the observed scenario. In the case of San Leo (Figure 30), the point cloud acquired using TLS is characterised by areas closer to the sensor with high density values (130 points per cubic meter) remarkably higher than the areas more far from the instrument. An exception is represented by an area in the central part of the cliff characterized by high values of density (around 90 points per

cubic meter) with respect to the surrounding portions. This is due to the influence of surface orientation with respect to the laser beam that is, in such a case, particularly favourable. On the other hand, in case of using photogrammetric point clouds (Ricasoli test site, Figure 51), the density is mainly related to the camera resolution, image quality (blurry or into focus images), image overlap and shooting altitude.

In both cases, a preliminary evaluation of the point density can be particularly useful to assess the expected quality of possible post processing elaborations such as DTMs or 3D polygonal models (e.g. mesh). In this case, the different point density can influence the further point cloud comparison, performed with the proposed tool.

Successively, Routine 1 allowed to perform a three-dimensional point cloud comparison for each of period of study. The proposed comparison approach is based on the computation of the distances between two point clouds along the local normal, as proposed in Lague et al. (2013); contrary to the methods proposed for example in Teza et al. (2007) or Monserrat and Crosetto (2008), which are based on same element and feature tracking within point clouds acquired in successive times (see chapter 3). The choice was driven by the difficulty to individuate the corresponding elements in different point clouds in an automatic way. This is true especially in the case of rough complex topographies, but also in the case of different conditions during the surveys, that can originate substantial differences in some portions of the compared point clouds, in terms of point density, shadowing, illumination and backscattering properties.

The surface normal-differences computation considers the dependence of the geomorphic processes (in particular landslide processes) on the surface geometry, especially in the case of rock movements. Indeed, for this category rigid body transformation can well express planar sliding as well as toppling movements.

Furthermore, the tool allows to investigate the components of the local normal distance along the three principal axes in a global reference system, corresponding to the north-direction (y-axis), east-direction (x-axis) and vertical direction (z-axis).

Among the factors influencing the comparison quality, vegetation coverage can create noisy areas in the point clouds. This is the case of some portions of San Leo cliff where some sparse bushes led to detect unnatural surface changes. Generally, regarding the point clouds obtained from TLS surveys, it can be possible to remove vegetation by using specific filtering

algorithm (e.g. Brodu et al. 2012) that could be based on the relative position between the points within a certain distance at a certain scale, based on the RGB values or, at least, manually. The application of such techniques and automatic algorithms is often effective when using laser scanning data, thanks to the capability of the laser beams to penetrate the vegetation foliage, but less effective on photogrammetric point clouds, especially in presence of a dense and uniform coverage.

The result of this effect is the impossibility of reconstruct precisely the terrain features, for example, below a dense grass coverage on the slope, grown between the surveys. This is the case of the northern slope of Ricasoli where a dense grass coverage is increased from the first to the second and the third surveys (this is well visible from optical images in Figure 46) preventing to triangulate points corresponding to the surface below. This effect resulted in a diffuse increase in altitude in all the grassy areas (from 20 to 30 centimetres), visible from the comparison process (Figures 53 and 55). Removing these points would lead to have widespread holes in the cloud while, isolated trees or sparser vegetation are generally easily removed by applying automatic filters and a manual refinement.

In this case, as well as leading to uncertain comparison results, such vegetation effect did not allow to point out fissures and other features of the ground, useful for precise landslide delimitation and characterization. However, the contribute of the vegetation can be significantly reduced with the use of a high-quality camera with higher resolution, stabilized and low distortion lenses, avoiding fish-eye effects and blurry images.

Considering these aspects, the output of the comparison process is point clouds coloured basing on the distance value associated to each point of the *reference* cloud. Depending on the type of monitored phenomena, positive and negative values can be interpreted as a result of different morphological processes in the investigated slopes. In particular, considering the San Leo cliff, positive values are due to displacements of isolated portions of the cliff and unstable blocks, moving towards the sensor. On the contrary, positive values in the case of Ricasoli can be related to both ongoing superficial deformations or accumulation of the already detached landslide deposits and, furthermore, to the previously described effect of the growing low vegetation.

Negative distance values are, as well as the positive ones, related to different morphological processes with respect to the case study. In San Leo, negative values are associated to areas

in which detachment of rock masses occurred between the different surveys, while in Ricasoli, areas with negative values are found to be related respectively to material detachment from the surface, to secondary ground deformations and by lack of vegetation.

Furthermore, from the point of view of the morphological characterization, the comparison map allows to identify the main landslide morphological elements such, as scarps (Figure 62), belonging to ongoing processes on the slopes.
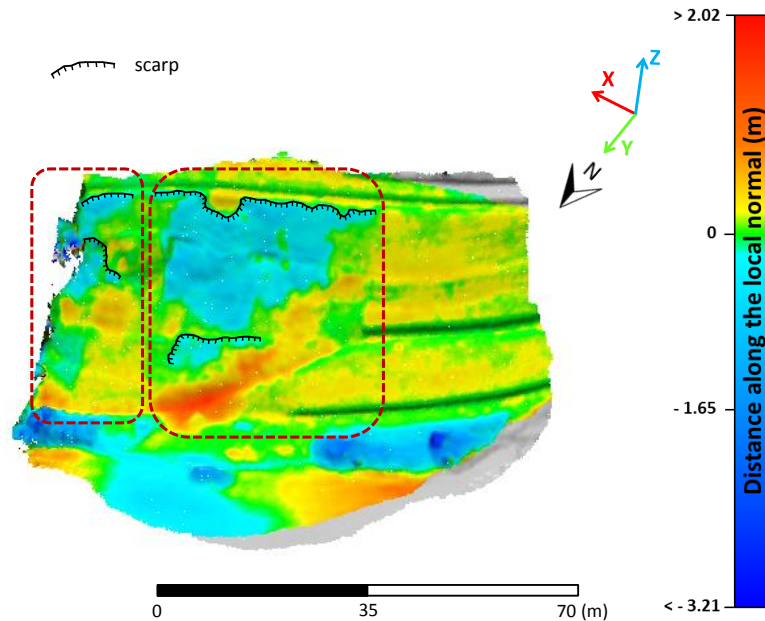
Figure 62. Point cloud comparison map for Period D (30th July 2015 – 6th April 2016) with the main landslide scarps and the recognized landslides (red dashed line).

The proposed approach revealed to be an efficient tool also to compare point clouds resulting by different sources (TLS and UAV), as shown for Ricasoli test site, as long as the point clouds are referred to the same global coordinate system. The results of the comparison are only a function of the sign convention, established by the user for the local normal vectors.

The change detection results can be affected also by random noise, due to roughness or instrumental errors as in the case of San Leo cliff where the influence of surface roughness is clearly visible on the highly irregular rock faces. Beyond the evident natural roughness of the test site, an artificial roughness resulting from survey design errors could occur. Thus, the averaging process is performed to reduce the effect of the random noise as formerly remarked by different authors (Abellán et al., 2009; Lague et al., 2013; Kromer et al., 2015). Indeed, the effect of roughness appears reduced in the resulting San Leo averaged distances (Figures from

35 to 38). Concerning the Ricasoli slope, the values of roughness are lower than those of San Leo cliff and the effect of this parameter on the comparison results is substantially null.

To distinguish real movements from noise, a minimum threshold is provided to Routine 2 as input parameter. Regarding San Leo test site, this level of detection was statistically calculated as the standard deviation of the distances computed on the areas considered stable during the full monitoring period. Therefore, fifteen distinct detachment zones and eight moving zones are extracted from the point cloud (Figure 41). Instead, in the case of Ricasoli slope, the dense vegetation did not allow to individuate perfectly stable areas and to discriminate, in some cases, the morphological changes from the effect of the vegetation. Thus, a threshold of 0.2 m was chosen considering an increase in altitude in the grassy area of 20-30 centimetres.

The application of cluster analysis to San Leo test site provides a good distinction of the different zones. A field survey was performed to observe and validate the rock block detachments and the instability areas (Figure 63).

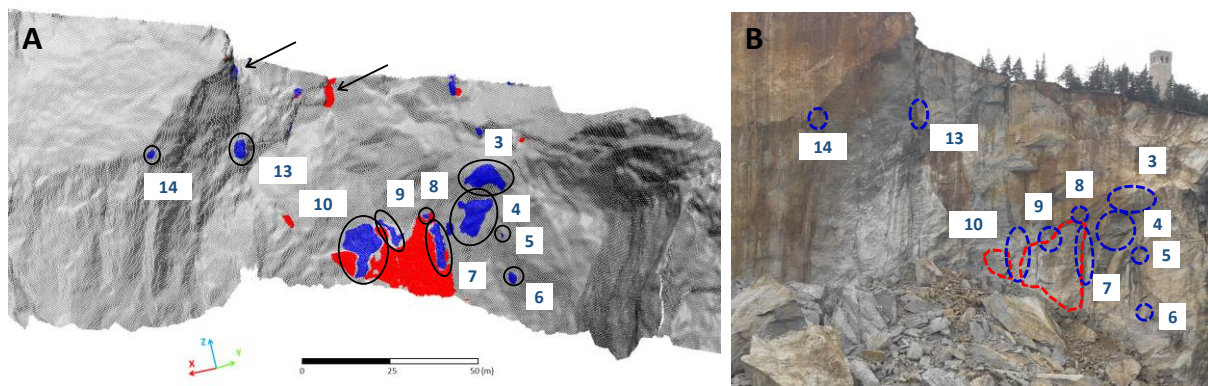*Figure 63. Location on optical image of the detachment and deformation zones.*

As shown in Figure 63, some areas (indicate by an arrow) represent uncertain results, these can be due to sampling bias due to occlusion areas that can induce artificially surface changes in points adjacent to occlusion itself. In fact, in the case of the two areas highlighted in Figure 64 the computed distances are close to shadow zones.
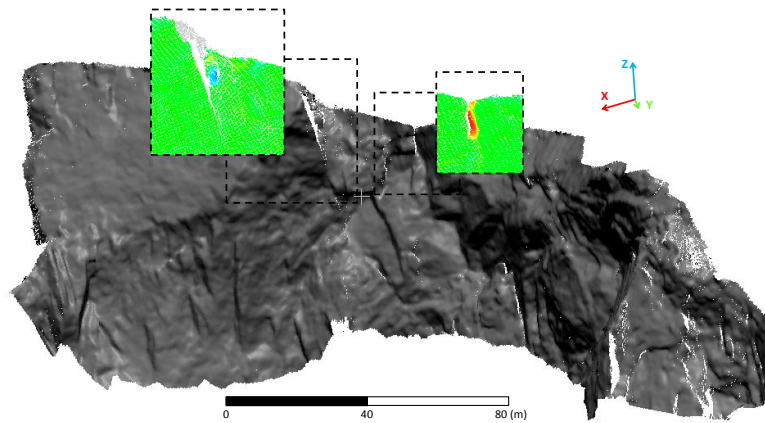
Figure 64. Possible uncertain results within San Leo cliff.

This spatial clustering process is more suitable for well-defined areas being based on the computation of Euclidean distances, but can provide unsatisfied results when a clear distinction between the several clusters does not occur, as in the case of Ricasoli test site. This is an aspect that must be deepened and improved.

Generally, laser scanning and digital photogrammetry can be effective tools for slope characterization and monitoring, especially thanks to their three-dimensionality aspect with respect to other remote sensing techniques. In the case of subvertical rock wall as in San Leo, GB-InSAR displacement data (see Figure 24) suffer from an ambiguity in locating deformations along the rock cliff due to system range resolution of scenario sectors locate at different heights along the investigated rock wall. The result is that the displacements are spread along the rock wall; the ambiguity increases in case of overhanging parts. Furthermore, TLS and photogrammetry data are not affected by decorrelation and they can be used to detect displacements also in directions oblique to the line of sight. On the other hand, GB-InSAR can reach submillimetre accuracy, while TLS and digital photogrammetry are generally less accurate (millimetre to centimetre), even if recent approaches (Kromer et al., 2015) taking advantage of point redundancy (in space and time domains), filtering and calibration processes, make it possible to achieve similar accuracy than radar systems.

The integrated use of TLS and GB-InSAR techniques is more convenient in the case of less steep slope as reported in **Annex 2**.

6.2 Advantages and drawbacks

The proposed tool represents an alternative for the morphometric characterization and surface change analysis from the comparison of point clouds obtaining from laser scanner and digital photogrammetry technologies. In closing, the tool returns a database including the number of recognized signed (positive and negative) zones and for each of these sectors: the features obtained by the point cloud analysis and comparison (that is azimuth, slope, local normal vector, roughness, point density, distance along the local normal, distance along the x-, y- and z-axis) and the area. Therefore, the procedure provides some information in terms of spatial and temporal evolution of unstable slope.

Regarding the morphometric features (azimuth, slope and roughness) and density extraction, the most common commercial geographic information system software, e.g. ArcMap software (www.esri.com), require the gridding or triangulation of the point cloud, which can result in a loss of information (as discussed in chapter 3), and the morphometric characteristics are calculated for each cell of the obtained raster. On the contrary, the tool presented in this thesis allows to compute these features for each set of points defined within a neighbourhood cube in a three-dimensional domain. In this regard, the three-dimensional information contained in a point cloud is fully exploited. The software permits the comparison between two surveys using DEM of difference method (see chapter 3), that provides the changes only along an one direction. This tool is opportune when the user is not interested in 3D knowledge and the vertical component represents the main component of the movement.

With regard to point cloud comparison, several distance calculation tools (described beforehand in chapter 3) implemented in most common software packages exist. Among them, RiSCAN PRO, the companion software for RIEGL Terrestrial 3D Laser Scanner Systems, contains the surface comparison tool with which the user can compare a point cloud to a reference mesh (C2M method). Indeed, this tool involves the triangulation of the point cloud chosen as reference one resulting in a time-consuming processing, in particular in the case of a huge amount of data.

Also, the open-source software CloudCompare includes different methods to compare two point clouds: C2C, C2M and M3C2. The advantages and the drawbacks of these tools were described in depth in chapter 3. Compared to *Cloud-to-Cloud* (C2C) method calculating the absolute distance, the proposed algorithm computes the signed (positive and negative)

distances allowing the distinction between detachment zones and accumulation or deformation zones. Both tools permit to obtain the distance values projected along the x-, y- and z- components. The *Cloud-to-Mesh* (C2M) method was discussed previously. Lastly, *Multiscale Model to Model Cloud Comparison* (M3C2) algorithm considers the average position of each core point within the reference cloud to compute the distance; on the contrary, the tool developed during this PhD course uses the original position of each point of the reference cloud to compute the signed distance. As highlighted by Kromer et al. (2015), the averaging process of the point cloud position can cause contrived results, for this reason the averaging of the distances was preferred.

The advantages and drawbacks of the tool applicability to selected test sites are shown in the previous paragraph.

7. Conclusions

The objective of this PhD research programme was to develop a semi-automatic analysis tool able to expeditiously investigate the significant spatio-temporal morphological changes in unstable slopes by comparing 3D point clouds, obtained by laser scanning and photogrammetry techniques, gathered at different epochs. This was possible through the MATLAB programming language.

During the last years, the use of point clouds in Earth Science environment has considerably increased (as confirmed by Abellán et al., 2016) and with it, the computational performance of computers and the development of new algorithms capable to process a huge amount of data, automatically or semi-automatically.

The point clouds allow to represent the topography of the observed scenario in three dimensions without gridding, meshing or triangulation process that can involve a loss of information and introduce a bias. The high resolution of these representations is due to their high measurement density that provides a huge redundancy of information about the investigated scene. The high detail of the represented surface permits to investigate the main morphometric characteristics of the investigated unstable slope, such as slope angle, azimuth angle and roughness, in three-dimensional space.

Therefore, during this three-years PhD programme, the effectiveness of point cloud exploitation for slope characterization and monitoring was tested and evaluated by applying a developed MATLAB tool. The tool was specifically designed to perform an automatic morphometric characterization and change detection analysis that allows to evaluate the movement affecting an unstable slope. Furthermore, a spatial cluster analysis routine based on significant distances was tested.

The tool was applied to two test sites characterized by different geological setting and instability phenomena: the San Leo rock cliff and the Ricasoli clayey slope. In the first case study, the terrestrial laser scanning acquisition of five scans of the investigated scenario allowed to analyse four monitoring period in the time span of almost one year and half. For these periods the significant detachment and deformations zones were individuated and for each one, the area was automatically computed. In the case of Ricasoli test site, a combined Terrestrial Laser Scanner and Unmanned Aerial Vehicles surveys allowed to recognise the

main detachment zones and the areas characterized by deformations or accumulation caused by two shallow landslides.

The proposed methodology proved to be an effective tool for a rapid assessment of slope instability since it is based only on point clouds, that is the primary raw product of laser scanner and photogrammetry technique. It is important to remark that a field validation is always recommended to validate the results of this semi-automatic process.

The future developments of the approach could involve the volume calculation of detached and accumulated zones and the related hazard zonation.

To conclude, the proposed procedure represents a rapid and effective basic change detection approach that can be further integrated and improved with a wide range of new modules and, additionally, a graphical user interface, to provide a standard analysis tool for common use.

8. References

Abbate E., 1983. Fluvial-Lacustrine Deposits of the Upper Valdarno. C.N.R., Firenze.

Abellán A., Calvet J., Vilaplana J. M., Blanchard J., 2010. Detection and spatial prediction of rockfalls by means of terrestrial laser scanner monitoring. Geomorphology 119(3): 162-171.

Abellán A., Derron M.H., Jaboyedoff M., 2016. "Use of 3D point clouds in geohazards" Special issue: current challenges and future trends. Remote Sensing 8.2: 130.

Abellán A., Jaboyedoff M., Oppikofer T., Vilaplana J.M., 2009. Detection of millimetric deformation using a terrestrial laser scanner: experiment and application to a rockfall event. Natural Hazards and Earth System Science 9: 365-372.

Abellán A., Oppikofer T., Jaboyedoff M., Rosser N.J., Lim M., Lato M., 2014. Terrestrial laser scanning of rock slope instabilities. Earth Surf. Process. Landforms 39: 80-97.

Abellán, A.; Vilaplana, J.; Calvet, J.; García-Sellés, D.; Asensio, E., 2011. Rock fall monitoring by Terrestrial Laser Scanning—Case study of the basaltic rock face at Castellfollit de la Roca (Catalonia, Spain). Nat. Hazard. Earth Syst. 11: 829–841.

Agisoft LLC: Agisoft PhotoScan Professional v. 1.2.4, available at http://www.agisoft.com/

Angeli M.G., Pasuto A., Silvano S., 2000. A critical review of landslide monitoring experiences. Engineering Geology 55: 133-147.

Antova G., 2015. Registration process of laser scan data in the field of deformation monitoring. In: Procedia Earth and Planetary Science, volume 15: 549–552.

Aryal A., Brooks B.A., Reid M.E., Bawden G.W., Pawlak G.R., 2012. Displacement fields from point cloud data: Application of particle imaging velocimetry to landslide geodesy. Journal of Geophysical Research 117(F1).

Baily B., Collier P., Farres P., Inkpen R., Pearson A., 2003. Comparative assessment of analytical and digital photogrammetric methods in the construction of DEMs of geomorphological forms. Earth Surface Processes and Landforms 28: 307-320.

Bae K.H., Lichti D.D., 2008. A method for automated registration of unorganised point clouds. ISPRS Journal of Photogrammetry and Remote Sensing 63(1): 36-54.

Bamler R., Hartl P., 1998. Synthetic aperture radar interferometry. Inverse Probl. 14: 1–54.

Barbarella M., Fiani M., 2013. Monitoring of large landslides by Terrestrial Laser Scanning techniques: field data collection and processing. European Journal of Remote Sensing 46: 126-151.

Barla G., Antolini F., Barla M., Mensi E., Piovano G., 2010. Monitoring of the Beauregard landslide (Aosta Valley, Italy) using advanced and conventional techniques. Engineering Geology 116: 218-235.

Barnhart T. B., Crosby B. T., 2013. Comparing two methods of surface change detection on an evolving thermokarst using high-temporal-frequency terrestrial laser scanning, Selawik River, Alaska. Remote Sensing, 5: 2813-2837.

Beckmann P., 1965. Signal degeneration in laser beams propagated through a turbulent atmosphere. J. Res. Nat. Bur. Stand. Sect. D., Radio Sci 69D: 629.

Benedetti G., Bernardi M., Borgatti L., Continelli F., Ghirotti M., Guerra C., Landuzzi A., Lucente C.C., Marchi G., 2013. San Leo: centuries of coexistence with landslides. In: Margittini C., Canuti P., Sassa K. (Eds), Landslide Science and Practice. Springer, Heidelberg, Germany, pp. 529-537.

Besl P.J., McKay N.D., 1992. Method for registration of 3-D shapes. In: Robotics-DL tentative (pp. 586-606). International Society for Optics and Photonics.

Bitelli G., Dubbini M., Zanutta A., 2004. Terrestrial laser scanning and digital photogrammetry techniques to monitor landslide bodies. ISPRS – Int. Arch. Photogram. Remote Sens. Spatial Inform. Sci. 35: 246-251.

Blasone G., Cavalli M., Marchi L., Cazorzi F., 2014. Monitoring sediment source areas in a debris-flow catchment using terrestrial laser scanning. Catena, 123: 23-36.

Boike J., Yoshikawa K., 2003. Mapping of periglacial geomorphology using kite/balloon aerial photography. Permafrost and Periglacial Processes 14: 81–85.

Borgatti L., Guerra C., Nesci O., Romeo R.W., Veneri F., Landuzzi A., Benedetti G., Marchi G., Lucente C.C., 2015. The 27 February 2014 San Leo landslide (northern Italy). Recent Landslides 12: 387-394.

Borgatti L., Soldati M., 2010. Landslides as a geomorphological proxy for climate change: a record from the dolomites (Northern Italy). Geomorphology. 120: 56-64.

Borkowski A., Perski Z., Wojciechowski T., JóźkóW G., Wójcik A., 2011. Landslides mapping in Roznow Lake vicinity, Poland using airborne laser scanning data. Acta Geodyn. Geomater. 8: 325–333.

Bossi G., Cavalli M., Crema S., Frigerio S., Quan Luna B., Mantovani M., Marcato G., Schenato L., Pasuto A., 2015. Multi-temporal LiDAR-DTMs as a tool for modelling a complex landslide: a case study in the Rotolon catchment (eastern Italian Alps). Natural Hazards and Earth System Sciences 15(4): 715-722.

Brasington J., Wheaton J.M., Vericat D., Hodge R., 2007. Modelling braided river morphodynamics with terrestrial laser scanning. In AGU Fall Meeting Abstracts (Vol. 1, p. L02).

Brodu N., Lague D., 2012. 3D terrestrial LiDAR data classification of complex natural scenes using a multi-scale dimensionality criterion: applications in geomorphology. ISPRS Journal of Photogrammetry and Remote Sensing 68: 121-134.

Burns W.J., Coe J.A., Kaya B.S., Ma L., 2010. Analysis of elevation changes detected from multi-temporal LiDAR surveys in forested landslide terrain in western Oregon. Environmental & Engineering Geoscience 16(4): 315-341.

Canuti P., Casagli N., Ermini L., Fanti R., Farina P., 2004. Landslide activity as a geoindicator in italy: significance and new perspectives from remote sensing. Environmental Geology. 45(7): 907-919.

Cardenal J., Mata E., Perez-Garcia J. L., Delgado J., Andez M., Gonzalez A., Diaz-de-Teran J.R., 2008. Close range digital photogrammetry techniques applied to landslide monitoring. International Archives of Photogrammetry, Remote Sensing and Spatial Information Sciences 37.

Carvajal F., Agüera F., Pérez M., 2011. Surveying a landslide in a road embankment using unmanned aerial vehicle photogrammetry. ISPRS – Int. Arch. Photogramm. Remote Sens. Spatial Inform. Sci. XXXVIII-1/C22, 201–206.

Chandler J., 1999. Effective application of automated digital photogrammetry for geomorphological research. Earth Surface Processes and Landforms 24: 51-63.

Chang-chun L., Guang-sheng Z., Tian-jie L., A-du G., 2011. Quick image-processing method of UAV without control points data in earthquake disaster area. Trans. Nonferrous Met. Soc. China 21: 523-528.

Chen Y., Medioni G., 1992. Object modelling by registration of multiple range images. Image and Vision Computing 10(3): 145-155.

Cignoni P., Rocchini C., 1998. Metro: measuring error on simplified surfaces. Computer graphics Forum 17 (2): 167-174.

Colomina I., Molina P., 2014. Unmanned aerial systems for photogrammetry and remote sensing: A review. ISPRS Journal of Photogrammetry and Remote Sensing 92: 79–97

Conti S., 1989. Geologia dell'Appennino marchigiano romagnolo tra le valli del Savio e del Foglia (Note illustrative alla carta geologica a scala 1:50.000). Boll. Soc. Geol. It. 108: 453-490.

Conti S., 2002. Palaeogeographic implications and relations between tectonics and sedimentation in satellite basins (northern Apennines): insights from Neogene Epiligurian arcs. Bollettino della Società Geologica Italiana Vol. Volume Speciale 1: 353-364.

Conti S., Tosatti G., 1996. Tectonic vs gravitational processes affecting Ligurian and Epiligurian units in the Marecchia valley (northern Apennines). Mem. Sci. Geol. 48: 107-142.

Cornamusini G., Conti P., Bonciani F., Callegari I., Carmignani L., Martelli L., Quagliere S., 2010. Note illustrative della carta Geologica d'Italia. Foglio 267 San Marino, scala 1:50.000 (pp. 125). Roma: ISPRA.

Corsini A. Borgatti L., Cervi F., Dahne A., Ronchetti F., Sterzai P., 2009a. Estimating mass-wasting processes in active earth slides – earth flows with time-series of High-Resolution DEMs from photogrammetry and airborne LiDAR. Natural Hazards and Earth System Sciences 9: 433-439.

Corsini A., Cervi F., Daehne A., Ronchetti F., 2009b. Coupling geomorphic field observation and LIDAR derivatives to map complex landslides. In: Landslides Processes—From Geomorphologic Mapping to Dynamic Modelling; Malet, J.P., Remaître, A., Bogaard, T., Eds.; CERG Editions: Strasbourg, France, pp. 15–18.

Corominas J., Moya J., Lloret A., Gili J.A., Angeli M.G., Pasuto A., Silvano S., 2000. Measurement of landslide displacments using a wire extensometer. Engineering Geology 55: 149-166.

Cruden D.M., 1991. A simple definition of a landslide. Bullettin of Engineering Geology and the Environment, 43 (1): 27-29.

Cruden D.M., Varnes D.J., 1996. Landslide types and processes. In: Turner AK, Schuster R.L., (eds) Landslides: Investigation and Mitigation, Sp. Rep. 247, Transportation Research Board, National research Council. National Academy Press, Washington DC, 36-75.

Daehne A., Corsini A., 2013. Kinematics of active earthflows revealed by digital image correlation and DEM subtraction techniques applied to multi-temporal LiDAR data. Earth Surface Processes and Landforms 38(6): 640-654.

Dandois J.P., Ellis E.C., 2010. Remote sensing of vegetation structure using computer vision. Remote Sensing 2: 1157-1176.

De Feyter A.J., 1991. Gravity tectonics and sedimentation of the Montefeltro (Italy). Geol. Ultraiect. 35: 1-168.

DeLong S.B., Prentice C.S., Hilley G.E., Ebert Y., 2012. Multitemporal ALSM change detection, sediment delivery, and process mapping at an active earthflow. Earth Surface Processes and Landforms 37(3): 262-272.

Demmel J.W., 1997. Applied Numerical Linear Algebra, SIAM, Philadelphia.

Đomlija P., Bernat S., Mihalić Arbanas S., Benac Č., 2014. Landslide inventory in the area of Dubračina River Basin (Croatia). In Landslide Science for a Safer Geoenvironment; Sassa K., Canuti P., Yin Y., Eds.; Springer: Berlin, Germany, 2014; Volume 2, pp. 837–842.

Duffy G.P., Hughes-Clarke J.E., 2005. Application of spatial cross correlation to detection of migration of submarine sand dunes. J. Geophys. Res. 110: 1-11.

Duffy G.P., Hughes-Clarke J.E., Parrott R., 2004. Application of current measurement and time lapsed bathymetric multibeam surveying to investigation of a banner bank, Mispec Bay, New Brunswick, Canada. In Marine Sandwave Dynamics and River Dune Dynamics II. Edited by Hulscher, SJMH, Garlan, T., Idier, D. International Workshop, University of Twente, Enschede, The Netherlands, pp. 72-78.

Dunham W., 1990. Heron's Formula for Triangular Area. Ch. 5 in Journey through Genius: The Great Theorems of Mathematics. New York: Wiley, pp. 113-132.

EDF R&D, T.P., 2011. CloudCompare (version 2.6) [GPL software]. Retrieved from http://www.danielgm.net/cc/.

Eisenbeiss H., 2008. The autonomous mini helicopter: a powerful platform for mobile mapping. Int. Arch. Photogramm. Remote Sens. Spat. Inf. Sci 37: 977-983.

Eisenbeiss H., Sauerbier M., 2011. Investigation of uav systems and flight modes for photogrammetric applications. The Photogrammetric Record 26(136): 400–421.

Eisenbeiss H., Zhang L., 2006. Comparison of DSMs generated from mini UAV imagery and terrestrial laser scanner in a cultural heritage application. International Archives of Photogrammetry, Remote Sensing and Spatial Information Sciences XXXVI-5, 90e96.

Fan Y.B., Yang S.W., Xu L.K., Li S.H., Feng C., Liang B.F., 2016. Real-time monitoring instrument designed for the deformation and sliding period of colluvial landslides. Bulletin of Engineering Geology and the Environment, 1-10.

Fanti R., Gigli G., Lombardi L., Tapete D., Canuti P., 2013. Terrestrial laser scanning for rockfall stability in the cultural heritage site of Pitigliano (Italy). Landslides: 1-12.

Fey C., Wichmann V., 2016. Long-range terrestrial laser scanning for geomorphological change detection in alpine terrain handling uncertainties. Earth Surf. Process. Landforms. doi: 10.1002/esp.4022

Fell R., 1994. Landslide risk assessment and acceptable risk. Canadian Geotechnical Journal, 1994, 31(2): 261-272, 10.1139/t94-031

Fidolini F., Ghinassi M., Magi M., Papini M. and Sagri M., 2013. The Plio-Pleistocene Fluvio-Lacustrine Upper Valdar—no Basin (Central Italy): Stratigraphy and Basin Fill Evolution. Italian Journal of Geosciences (32): 13–32.

Forlani G., Pinto L., Roncella R., Pagliari D., 2014. Terrestrial photogrammetry without ground control points. Earth Science Informatics 7(2): 71-81.

Frodella W., Ciampalini A., Gigli G., Lombardi L., Raspini F., Nocentini M., Scardigli C., Casagli N., 2016. Synergic use of satellite and ground based remote sensing methods for monitoring the San Leo rock cliff (Northern Italy). Geomorphology 264: 80-94.

Frohlich C., Mattenleiter M., 2004. Terrestrial laser scanning – new perspectives in 3D surveying. International Archivies of Photogrammetry, Remote Sensing and Spatial Information Sciences 36, Part 8:W2.

Furukawa Y., Ponce J., 2009. Accurate, dense, and robust multi-view stereopsis. IEEE Trans. Pattern Anal., 32: 1362–1376.

Giardino M., Mortara G., Borgatti L., Nesci O., Guerra C., Lucente C.C., 2015. Dynamic geomorphology and historical iconography. Contributions to the knowledge of environmental changes and slope instabilities in the Apennines and the alps. In: Lollino G., Giordan D., Marunteanu C., Christaras B., Yoshinori I., Margottini C. (Eds), Engineering Geology for Society and Territory Vol. Volume 8. Springer International Publishing, pp. 463-468.

Gigli G., Casagli N., 2011. Semi-automatic extraction of rock mass structural data from high resolution LIDAR point clouds. International Journal of Rock Mechanics and Mining Sciences 48: 187-198.

Gigli G. Fodella W., Garfagnoli F., Morelli S., Mugnai F., Menna F., Casagli N., 2013. 3-D geomechanical rock mass characterization for the evaluation of rockslide susceptibility scenarios. Landslides: 1:10.

Gigli G., Morelli S. Fornera S., Casagli N., 2014. Terrestrial laser scanner and geomechanical surveys for the rapid evaluation of rock fall susceptibility scenarios. Landslides 11: 1-14.

Girardeau-Montaut D., Roux M., Marc R., Thibault G., 2005. Change detection on point cloud data acquired with a ground laser scanner. International Archives of Photogrammetry, Remote Sensing and Spatial Information Sciences 36.part 3 (2005): W19.

Golub G.H., Van Loan C.F., 1980. An analysis of the total least squares problem. In SIAM Journal on Numerical Analysis 17(6): 883-893.

Golub G.H., Van Loan C.F., 1996. Matrix computation, 3rd ed., Academic Press, Boston.

Golub G.H., Reinsch C., 1970. Singular value decomposition and least squares solutions. Numerische Mathematik 14: 403-420.

Gopi S., 2007. Advanced Surveying: Total Station, GIS and Remote Sensing. Pearson Education India.

Gruen A., Akca D., 2005. Least squares 3D surface and curve matching. ISPRS Journal of Photogrammetry and Remote Sensing 59(3): 151-174.

Grussenmeyer P., Landes T., Voegtle T., Ringle K., 2008. Comparison methods of terrestrial laser scanning, photogrammetry and tacheometry data for recording of cultural heritage buildings. ISPRS Arch. Photogramm. Remote Sens 37, W5.

Guarnieri A., Pirotti F., Vettore A., 2012. Comparison of discrete return and waveform terrestrial laser scanning for dense vegetation filtering. International Archives of the Photogrammetry, Remote Sensing and Spatial Information Sciences 39(B7): 511-516.

Guzzetti F., Peruccacci S., Rossi M., Stark C.P., 2008. The rainfall intensity-duration control of shallow landslides and debris flows: an update. Landslides, 5(1): 3-17.

Harwin S., Lucieer A., 2012. Assessing the accuracy of georeferenced point clouds produced via multi-view stereopsis from Unmanned Aerial Vehicle (UAV) imagery. Remote Sensing 4: 1573-1599.

Hodge R.A., 2010. Using simulated terrestrial laser scanning to analyse errors in high-resolution scan data of irregular surfaces. ISPRS Journal of Photogrammetry and Remote Sensing 65: 227-240.

Hutchinson D. J., Lato M., Gauthier D., Kromer R., Ondercin M., van Veen M., Harrap R., 2015. Applications of remote sensing techniques to managing rock slope instability risk. Geoquébec 2015.

IGOS GEOHAZARDS, 2004. Geohazards theme report: for the monitoring of our environment from space and from earth. European Space Agency Publication, pp 55.

Intrieri E., Gigli G., Mugnai F., Fanti R., Casagli N., 2012. Design and implementation of a landslide early warning system. Engineering Geology 147-148: 124-136.

Jaboyedoff M., Metzger R., Oppikofer T., Couture R., Derron M.H., Locat J., Durmel D., 2007. New insight techniques to analyze rock-slope relief using DEM and 3D- imaging cloud points: COLTOP-3D software. In: Eberhardt, E., Stead, D., Morrison, T. (Eds.) Rock mechanics: meeting society's challenges and demands, Taylor & Francis Group, London, pp 61–68

Jaboyedoff M., Oppikofer T., Abellán A., Derron M.H., Loye A., Metzger R., Pedrazzini A.,2012. Use of LiDAR in landslides investigations: a review. Natural Hazard 61: 5-28.

Jaboyedoff M., Oppikofer T., Locat A., Locat J., Turmel D., Robitaille D., Demers D., Locat P., 2009. Use of ground-based LIDAR for the analysis of retrogressive landslides in sensitive clay and of rotational landslides in river banks. Can Geotech J 46:1379–1390. doi:10.1139/T09-073

Jakob M., Lambert S., 2009. Climate change effects on landslides along the south-west coast of British Columbia. Geomorphology. 107, 275-284.

James M.R., Robson S., 2012. Straightforward reconstruction of 3D surfaces and topography with a camera: Accuracy and geoscience application. Journal of Geophysical Research 117, f03017. doi:10.1029/2011jf002289

Kromer R.A., Abellán A., Hutchinson D.J., Lato M., Edwards T., Jaboyedoff M., 2015. A 4D filtering and calibration technique for small-scale point cloud change detection with a terrestrial laser scanner. Remote Sens. 7: 13029-13052. doi:10.3390/rs71013029

Lane S.N., James T.D., Crowell M.D., 2000. Application of digital photogrammetry to complex topography for geomorphological research. Photogrammetric Record 16: 793-821.

Lane S.N., Westaway R.M., Hicks D.M., 2003. Estimation of erosion and deposition volumes in a large, gravel-bed, braided river using synoptic remote sensing. Earth Surface Processes and Landforms 28 (3): 249-271.

Lalonde J.F., Unnikrishnan R., Vandapel N., Hebert M., 2005. Scale selection for classification of point-sampled 3-D surfaces. Proceeedings of the fifth international conference on 3-D digital imaging and modelling: 285-292.

Lague D., Brodu N., Leroux J., 2013. Accurate 3D comparison of complex topography with terrestrial laser scanner: Application to the Rangitikei canyon (N-Z). ISPRS J. Photogramm. Remote Sens. 82: 10-26.

Lato M., Diederichs M., Hutchinson D.J., Harrap R., 2009. Optimization of LiDAR scanning and processing for automated structural evaluation of discontinuities in rock masses. Int J Rock Mech Min 46: 194–199

Lato M., Diederichs M., Hutchinson D.J., 2010. Bias correction for static LiDAR scanning of rock outcrops for structural characterization. Rock Mechanics and Rock Engineering 43(5): 615-628.

Lay D.C., 2002. Linear Algebra and Its Applications (3rd edition). Addison-Wesley.

Lejot J., Delacourt C., Piégay H., Fournier T., Trémélo M.L., Allemand P., 2007. Very high spatial resolution imagery for channel bathymetry and topography from an unmanned mapping controlled platform. Earth Surface Processes and Landforms 32: 1705–1725.

Lichti D.D., Gordon S.J., Tipdecho T., 2005. Error models and propagation in directly georeferenced terrestrial laser scanner networks. Journal of surveying engineering 131 (4): 135-142.

Lichti D., Skaloud J., 2010. Registration and calibration. In: Airborne and Terrestrial Laser Scanning; Whittles Publishing: Dunbeath, UK; pp. 83-133.

Lombardi L., Casagli N., Gigli G., Nocentini M., 2006. Verifica delle condizioni di sicurezza della S.P. Lodovica in seguito ai fenomeni di crollo nella cava di Sesto di Moriano (Lucca), Giornale di Geologia Applicata, AIGA, 3: 249-256 [In Italian].

Lucieer A., De Jong S., Turner D., 2014. Mapping landslide displacements using Structure from Motion (SfM) and image correlation of multi-temporal UAV photography. Progress in Physical Geography February 2014 vol. 38 no. 1 97-116.

Lucieer A., Robinson S., Turner D., 2011. Unmanned Aerial Vehicle (UAV) Remote Sensing for Hyperspatial Terrain Mapping of Antarctic Moss Beds Based on Structure from Motion (SFM) Point Clouds. In: Proceedings of the 34th International Symposium for Remote Sensing of the Environment (ISRSE), Sydney, Australia, 10–15 April 2011.

Luzi G., 2010. Ground based SAR interferometry: a novel tool for geoscience. INTECH Open Access Publisher.

Mallet C., Bretar F., 2009. Full-waveform topographic lidar: State-of-the-art. ISPRS J Photogramm Remote Sens 64:1-16.

Marzolff I., Ries J.B., Albert K.D., 2003. Kite aerial photography for gully monitoring in Sahelian landscapes. Proceedings of the Second Workshop of the EARSeL Special Interest Group on Remote Sensing for Developing Countries, pp. 2–13. 18–20 September, Bonn, Germany.

Milan D.J., Heritage G.L., Hetherington D., 2007. Application of a 3D laser scanner in the assessment of erosion and deposition volumes and channel change in a proglacial river. Earth Surface Processes and Landforms 32 (11): 1657-1674.

Mitra N.J., Nguyen A., 2003. Estimating surface normals in noisy point cloud data. Proceedings of the nineteenth conference on Computational geometry: 322-328.

Monserrat O., Crosetto M., 2008. Deformation measurement using terrestrial laser scanning data and least squares 3D surface matching. ISPRS Journal of Photogrammetry and Remote Sensing 63: 142-154.

Muller N., Magaia L., Herbst B.M., 2004. Singular value decomposition, Eigenfaces, and 3D Reconstructions. SIAM Rev. 46(3): 518-545.

Nadim F., Kjekstad O., Peduzzi P., Herold C., Jaedicke C., 2006. Global landslide and avalanche hotspots. Landslides 3: 159–173.

Niethammer U., James M.R., Rothmund S., Travelletti J., Joswig W., 2012. UAV-based remote sensing of the Super Sauze landslide: evaluation and results. Engineering Geology 128: 2–11.

Niethammer U., Rothmund S., James M. R., Travelletti J., Joswig, M., 2010. UAV-based remote sensing of landslides. International Archives of Photogrammetry, Remote Sensing and Spatial Information Sciences, 38(Part 5): 496-501.

Niethammer U., Rothmund S., Schwaderer U., Zeman J., Joswig M., 2011. Open source image-processing tools for low-cost uav-based landslide investigations. International Archives of the Photogrammetry, Remote Sensing and Spatial Information Sciences, Volume XXXVIII-1/C22, isprs Zurich 2011 Workshop, 14-16 September 2011, Zurich, Switzerland.

Oda K., Hattori S., Takayama T., 2016. Detection of slope movement by coparing point clouds created by SfM software. XXIII ISPRS Congress, 12–19 July 2016, Prague, Czech Republic.

Olsen M.J., Johnstone E., Kuester F., Driscoll N., Ashford S.A., 2011. New automated point-cloud alignment for ground-based light detection and ranging data of long coastal sections. Journal of Surveying Engineering 137 (1): 14-25.

Olsen M.J., Kuester F., Chang B.J., Hutchinson T.C., 2010. Terrestrial laser scanning-based structural damage assessment. Journal of Computing in Civil Engineering 24 (3): 264-272.

Oppikofer T., Jaboyedoff M., Blikra L., Derron M.H., Metzger R., 2009. Characterization and monitoring of the Aknes rockslide using terrestrial laser scanning. Nat. Hazards Earth Syst. Sci., 9: 1003-1009.

Pesci A., Teza G., Ventura G., 2008. Remote sensing of volcanic terrains by terrestrial laser scanner: preliminary reflectance and RGB implications for studying Vesuvius crater (Italy). Annals of Geophysics 51(4): 633–653. doi: 10.4401/ag-4455

Pesci A., Teza G., Bonali E., 2011. Terrestrial laser scanner resolution: numerical simulations and experiments on spatial sampling optimization. Remote Sensing 3(1): 167-184.

Picco L., Mao L., Cavalli M., Buzzi E., Rainato R., Lenzi M. A., 2013. Evaluating short-term morphological changes in a gravel-bed braided river using terrestrial laser scanner. Geomorphology 201: 323-334.

Pirotti F., Guarnieri A., Vettore A., 2013. State of the art of ground and aerial laser scanning technologies for high-resolution topography of the earth surface. European Journal of Remote Sensing 46:66-78. doi: 10.5721/EuJRS20134605

Ponzana L., 1993. Caratteri sedimentologici e petrografici della Formazione di Monte Morello (Eocene inferiore-medio, Appennino Settentrionale). Boll. Soc. Geol. Ital. 112: 201-218.

Preparata F.P., Hong S.J., 1977. Convex hulls of finite sets of points in two or three dimensions. Communications of the Association for Computing Machinery 20: 87-93.

Prokop A., Panholzer H., 2009. Assessing the capability of terrestrial laser scanning for monitoring slow-moving landslides. Nat. Hazards Earth Syst. Sci. 9: 1921-1928.

Rahman Z., Slob S., Hack R., 2006. Deriving roughness characteristics of rock mass discontinuities from terrestrial laser scan data. Proceedings of the 10 th IAEG Congress, "Engineering geology for tomorrow's cities". Nottingham, United Kingdom: Geological Society of London; 6-10 September 2006, paper 437, 12 pp.

Remondino F., Barazzetti L., Nex F., Scaioni M., Sarazzi D., 2011. Uav photogrammetry for mapping and 3d modeling - current status and future perspectives-. International Archives of the Photogrammetry, Remote Sensing and Spatial Information Sciences, Volume XXXVIII-1/C22, 2011, ISPRS Zurich 2011 Workshop, 14-16 September 2011, Zurich, Switzerland

Remondino F., El-Hakim S., 2006. Image-based 3D modelling: A review. Photogramm. Rec. 21: 269–291.

RIEGL, 2010a. Data sheet of long range & high accuracy 3D terrestrial laser scanner LMS-Z420i. http://www.riegl.com/uploads/tx_pxpriegldownloads/10_DataSheet_Z420i_03-05-2010.pdf

RIEGL, 2010b. Operating & processing software RiSCAN PRO for RIEGL 3D laser scanners. Available from http://www.riegl.com/uploads/tx_pxpriegldownloads/11_DataSheet_RiSCAN-PRO_22-09-2010.pdf.

Rosser N.J., Petley D.N., Lim N., Dunning S., Allison R.J., 2005. Terrestrial laser scanning for monitoring the process of hard rock coastal cliff erosion. Q. J. Eng. Geol. Hydrogeol. 38: 363–375.

Rossi G., Nocentini M., Lombardi L., Vannocci P., Tanteri L., Dotta G., Bicocchi G., Scaduto G., Salvatici T., Tofani V., Moretti S., Casagli N., 2016. Integration of multicopter drone measurements and ground-based data for landslide monitoring. Landslides and Engineered Slopes. Experience, Theory and Practice – Aversa et al. (Eds)

Royán M.J., Abellán A., Jaboyedoff M., Vilaplana J.M., Calvet J., 2014. Spatio-temporal analysis of rockfall pre-failure deformation using Terrestrial LiDAR. Landslides 11(4): 697-709.

Rychkov I., Brasington J., Vericat D., 2012. Computational and methodological aspects of terrestrial surface analysis based on point clouds. Computers & Geosciences 42: 64-70.

Scaioni M., Feng T., Lu P., Qiao G., Tong X., Li R., Barazzetti L., Previtali M., Roncella R., 2015. Close-range photogrammetric techniques for deformation measurement: Applications to landslides. In: Modern Technologies for Landslide Monitoring and Prediction. Springer Berlin Heidelberg. pp. 13-41.

Scaioni M., Longoni L., Melillo V., Papini M., 2014. Remote sensing for landslide investigations: an overview of recent achievements and perspectives. Remote sens., 6, 1-x manuscripts. doi:10.3390/rs60x000x

Scheidl C., Rickenmann D., Chiari M., 2008. The use of airborne LiDAR data for the analysis of debris flow events in Switzerland. Natural Hazards and Earth System Sciences 8(5): 1113-1127.

Schurch P., Densmore A. L., Nicholas J. R., Lim M., McArdell B. W., 2011. Detection of surface change in complex topography using terrestrial laser scanning: application to the Illgraben debris-flow channel. Earth Surface Processes and Landforms, 36: 1847-1859.

Skempton A.W., Hutchinson J.N., 1969. Stability of natural slopes and embankment foundations. In: Proceedings, 7th International conference of soil mechanics and foundation engineering, Mexico, State of Art volume, 291-340.

Shan J., Toth K., 2008. Topographic laser ranging and scanning: principles and processing. CRC Press, Taylor & Francis Group, LLC, UK.

Slob S., 2008. Automated rock mass characterisation using 3-D terrestrial laser scanning. PhD thesis, University of Delft.

Slob S., Hack H.R.G.K., Turner K., 2002. An approach to automate discontinuity measurements of rock faces using laser scanning techniques. In: Dinid da Gama, C., Riberia e Sousa, L. (Eds) Proceedings of ISRM EUROCK 2002, 25–28 November 2002, Funchal, Portugal, Sociedade Portuguesa de Geotecnia, pp 87–94

Slob S., Hack H.R.G.K., 2004. 3D terrestrial laser scanning as a new field measurement and monitoring technique. In: Engineering geology for infrastructure planning in Europe: a European perspective /editor Hack HRGK, Azzam R, Charlier R – Berlin etc.: Springer (Lecture Notes in Earth Sciences; 104) pp. 179-190.

Slob S., Hack H.R.G.K., 2007. Fracture mapping using 3D laser scanning techniques. In: 11th congress of International Society for Rock Mechanics: the second half century of rock mechanics, 9-13, July, 2007, Lisbon, Portugal/ed. By L.R. e Sousa, C.O.N. Grossmann Leiden: Taylor & Francis/Balkema. ISBN 978-0-4545-084-3, pp. 299-302.

Soudarissanane S.S., 2016. The geometry of terrestrial laser scanning – Identification of errors, modeling and mitigation of scanning geometry. Doctoral thesis, University of Delft. doi:10.4233/uuid:b7ae0bd3-23b8-4a8a-9b7d-5e494ebb54e5

Soudarissanane S.S., Lindenbergh R., Menenti M., Teunissen P., 2009. Incidence angle influence on the quality of terrestrial laser scanning points. International Archivies of Photogrammetry, Remote Sensing and Spatial Information XXXVIII:183-188.

Soudarissanane S.S., Lindenbergh R., Menenti M., Teunissen P., 2011. Scanning geometry: Influencing factor on the quality of terrestrial laser scanning points. ISPRS Journal of Photogrammetry and Remote Sensing 66 (4): 389-399.

Smith M., Chandler J., Rose J., 2009. High spatial resolution data acquisition for the geosciences: kite aerial photography. Earth Surface Processes and Landforms 34: 155–161.

Snavely N., 2008. Scene reconstruction and visualization from Internet photo collections, unpublished PhD thesis, University of Washington, USA.

Spreafico M.C., Bacenetti M., Borgatti L., Perotti L., Pellegrini M., 2013. Structural analysis of San Leo (RN, Italy) east and north cliffs using 3D point clouds. Rend. Online Soc. Geol. Ital. 24: 304-306.

Spreafico M.C., Perotti L., Cervi F., Bacenetti M., Bitelli G., Girelli V.A., Mandanici E., Tini M.A., Borgatti L., 2015. Terrestrial remote sensing techniques to complement conventional

geomechanical surveys for the assessment of landslide hazard: the San Leo case study (Italy). European Journal of Remote Sensing 48: 639-660.

Spreafico M.C., Francioni M., Cervi F., Stead D., Bitelli G., Ghirotti M., Girelli V.A., Lucente C.C., Tini M.A., Borgatti L., 2016. Back analysis of the 2014 San Leo landslide using combined terrestrial laser scanning and 3D distinct element modelling. Rock Mech. Rock Eng. 49: 2235-2251.

Squarzoni C., Delacourt C., Allemand P., 2005. Differential single-frequency GPS monitoring of the La Vallette landslide (French Alps). Engineering Geology 79: 215-229.

Stavroulaki M. E., Riveiro B., Drosopoulos G.A., Solla M., Koutsianitis P., Stavroulakis G.E., 2016. Modelling and strength evaluation of masonry bridges using terrestrial photogrammetry and finite elements. Advances in Engineering Software.

Sturzenegger M., Stead D., 2009. Quantifying discontinuity orientation and persistence on high mountain rock slopes and large landslides using terrestrial remote sensing techniques. Natural Hazards and Earth System Sciences 9: 267-287.

Teza G., Galgaro A., Zaltron N., Genevois R., 2007. Terrestrial laser scanner to detect landslide displacement fields: a new approach. International Journal of Remote Sensing 28: 3425-3446.

Teza G., Pesci A., Genevois R., Galgaro A., 2008. Characterization of landslide ground surface kinematics from terrestrial laser scanning and strain field computation. Geomorphology 97(3): 424-437.

Terzaghi K., 1950. Mechanics od landslides (Berkley volume). Geological Society of America, New York, pp. 83-124.

Theule J.I., Liébault F., Loye A., Laigle D., Jaboyedoff M., 2012. Sediment budget monitoring of debris-flow and bedload transport in the Manival Torrent, SE France. Natural Hazards and Earth System Sciences 12: 731-749.

Thoma T., Gupta S.C., Bauer M.E., Kirchoff C.E., 2005. Airborne laser scanning for riverbank erosion assessment. Remote Sens. Environ. 95: 493–501.

Travelletti J., Delacourt C., Allemand P., Malet J. P., Schmittbuhl J., Toussaint R., Bastard M., 2012. Correlation of multi-temporal ground-based optical images for landslide monitoring: Application, potential and limitations. ISPRS Journal of Photogrammetry and Remote Sensing 70: 39-55.

Travelletti J., Malet J.P., Delacourt C., 2014. Image-based correlation of Laser Scanning point cloud time series for landslide monitoring. International Journal of Applied Earth Observation and Geoinformation 32: 1-18.

Travelletti J., Oppikofer T., Delacourt C., Malet J.P., Jaboyedoff M., 2008. Monitoring landslide displacements during a controlled rein experiment using a long-range terrestrial laser scanning (TLS). Int. Arch. Photogramm. Remote Sens. Spat. Inf. Sci. 37: 485-490.

Turner A.K., Kemeny J., Slob S., Hack H.R.G.K., 2006. Evaluation and management of unstable rock slopes by 3-D laser scanning. IAEG, 404: 1-11.

UNISDR (United Nations International Strategy for Disaster Reduction), 2009. Terminology on Disaster Risk Reduction. 13 pp.

Ullman S., 1979. The interpretation of structure from motion. Proc. R. Soc. London, Ser. B, 203, 405–426, doi:10.1098/rspb.1979.0006.

Van Den Eeckhaut M., Poesen J., Verstraeten G., van Acker V., Nyssen J., Moeyersons J., van Beek L.P.H., Vandekerckhove L., 2007. The use of LIDAR-derived images for mapping old landslides under forest. Earth Surf. Process. 32: 754–769.

Varnes D.J., 1978. Slope movements and type processes. In: Landslides Analysis and Control, Transportation Research Board Special Report 176: 11-33.

Varnes D.J., IAEG Commission on Landslides and other Mass–Movements, 1984. Landslide hazard zonation: a review of principles and practice. UNESCO Press, Paris, 63 pp.

Vericat D., Brasington J., Wheaton J., Cowie M., 2009. Accuracy assessment of aerial photographs acquiring using lighter-than-air blimps: low cost tools for mapping river corridors. River Research and Applications 25: 985–1000.

Voegtle T., Schwab I., Landes T., 2008. Influences of different materials on the measurement of a Terrestrial Laser Scanner (TLS). The International Archives of the Photogrammetry, Remote Sensing and Spatial Information Sciences. Vol. XXXVIII. Part B5. Beijing

Vosselman G, Maas HG (eds), 2010. Airborne and Terrestrial laser scanning. Whittles Publishing, Dunbeath, Scotland.

Wehr A, Lohr U (1999) Airborne laser scanning–an introduction and overview. ISPRS J Photogramm Remote Sens 54:68–82. doi:10.1016/S0924-2716(99)00011-8

Wechsler S.P., 2003. Perceptions of digital elevation model uncertainty by DEM users. URISA Journal 15 (2): 57-64.

Wechsler S.P., Kroll C.N., 2006. Quantifying DEM uncertainty and its effect on topographic parameters. Photogrammetric Engineering and Remote Sensing 72 (9): 1081-1090.

Weichel, H., 1990. Laser Beam Propagation in the Atmosphere. SPIE Optical Engineering Press, Bellingham, Washington. 108 pages.

Westaway R.M., Lane S.N., Hicks D.M., 2003. Remote survey of large-scale braided, gravel-bed rivers using digital photogrammetry and image analysis. International Journal of Remote Sensing 24(4): 795-815.

Westoby M.J., Brasington J., Glasser N.F., Hambrey M.J., Reynolds J.M., 2012. 'Structure-from-Motion' photogrammetry: A low-cost, effective tool for geoscience applications. Geomorphology, 179: 300-314.

Wheaton J.M., 2008. Uncertainty in morphological sediment budgeting of rivers. Unpublished PhD, University of Southampton, Southampton, 412 pp. Available at: http://www.joewheaton.org/Homeresearch/projects-1/phdthesis

Wheaton J.M., Brasington J., Darby S.E., Sear D.A., 2010. Accounting for uncertainty in DEMs for repeat topographic surveys: improved sediment budgets. Earth Surface Processes and Landforms 35: 136-156.

White D.J., Take W.A., Bolton M.D., 2003. Soil deformation measurement using particle image velocimetry (PIV) and photogrammetry. Geotechnique 53(7): 619-632.

Wise S.M., 1998. The effect of GIS interpolation errors on the use of digital elevation models in geomorphology. In: Landform Monitoring, Modelling and Analysis, Lane SN, Richards K, Chandler J (eds). Wiley: Chichester, pp. 139-164.

Wolter A., Stead D., Clague J.J., 2014. A morphologic characterisation of the 1963 Vajont Slide, Italy, using long-range terrestrial photogrammetry. Geomorphology 206: 147-164.

Yin Y., Zheng W., Liu Y., Zhang J., Li X., 2010. Integration of GPS with InSAR to monitoring of the Jiaju landslide in Sichuan, China. Landslides 7: 359-365.

Zhang Z., 1994. Iterative point matching for registration of free-form curves and surfaces. International Journal of Computer Vision 13(2): 119-152.

Zhang Y., Xiong J., Hao L., 2011. Photogrammetric processing of low-altitude images acquired by unpiloted aerial vehicles. Photogramm. Rec. 26: 190–211.

Zhang Z., Zheng S., Zhan Z., 2004. Digital terrestrial photogrammetry with photo total station. International Archives of Photogrammetry and Remote Sensing, Istanbul, Turkey, 232-236.

Zheibak R., Filin S., 2007. Change detection via terrestrial laser scanning. International Archives of Photogrammetry and Remote Sensing XXXVI, Par, 430-435.

www.cloudcompare.org

www.esri.com

www.matlab.com

9. Publications

<u>Published:</u>

- Rossi G., Nocentini, Lombardi L., Vannocci P., Tanteri L., **Dotta G.**, Bicocchi G., Scaduto G., Salvatici T., Tofani V., Moretti S., Casagli N. (2016). Integration of multicopter drone measurements and ground-based data for landslide monitoring. Landslides and Engineered Slopes. Experience, Theory and Practice, Vol.3, pp. 1745-1750.
- Lombardi L., Nocentini M., Frodella W., Nolesini T., Bardi F., Intrieri E., Carlà T., Solari L., **Dotta G.**, Ferrigno F., Casagli N. (2016). The Calatabiano landslide (Southern Italy): preliminary GB-InSAR monitoring data and remote 3D mapping. Landslides (767). DOI: 10.1007/s10346-016-0767-6
- **Dotta G.**, Ferrigno F., Nocentini M. (2016). Semiautomatic geomechanical characterization of Punta Gabbianara rock mass (Giglio Island, Italy). Rend. Online Soc. Geol. It., Bologna.

<u>Accepted by Journals:</u>

- **Dotta G.**, Gigli G., Ferrigno F., Gabbani G., Nocentini M., Lombardi L., Agostini A., Nolesini T., Casagli N. (under review - Rock Mechanics and Rock Engineering). Geomechanical characterization of the bedrock underlying the Costa Concordia cruise ship and stability analysis.

Annexes

- **Annex 1**: Rossi G., Nocentini, Lombardi L., Vannocci P., Tanteri L., **Dotta G.**, Bicocchi G., Scaduto G., Salvatici T., Tofani V., Moretti S., Casagli N. (2016). Integration of multicopter drone measurements and ground-based data for landslide monitoring. Landslides and Engineered Slopes. Experience, Theory and Practice, Vol.3, pp. 1745-1750.

- **Annex 2**: Lombardi L., Nocentini M., Frodella W., Nolesini T., Bardi F., Intrieri E., Carlà T., Solari L., **Dotta G.**, Ferrigno F., Casagli N. (2016). The Calatabiano landslide (Southern Italy): preliminary GB-InSAR monitoring data and remote 3D mapping. Landslides (767). DOI: 10.1007/s10346-016-0767-6

Annexes

Integration of multicopter drone measurements and ground-based data for landslide monitoring

G. Rossi, M. Nocentini, L. Lombardi, P. Vannocci, L. Tanteri, G. Dotta, G. Bicocchi,
G. Scaduto, T. Salvatici, V. Tofani, S. Moretti & N. Casagli
Department of Earth Sciences, University of Florence, Florence, Italy

ABSTRACT: The multicopter drone has an increasing role in remote sensing and aerial photography. The piloting ease and the mechanical simplicity are the main reasons for drone diffusion as a hobby and for professional use. To improve the existing multicopters, the Department of Earth Sciences of Florence (DST) has developed a new type of chassis structure that overcomes some critical issues for scientific and heavy payload or long flight applications. Using the DST Drone, a long term monitoring campaign was performed to understand the possibility of this rising technology to characterize and to monitor landslides. High temporal frequency DEMs are performed by the DST drone in Ricasoli village, in the Upper Arno river Valley (Tuscany) and integrated with data collected by a wireless network of automated instruments: extensometers, biaxial tiltmeters and laser distometer. The integration of different monitoring methods improve the understanding of the movement and the reliability of landslide monitoring. Moreover a validation of drone slope monitoring technique has started to extend the future use of multicopter over landslides areas.

1 INTRODUCTION

Displacement monitoring of unstable slopes is a crucial tool for the prevention of hazards. It is often the only solution for the survey and the early-warning of large landslides that cannot be stabilized or that may accelerate suddenly (Travelletti et al., 2012).

Displacement monitoring techniques can be broadly subdivided into two main groups: ground-based and remote-sensing techniques.

The first group includes all the techniques that necessitate the installation of targets or sensors in and outside the landslide and in measuring their position at different times. Ground-based techniques have proven to be very effective in ground movement monitoring due to their extreme precision (0.2–2 cm), however they have some drawbacks such as their punctual nature, the costs of installation and maintenance. Remote sensing techniques are interesting tools to obtain spatially-distributed information on kinematics (Delacourt et al., 2007), and can be operational from spaceborne, airborne and ground-based platforms. The main advantage of remote-sensing monitoring is capability to provide spatially continuous data, even with centimetric precision, that can be very useful if integrated with the punctual measurements of the ground techniques Tofani et al. 2012).

However, remote sensing analysis performed using conventional platforms (aircrafts and satellites) highlight some drawbacks such as the high costs and the difficult repeatability in a short time.

In the last decade, the combination between a rapid development of low cost and small Unmanned Aerial Vehicles (UAVs) with improved battery technology and the recent improvements of conventional sensors (Optical and LiDAR) in terms of cost and dimensions, lead to new interesting scenarios in environmental remote sensing and surface modelling and monitoring (Colomina and Molina, 2014; Travelletti et al., 2012; James and Robson, 2012; Remondino et al., 2011; Eisenbeiss and Sauerbier, 2011; Fabris and Pesci, 2005).

In particular, as an important mean of obtaining spatial data, UAV remote sensing has the following advantage: real-time, flexibility, high-resolution, low cost, and it can collect information in dangerous environments without risk (Chang Chun et al., 2011).

In this work a multicopter drone, equipped by an optical camera, is used to carry out photogrammetric data acquisition in an area close to the village of Ricasoli, in Tuscany (Italy) that is strongly affected by landslide activity. The aim is the creation of high-resolution 3D surface models which can be integrated with data acquired using an existing ground-based monitoring sensor network

in order to better characterize and to monitor the landslides affecting the village.

2 STUDY AREA

Ricasoli is a village located in a morphological high in the Upper Arno river Valley (Tuscany), an area historically subject to widespread slope instability phenomena. The village is located in a typical NW-SE oriented intramontane basin formed during the extensional phase of the Neogene-Quaternary evolution of the Tyrrhenian side of the Northern Apennines (Abbate, 1983).

The substrate of the basin is composed of Cervarola-Falterona Unit (eastern side) and Macigno Formation (western side). The fluvial-lacustrine sediments were deposited in this area in three phases between Lower Pliocene and Upper Pleistocene and can reach a 500 m thickness (Fidolini et al., 2013).

Ricasoli is located above sediments of the fluvial-lacustrine phase (second phase) overcome by the sediments of the fluvial phase (third phase) (Figure 1). In particular, from the bottom to the top the second phase consists of:

Terranova silt (TER): grey clayey silts in lower part followed upward by medium-fine clayey sands. These sediments have been deposited in a lacustrine environment and the maximum outcrop thickness is 25–30 m.

Ascione Stream Clay (ASC): this unit consists of peaty silty clays deposited in lacustrine environment and they are characterized by the presence of decimetric layers of lignite. The thickness of the outcrops is 15 m.

Silt and Sand of Oreno Stream (LSO): grey silts, occasionally clayey silts or arenaceous silts, which superimpose yellowish fine and medium grained sands. In the inner part of these sediments residual paleosoils and some levels of conglomerates with pebbles of sandstones are present. The origin of this unit can be referred to a lacustrine environment subject to recurrent fluvial episodes and emersion stages. The thickness of the outcrops is 50 m.
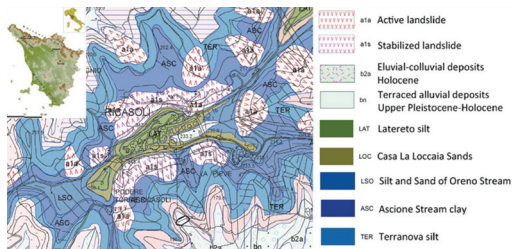
The third phase consists of:

Casa La Loccaia Sands (LOC): Sands and gravels with arenaceous clasts with intercalations of reddish arenaceous silts that often present pedogenesis phenomena.

Latereto silt (LAT): massive silts highly pedogenized, these sediments are deposited in a fluvial plain environment.

This morphological high and the surrounding slopes result to be affected by numerous landslides, which cause the retreat of the escarpments surrounding the village, involving infrastructures and buildings.

According to the Cruden and Varnes (1996) classification, in the area predominantly compound slides and falls can be recognized. In particular, compound slides causing the retreat of the escarpments affect the slope surrounding the village and are triggered by heavy and continuous rainfalls.

In the area many evidences of instability phenomena can be recognized (cracks, fissures on the wall of the buildings and on the streets, small escarpments, corrugation of the soil surface), in particular in the northern slope, recently reprofiled and stabilized.

3 MATERIALS AND METHODS

3.1 *Inclinometric monitoring network*

To monitor the evolution of landslide activity, a network of 12 inclinometers was installed in Ricasoli village and in the surrounding slopes, in autumn 2004. Nowadays 4 inclinometers are no longer operating since they were irreparably damaged by the subsoil movement (Figure 2).

The data have been collected through a digital biaxial probe every 0.5 meters, showing from autumn 2004 to spring 2005 and from 2009 to

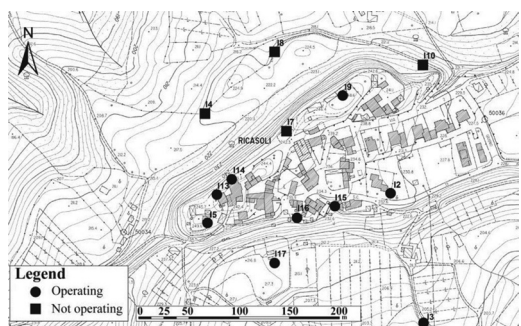Figure 1. Geological map and localization of Ricasoli (Rosi et al., 2013).

Figure 2. Position of operative and not operative inclinometers.

2010 (I2, I4, I5, I7, I8, I9 and I10) the presence of numerous and diffuse instability phenomena (Rosi et al., 2013).

3.2 Wireless sensor network

Since February 2014 a Wireless Sensor Network (WSN) was installed and the obtained data integrated with the traditional instruments. The automated instruments were located in correspondence to the main building cracks and infrastructures.

This sensor node network allows to survey the physical characteristics (e.g. temperature, humidity, inclination, displacements) and to elaborate the surveyed data; each node forwards these data to a coordinating node (called sink node) that in turn send them to a server.

The WSN is composed by 15 sensor nodes, one of which assumes the role of a sink node and a gateway between the network and a server. The data are available online in real time (http://winet-srl.serveftp.com). The sensors are 12 extensometers, 3 biaxial tiltmeters and 2 laser distometers (Figure 3).

3.3 The multicopter drone

Usually multicopters have a "spider" structure with a central body and many radial arms that support the propulsion device.

To improve the structure of the existing multicopter, the Department of Earth Sciences of Florence (DST) has developed a new type of chassis structure that allows to overcome some critical issues for scientific and heavy payload or long flight applications (Figure 4).

The new chassis is patent pending in Italy and PCT (Patent Cooperation Treaty) applied in 117 countries in the world and received its first positive report in Spring 2014.

Figure 3.   Position of the sensors.

Figure 4.   The DST multicopter *Saturn*.

The drone, named *Saturn*, has an innovative perimetric chassis that fully supports flight dynamics. The improved structure has these main key features:

- Increased space without constraints to positioning electronics, flight system and instruments.
- The central payload area can be connected in a rigid manner or even with a flexible mount to dramatically cut down mechanical vibrations from the propulsion system.
- Maximized flexibility of propulsion configuration with a single chassis: without any modifications to the chassis it is possible to vary the number of propulsion systems (three, four, six etc..) even during the flight.
- The flexible propulsion configuration allows us to fit the need of every single mission: less engine to increase autonomy, more engine to allow for heavy payload.
- Variable propulsion geometry to keep the perfect balance with all types of payloads and to manage an emergency landing in case of a propulsion unit failure.

The DST multicopter is a drone, and is capable of autonomous flight, from take-off to landing, and emergency management.

Saturn drone has onboard a complete and fully configurable acquisition system with frame grabber for scientific instruments.

3.4 Digital photogrammetry

In order to obtain a detailed reconstruction of the topography of the site, an aerial photogrammetric survey was performed on July 30th 2015.

Digital photogrammetry is an innovative technique that allows to reconstruct a 3D surface model by triangulating the position in the 3D space, of pixels that are visible in two or more images.

In principle, once images are oriented and, possibly, calibrated, is possible to derive DSM and
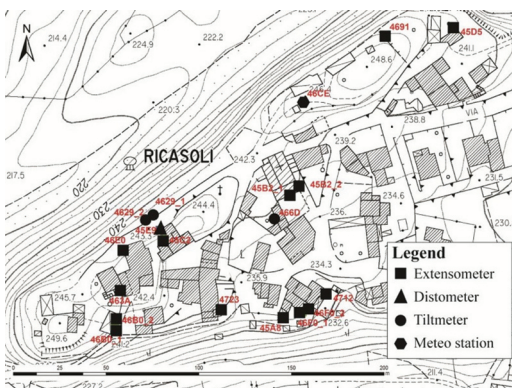
orth photos (Colomina & Molina, 2014), along with very high definition point clouds. This process can be carried out using one of the several Structure-From-Motion (SfM) softwares that, exploiting specific algorithms for image triangulation and bundle adjustment, allow to reconstruct very accurate 3D representation of any surface.

Furthermore, thanks to the time and cost-effectiveness of the technique, is possible to repeat measurement surveys at regular time intervals and monitoring the changes occurred between different acquisitions by and comparing the results.

In this work a point cloud obtained by the 30th multicopter survey is compared to a Terrestrial Laser Scanner (TLS) point cloud, acquired in late March 2015.

The photogrammetric survey is performed in 5 different stages: (1) mission planning, (2) acquisition of ground control points with GPS, (3) flight and image acquisition, (4) image processing and (5) implementation in GIS environment.

The first stage consists in the adoption of the flight plan, that have to be created *ad-hoc* to ensure the best coverage of the target area, with an optimal photo overlap in frontal (overlap) and lateral direction (sidelap), taking into account the camera footprint at a certain quote.

The sidelap and overlap were respectively 50% and 60% in order to guarantee a sufficiently redundant coverage of the area of interest (Fig. 5(a)).

In order to have a georeferenced and calibrated 3D model, a ground GPS survey was carried out by collecting 7 Ground Control Points (GCPs) in correspondence with objects on the ground that can be easily recognized in the aerial photos (Fig. 5(b) and (c)). The images were processed using the software Agisoft Photoscan Professional and the resulting data were implemented in GIS environment (Fig. 5(d) and (e)).

Using the Surface Comparison tool (RiSCAN-PRO; RIEGL, 2010), the drone point cloud was compared with Laser Scanner point cloud, acquired by a Terrestrial Laser Scanner (TLS) on 30th March 2015, collecting 1,500,000 points with angular resolution of 0,034°. This tool allows to compute the distance between a reference triangulated mesh and a compared data point. The comparison was performed assuming the TLS data mesh as reference one and calculating the differences through normal vectors mode. The result is the normal distance between each point of the drone cloud and the plane of the nearest data point of the reference mesh, obtained as an average of all close triangle normal vectors.
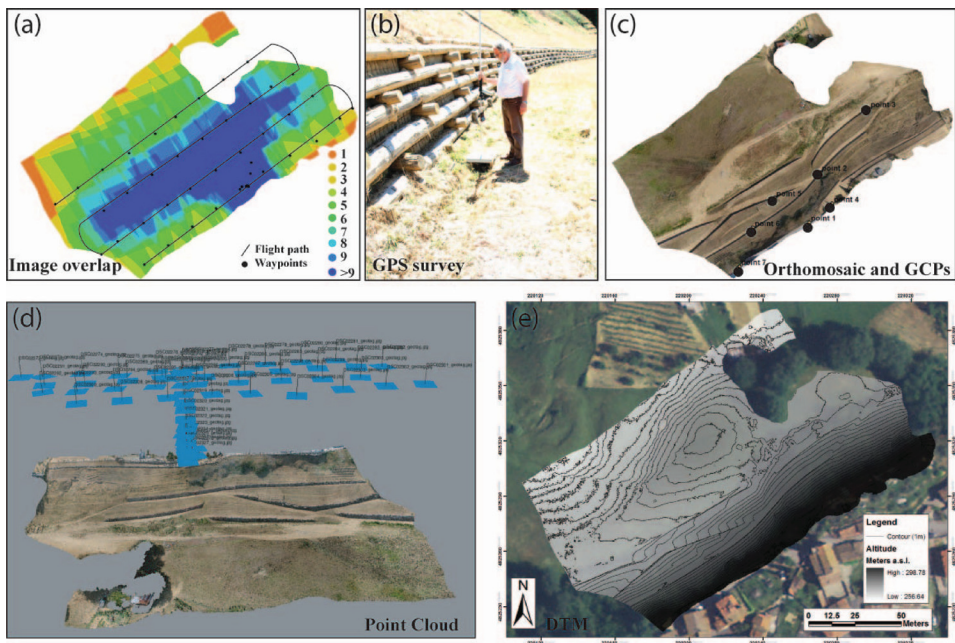

Figure 5. Phases of the multicopter drone survey: (a) Flight plan with image coverage of the area (number of images); (b) acquisition of selected GCPs with GPS; (c) digital image orthomosaic with locations of the 7 GCPs; (d) resulting point cloud with camera positions; (e) georeferenced DTM visualized in a common GIS software, associated with 1 meter contour lines.

4 RESULTS AND DISCUSSION

During the last two years (2013–2015), the inclinometers did not register significant displacements neither in the village nor in the southern slope of the Ricasoli village of the area.

The analysis of the inclinometric data in correspondence with the northern slope, highlighted a main slip-surface at a 13–18 m depth, along with others widespread more superficial surfaces.

In particular, the inclinometer I8 registered an acceleration during the last year of monitoring until rupture, occurred in early 2015 at 13.5 m depth. Also the nearby inclinometer I4 is broken at a depth of 17 m, since 2013, showing an ongoing general deformation at the foot of the northern escarpment.

Since the installation (1st March 2014) the wireless sensor network substantially did not register evident displacements.

The ground image coverage obtained by aerial survey is shown in Figure 5(a); the maximum coverage is in correspondence of the lower part of the escarpment, where every point of the scene is visible in more than 9 images.

Further details on the aerial survey are reported in Table 1.

Table 1. Data related to the flight performed with the multicopter drone on July 30th 2015.

Multicopter drone survey	
Number of images	58
Average flying altitude (m.a.g.l.)	68
Ground resolution (m/pix)	0.019
Coverage area (km²)	0.0185769
Number of tie-points	5952
Number of projections	46717
Error (pix)	0.932718

The resulting digital orthomosaic has ground resolution of ~2 cm-pixel and the 3D point cloud is composed by nearly 57 million points (Figure 5(d)). Furthermore, an high-resolution DTM (0.05 m/pix) was obtained by using the point cloud, appropriately filtered in order to remove all the points processed on trees and high vegetation.

The point cloud acquired by the drone was resampled in order to have the same resolution as the TSL one, equal to 10 centimeter per point.

The result of the comparison do not highlight significant displacement measured along the TLS line of sight, occurred between March 30th 2015 and July 30th 2015, as shown Figure 6.

5 CONCLUSIONS

During the monitoring of the northern slope of Ricasoli different data measured from ground and aerial sensors were integrated. The integration between drone aerial survey and inclinometric and wireless network, permitted to overcome the limitations of the punctual measures of the traditional monitoring systems (inclinometer, distometers, tiltmeters, etc.).

The images acquired during the aerial drone survey allowed to obtain a continue 3D surface model of the studied area using a photogrammetric approach.

The results of the drone survey has proven to be reliable and perfectly integrated with other point clouds acquired with different methods such as, in this case, a high resolution Terrestrial Laser Scanner technique.

The detection of possible displacements occurred in the covered area between the two acquisition was performed by comparing the different surface point clouds. As a result, no significant movements were highlighted by this comparison, in perfect
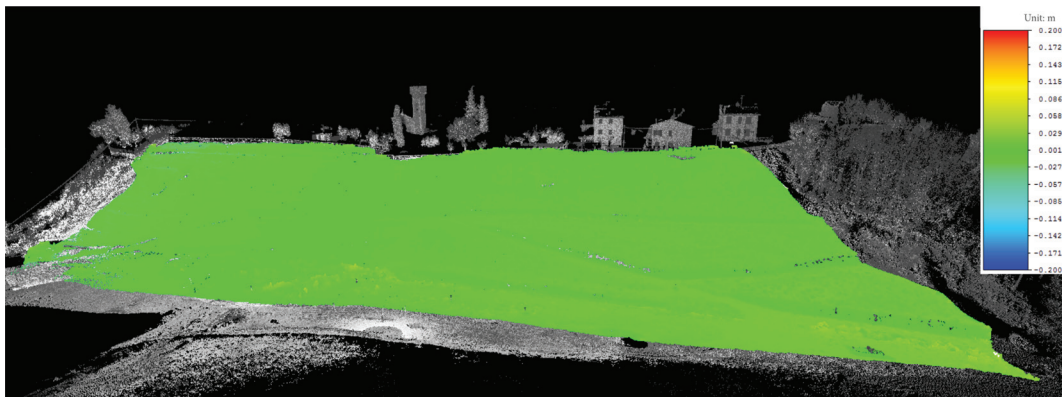

Figure 6. Results of surface comparison between the point clouds acquired using the drone and using TLS.

agree with the information provided by the ground monitoring. However, since no displacements have occurred yet, we do not have a full validation of the reliability of the drone survey technique on an area that is in movement. The correspondence with TLS data is a key and a starting point to introduce drone technique to monitor slope stability, since it has proven to be an easier and more cost—and time—effective approach with respect to laser scanning on a multi temporal survey.

Thanks to these potentials and to its repeatability, drone surveys will become an integral part of the monitoring system in Ricasoli village and will collect more data to validate the technique.

REFERENCES

Abbate, E., 1983. Fluvial-Lacustrine Deposits of the Upper Valdarno. C.N.R., Firenze.

Chang-chun L., Guang-Sheng Z., Tian-jie L., A-du G."Quick image-processing method of UAV without control points data in earthquake disaster area" Trans. Nonferrous Met. Soc. China 21, 2011, s523–s528.

Colomina I., Molina P. "Unmanned aerial systems for photogrammetry and remote sensing: A review" ISPRS Journal of Photogrammetry and Remote Sensing 92, 2014, 79–97.

Cruden, D.M. & Varnes, D.J., 1996. "Landslide Types and Processes". In: A.K. Turner and R.L. Schuster, Eds., *Landslides*: *Investigation and Mitigation*: *Sp. Rep.* 247, National Academy Press, Washington DC, pp. 36–75.

Delacourt C., Allemand P., Berthier, E., Raucoules D., Casson B., Grandjean P., Pambrun C., Varel E.. "Remote-sensing techniques for analysing landslide kinematics: a review". Bulletin de Societe Geologique 178 (2), 2007, 89–100.

Eisenbeiss H. and Sauerbier M. "Investigation of uav systems and flight modes for photogrammetric applications" The Photogrammetric Record 26(136), 2011, 400–421.

Fabris M. and Pesci A. "Automated DEM extraction in digital aerial photogrammetry: precisions and validation for mass movement monitoring" Annals of Geophysics, vol. 48, n. 6, 2005.

Fidolini F., Ghinassi M., Magi M., Papini M. and Sagri M., "The Plio-Pleistocene Fluvio-Lacustrine Upper Valdar—no Basin (Central Italy): Stratigraphy and Basin Fill Evolution," *Italian Journal of Geosciences*, Vol. 132, No. 1, 2013, pp. 13–32.

James M.R. and Robson S. "Straightforward reconstruction of 3D surfaces and topography with a camera: Accuracy and geoscience application" Journal of Geophysical Research, vol. 117, 2012, f03017, doi:10.1029/2011 jf002289.

Remondino F., Barazzetti L., Nex F., Scaioni M. and Sarazzi D. "Uav photogrammetry for mapping and 3d modeling—current status and future perspectives-" International Archives of the Photogrammetry, Remote Sensing and Spatial Information Sciences, Volume XXXVIII-1/C22, 2011, ISPRS Zurich 2011 Workshop, 14–16 September 2011, Zurich, Switzerland.

Rosi A., Vannocci P., Tofani V., Gigli G., Casagli N., "Landslide Characterization Using Satellite Interferometry (PSI), Geotechnical Investigations and Numerical Modelling: The Case Study of Ricasoli Village (Italy)", *International Journal of Geosciences*, 2013, 4, 904–918.

RIEGL (2010) Operating & processing software RiSCAN PRO for RIEGL 3D laser scanners. Available from http://www.riegl.com/uploads/tx_pxpriegldownloads/11_DataSheet_RiSCAN-PRO_22-09-2010.pdf.

Tofani V.; Segoni S.; Agostini A.; Catani F.; Casagli N. Technical note: Use of remote sensing for landslide studies in Europe. Nat. Hazards Earth Syst. Sci. 2013, 13, 1–12.

Travelletti J., Delacourt C., Allemand P., Malet J.P., Schmittbuhl J., Toussaint R., Bastard M. "Correlation of multi-temporal ground-based optical images for landslide monitoring: Application, potential and limitations" ISPRS Journal of Photogrammetry and Remote Sensing 70, 2012, 39–55.

Luca Lombardi · Massimiliano Nocentini · William Frodella · Teresa Nolesini · Federica Bardi ·
Emanuele Intrieri · Tommaso Carlà · Lorenzo Solari · Giulia Dotta · Federica Ferrigno ·
Nicola Casagli

The Calatabiano landslide (southern Italy): preliminary GB-InSAR monitoring data and remote 3D mapping

Abstract On 24 October 2015, following a period of heavy rainfall, a landslide occurred in the Calatabiano Municipality (Sicily Island, Southern Italy), causing the rupture of a water pipeline supplying water to the city of Messina. Following this event, approximately 250,000 inhabitants of the city suffered critical water shortages for several days. Consequently, on 6 November 2015, a state of emergency was declared (O.C.D.P. 295/2015) by the National Italian Department of Civil Protection (DPC). During the emergency management phase, a provisional by-pass, consisting of three 350-m long pipes passing through the landslide area, was constructed to restore water to the city. Furthermore, on 11 November 2015, a landslide remote-sensing monitoring system was installed with the following purposes: (i) analyse the landslide geomorphological and kinematic features in order to assess the residual landslide risk and (ii) support the early warning procedures needed to ensure the safety of the personnel involved in the by-pass construction and the landslide stabilization works. The monitoring system was based on the combined use of Ground-Based Interferometric Synthetic Aperture Radar (GB-InSAR) and terrestrial laser scanning (TLS). In this work, the preliminary results of the monitoring activities and a remote 3D map of the landslide area are presented.

Keywords GB-InSAR · Laser scanning · Landslides · Emergency management · 3D mapping

Introduction

Landslides represent one of the most frequent geo-hazards. They represent serious threats to human life and can cause serious socioeconomic losses on the order of billions of Euros, in terms of damage to property, infrastructure and environmental degradation (Kjekstad and Highland 2009; Petley 2012). Recent events show a significant increase in the number of disasters with natural and/or technological causes, and these disasters can have potentially serious consequences for critical infrastructure (CI) (Murray and Grubesic 2007). Where this infrastructure tends to fail or to be destroyed, the resulting cascade effects (chain of events) can lead to catastrophic damage and negative effects on people, the environment and the economy (Geertsema et al. 2009; Kadri et al. 2014). In countries characterized by a geologically young and tectonically active territory, the susceptibility to instability phenomena is further increased. In Italy in particular, approximately 70 % of the country can be considered exposed to landslide risk (http://www.protezionecivile.gov.it/) and the related estimated socio-economic losses range from 1 to 2 billion dollars annually (Canuti et al. 2004). Currently, these values are certainly underestimated.

In the field of landslide detection, mapping, monitoring and management, the availability of advanced remote sensing technologies, which allow the systematic and easily updatable acquisition of data, may enhance the implementation of near-real-time monitoring activity and the production of landslide maps, optimizing field work (Guzzetti et al. 2012; Frodella et al. 2014). In recent years, the *Ground-Based Interferometric Synthetic Aperture Radar* (GB-InSAR) technique has been widely used to monitor ground displacements in research on landslides (Tarchi et al., 2003; Herrera et al. 2009; Barla et al. 2010; Schulz et al. 2012; Corsini et al. 2013; Bardi et al. 2014), volcanoes (Bozzano et al. 2011; Nolesini et al., 2013; Di Traglia et al. 2014) and sinkholes (Intrieri et al. 2015). *Terrestrial laser scanning* (TLS) has become a widely applied technique for the detection and characterization of several types of mass movements as it allows the rapid collection of detailed and highly accurate 3D ground representations (Abellan et al. 2006; Oppikofer et al. 2008; Jaboyedoff et al. 2009; Fanti et al. 2012; Gigli et al. 2014). The intrinsic characteristics of the abovementioned techniques, such as (i) producing near-real-time displacement maps without physical access to the analysed area; (ii) observing the investigated scenario 24 h per day and in all weather conditions; (iii) generating high-resolution images, especially for analysis of local-scale phenomena; and (iv) providing high versatility and transportability, represent consistent advantages with respect to traditional methods.

This work presents an example of the advantages provided by the integrated use of GB-InSAR and TLS to monitor and manage the post-emergency phase associated with a landslide located in the Catania Province (Sicily Island, Southern Italy). The landslide occurred on 24 October 2015 following intense rainfall that occurred during the previous days (a total of approximately 195 mm measured between 21 and 24 October 2015; data provided by Osservatorio delle Acque—Regione Siciliana) and ruptured a water pipeline that was part of the Messina city aqueduct. Consequently, a considerable lack of water occurred for a large number of the city inhabitants. A provisional by-pass, consisting of three 350-m long pipes passing through the landslide area, was implemented to restore water to the city during the emergency management phase. An integrated monitoring network was also implemented to assess the residual risk by analysing the geomorphological and kinematic features of the landslide and to support the early warning procedures needed to ensure the safety of the personnel involved in the by-pass construction and the long-term landslide stabilization works. The workflow in Fig. 1 explains the organization of the performed activities.

Geological and geomorphological setting

The study area is located in the Calatabiano municipality (Catania Province, Sicily Island), approximately 50 km southwest of the city of Messina and approximately 3 km inland from the Ionian coastline (Fig. 2). From a geomorphologic perspective, the study area is located in the Alcantara River valley, which is delimited to the north by the Peloritani Mountains, to the west by the Nebrodi
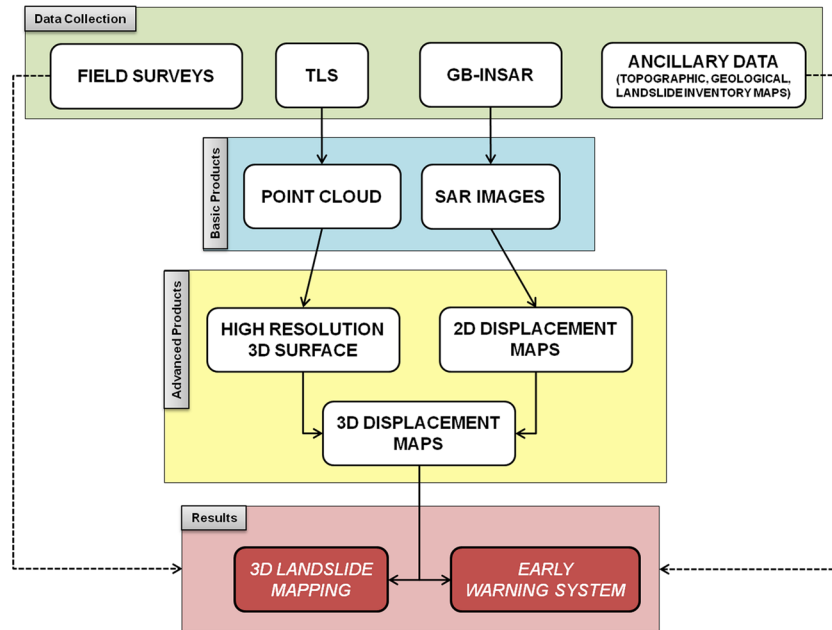
Fig. 1 Logical scheme of the applied operative procedure

Mountains and to the south by the north-eastern slopes of the Etna Volcano (Fig. 2).

The study area is located on the right side of the lowermost Alcantara river alluvial plain and is characterized by hilly terrain ranging from approximately 60 to 250 m a.s.l. The landslide (lat. 37° 49′ 39″; long. 15° 13′ 26″), which featured a 100-m elevation range and was approximately 110 m in maximum length and 65 m in width, affected a large portion of the east-facing slope overlooking the medieval Calatabiano Castle (Figs. 3 and 4). Its topmost sector is characterized by a wide crown area, where a rotational movement (Cruden and Varnes 1996) occurred, displaying a retrogressive behaviour and almost reached the slope ridge at approximately 200 m a.s.l. The landslide body and toe are affected by minor scarps, while two erosional channels, formed by mud flows that almost reached the creek valley at approximately 100 m a.s.l., border the right and left flanks of the landslide (Figs. 3 and 4). The creek valley is located just a few hundred metres from the northern sector of the inhabited area of Calatabiano and represents a high risk for the local population in case of possible landslide reactivation. The landslide-affected slope is characterized by olive trees, shrubs and rocky scattered outcrops, and field surveys have revealed that the mass movement involved detrital slope deposits a few metres thick and consisting of heterogeneous clasts in a coarse sandy matrix with a small percentage of loam (Fig. 4).

These deposits were formed by the weathering and erosion of the bedrock, represented by the arenaceous-conglomeratic facies (PDT_c) of the Piedimonte Formation (Upper Eocene-Lower Oligocene) (Catalano et al. 2010). This lithofacies is composed of irregular alternations of conglomerates and coarse sandstones. The conglomerate layers present thicknesses of up to 10 m, while the sandstone strata rarely exhibit thicknesses greater than 1 m (Catalano et al. 2010). In the upper part of the slope (Fig. 4), a tectonic thrust contact that erased the original heteropic

succession of the two lithofacies represents the transition to the grey clays lithofacies (PDT_a) of the Piedimonte Formation (Cassola et al. 1991).

Employed remote sensing monitoring techniques

GB-InSAR monitoring

The employed radar system is composed of a coherent microwave transceiver unit operating on the Ku band with a bandwidth of 200 MHz and a central frequency of 17.2 GHz. Synthetic aperture is achieved by moving a motorized sled hosting the radar head along a 3-m long straight rail (parallel to the azimuth direction; Fig. 5a). The working principle of the GB-InSAR technique involves radiating microwaves toward the investigated area and measuring the backscattered signal, obtaining a SAR image. The SAR image is created by combining the spatial resolution along the direction perpendicular to the rail (range resolution; ΔRr) and the one parallel to the synthetic aperture (azimuth, or cross-range resolution; ΔRaz) (Luzi 2010), containing amplitude and phase information of the backscattered echo from the investigated scenario objects.

By evaluating the phase difference, pixel by pixel, between two pairs of averaged sequential SAR images of the same scenario, it is possible to obtain a 2D displacement map of the investigated area, which constitutes an interferogram (Luzi et al. 2004; Monserrat et al. 2014). It is important to note that the system is able to measure only the movement component parallel to the instrument line of sight (L.O.S.—direction connecting the sensor and the investigated object), thus displacements that occur in the direction perpendicular to the sensor are missed. The cross-range resolution depends on the target distance, and good acquisition geometries thus depend on the observed scene. The principal limitations of the GB-InSAR technique are due to temporal decorrelation and atmospheric noise (Luzi et al. 2010).
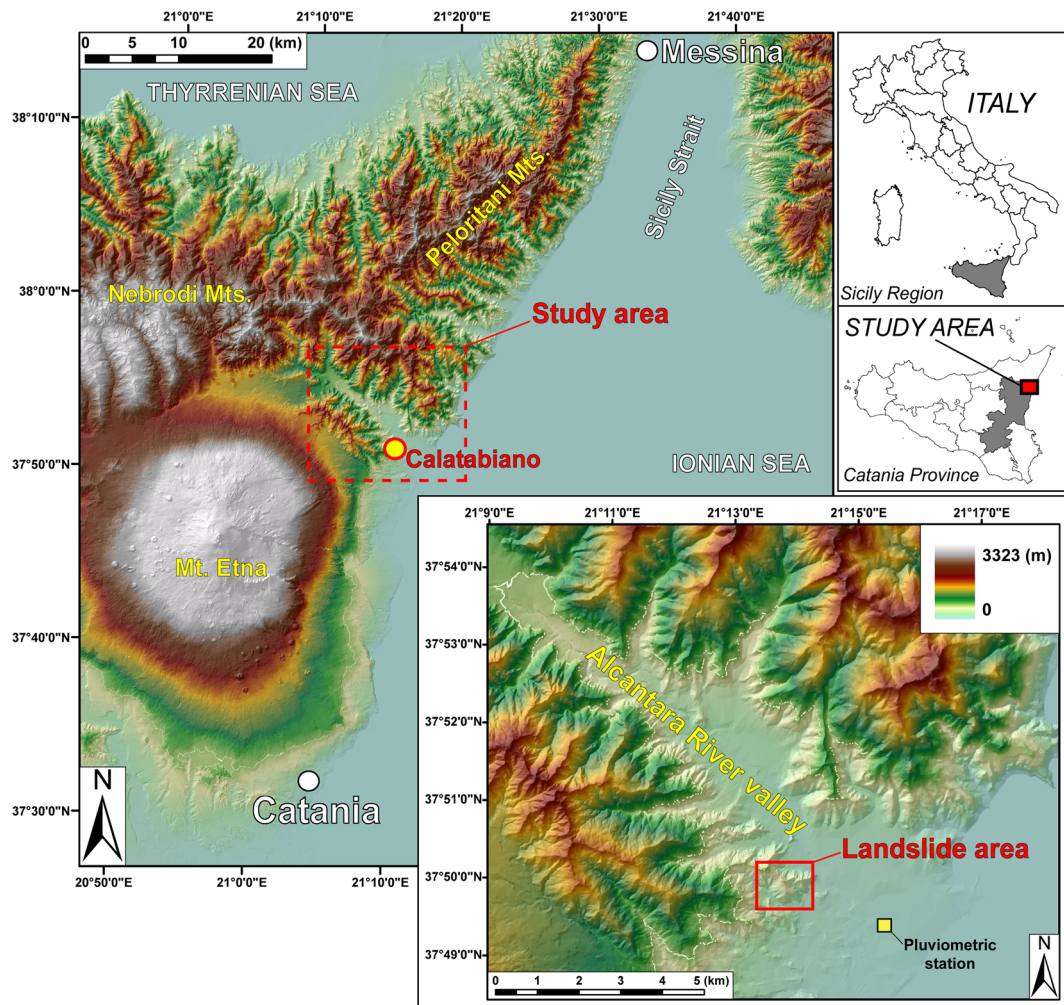
Fig. 2 Study area setting and landslide area location, including the rain gauge station

TLS survey

A TLS device consists of a directional, coherent and in-phase optical beam (or discrete pulses) transmitter, a back-scattered signal receiver and a scanning mechanism (e.g., a rotating mirror). The main product of a long-range laser scanning technique is a high-resolution matrix of points (called a point cloud), defined in polar coordinates (range, horizontal and vertical scanning angle), obtained by measuring the scanner-object distance with great accuracy (on the order of millimetres or centimetres). Given the range distance and the scanning angle, the Cartesian coordinates of each point can be obtained. The high acquisition rate (up to hundreds of thousands of points per second) makes the detailed 3D shape of the object immediately available. Furthermore, for each point, the intensity of the reflected signal is acquired. The intensity data can provide some information about the type of material and the soil moisture content of the targets (Pesci and Teza 2008; Voegtle et al. 2008; Franceschi et al. 2009).

The monitoring system

In the post-landslide event phase, on 11 November 2015, a GB-InSAR system was installed on the terrace roof of the Calatabiano Castle (Fig. 5a, c). With the aim of optimizing the monitoring system efficiency, the following installation criteria were applied: (i) an adequate sensor-target distance (approximately 500 m), aimed at guaranteeing an azimuth resolution spanning from 40 cm (at 150 m range distance) to 106 cm (at 400 m range distance); (ii) minimum presence of obstacles between the radar sensor and the investigated objects; and (iii) a stable radar location (Fig. 5a). The radar system produces interferograms every 2 min, but cumulative displacement maps can be generated using longer (monthly) temporal baselines to detect both rapid and long-term movements. To obtain a high-resolution 3D surface of the post-event landslide area and to geo-rectify the acquired radar images for a better interpretation of the radar displacement data, TLS surveys were performed on 11 November from the radar system position (Fig. 5a). The employed terrestrial laser scanner is a long-range and high-accuracy 3D time-of-flight instrument (model Riegl LMS-Z420i; RIEGL 2010). This device is able to acquire the position of up to 12,000 points/s by calculating the round-trip travel time of a pulsed laser beam (near-infrared wavelength) from the instrument to the scanned object, with a

Fig. 3 **a** Image of the Calatabiano landslide acquired on 10 November 2015, from the monitoring system installation point. The *dashed white line* represents the main landslide crown, the *dashed red line* represents the interrupted pipeline (**b**), and the *black line* represents the new pipeline by-pass (**c**). P1–P8 represent the GB-InSAR monitoring points

maximum angular resolution of 0.008°, an accuracy of ±10 mm (one σ at 50 m range under RIEGL test conditions) and from a maximum distance of 800 m (Fig. 5d). The acquired TLS point cloud (approximately 14.5 million points) was linked to a global reference system by performing a GPS survey of 12 laser reflectors placed on the investigated slope. The raw data were subsequently cleared of vegetation, the data points were triangulated, and a 3D mesh was created to produce a continuous surface for the slope.

Results

Monitoring data

The analysed preliminary radar data spans from 11 November to 31 December 2015, when the crucial landslide restoration works and by-pass construction was performed. The logistics of the GB-InSAR system installation provided a good spatial coverage of the landslide-affected area, including its main features (crown, minor scarps, erosional channels) and the pipeline by-pass and bulldozer trails related to the earthworks (Fig. 5). For the monitored site, the cumulative displacement maps were less affected by atmospheric noise than the single interferograms. Therefore, the cumulative displacement maps were considered more suitable for the ground deformation analysis of the slope and for the detection of landslide critical sectors. The detailed cumulative displacement maps are represented with a colour scale visualization: (i) stable areas are shown in light green; (ii) areas characterized by displacement toward the sensor L.O.S. feature colours from yellow to red and purple (maximum cumulative displacement); and (iii) areas characterized by displacements away from the sensor L.O.S. feature colours from dark green to deep blue (Fig. 6).

With the aim of analysing the landslide kinematics, displacement time series were extracted from 8 monitoring points in the displacement maps. These points were selected on the basis of high coherent values of the radar signal and high representativeness of the landslide behaviour (P1–P8) (Figs. 7 and 8). Specifically, the first six points (P1–P6) are located within the landslide body, and their cumulative displacements range from 4.5 mm (P5) up to 83 mm (P1). These points are representative of the areas that showed the highest displacement. The last two points (P7 and P8) were selected in order to be representative of stable areas: they are located outside the landslide body and correspond to a rocky outcrop and a sector of artificial drainage, respectively.

By means of the radar data analysis, a first relevant displacement phase and two further phases after two acceleration events were detected and analysed (Table 1):

- The first 10 days of monitoring activity (11–21 November 2015) show a widespread sector characterized by cumulative displacement values of up to 24 mm (red oval in Fig. 6) corresponding to the upper landslide crown area. Peak cumulative displacements of up to 55 mm are located in small areas in the landslide top-middle and lowermost sectors (white circles in Fig. 6).
- The first phase (after the first acceleration event; 25–26 November 2015) displays 15-mm peak cumulative displacements localized in two restricted areas: the first corresponding to the landslide upper portion (around control point P4) and the second corresponding to the top-middle one (around control point P1) (Fig. 7a).
- The second phase (after the second acceleration event; 22–22 December 2015) exhibits a 15-mm peak cumulative displacement distributed in a widespread area of the landslide top-middle sector (around control points P1–P4) and along the right flank of the slope (Fig. 7b).
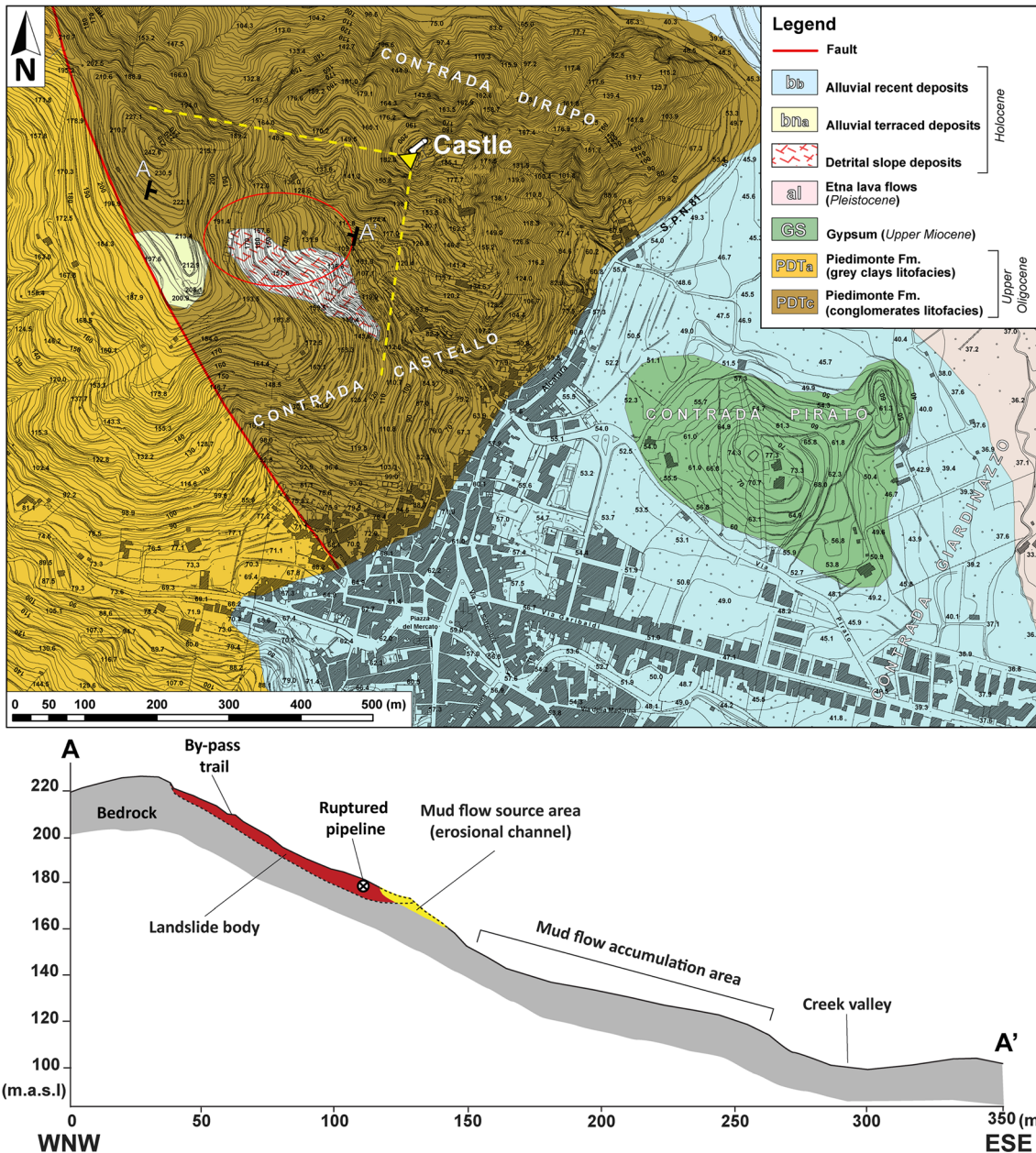
Fig. 4 Geological framework of the landslide area and schematic cross section (*red oval* highlights the landslide area)

To visualize the detected L.O.S. displacements directly on the 3D representation and therefore better localize the most critical areas of the landslide with respect to the work activities (landslide sectors, pipeline by-pass and bulldozer trails), the GB-InSAR data were merged with the TLS 3D model to obtain a 3D GB-InSAR cumulative displacement map (Fig. 9). Figure 9 displays the selected control points and shows that the maximum cumulative displacements recorded during the monitoring period was approximately 100 mm and occurred near the control point P1.

An early warning procedure was also implemented through the adoption of displacement and velocity thresholds calibrated during the first days of monitoring, when the movements were greatest. A simplified early warning system was developed, based on three different warning levels: ordinary, pre-alarm and alarm level. To ensure the safety of the workers involved in the restoration works, hourly displacement thresholds were adopted. A change in the level occurred if the following thresholds are surpassed: between 0.5 and 1.0 mm/h for the pre-alarm and >1.0 mm/h for the alarm level. To prevent possible damage to the pipeline by-pass (here representing the CI) and because this slow-moving landslide did not reach high deformation rates, daily displacement thresholds were adopted (between 12 and 24 mm/day for the pre-alarm and >24 mm/day for the alarm level). Communication, which is a fundamental issue of every early warning system (Intrieri et al., 2015), was achieved through the dispatch of monitoring bulletins every 12 h and whenever the warning thresholds were exceeded.
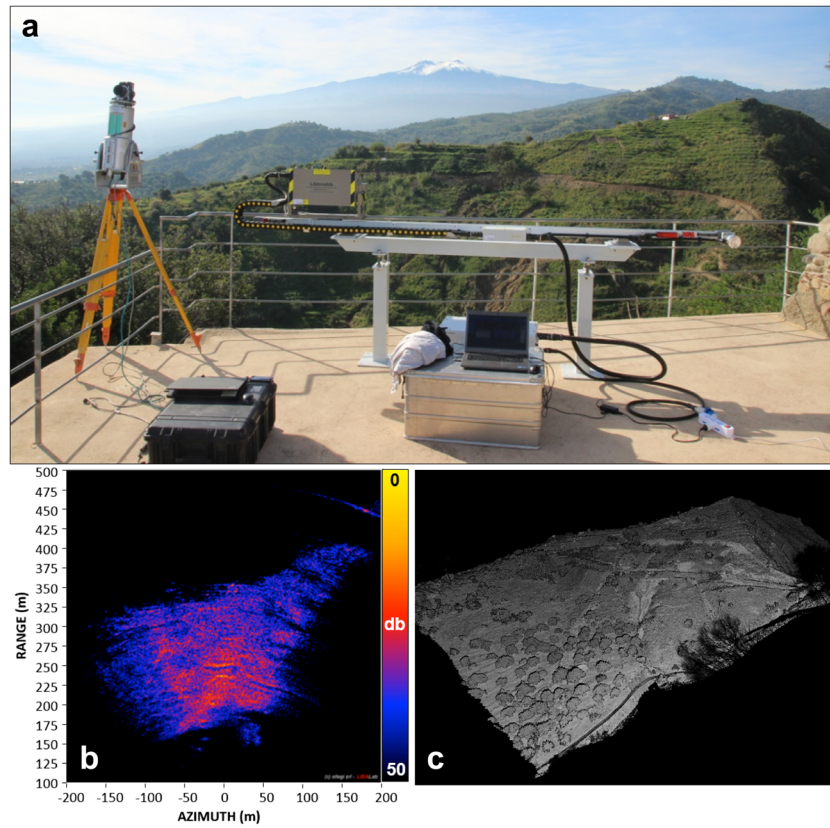
Fig. 5 a Ground-based radar and TLS positioned on the roof of Calatabiano Castle; b power image of the GB-InSAR surveyed slope; c point cloud coloured with intensity values of the reflected laser beam.
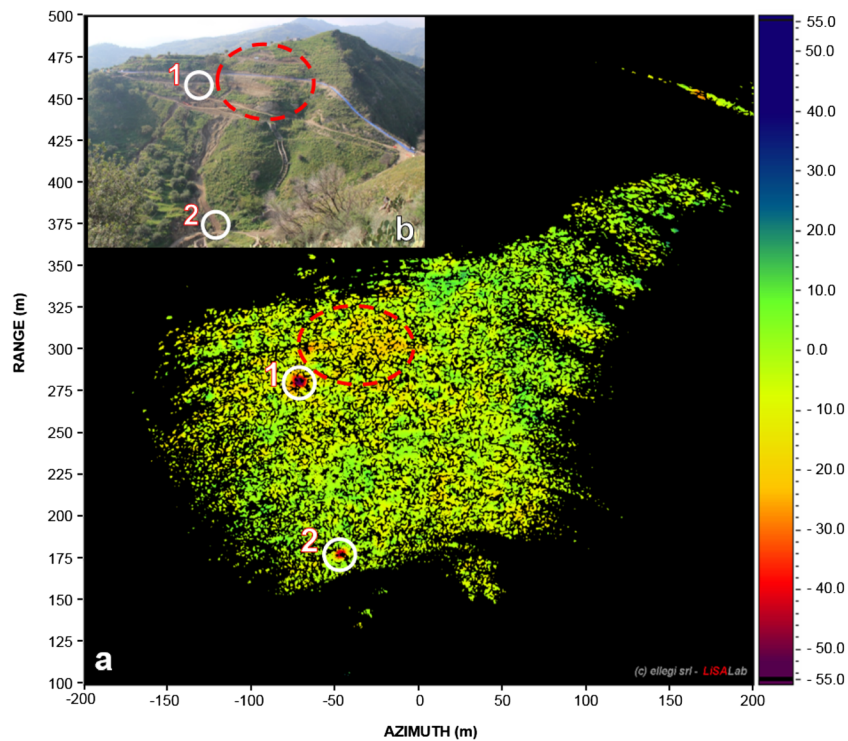

Fig. 6 a Cumulative displacement map obtained by 1 h average interferograms acquired between 11 November 2015 17:59 h GMT + 1 and 21 November 2015 23:00 h GMT + 1 (the *red oval* represents sectors characterized by cumulative displacement values of up to 24 mm, whereas the *white circles* indicate sectors characterized by cumulative peak displacements of up to 55 mm); b corresponding optical image of the landslide scenario acquired on 17 November 2015
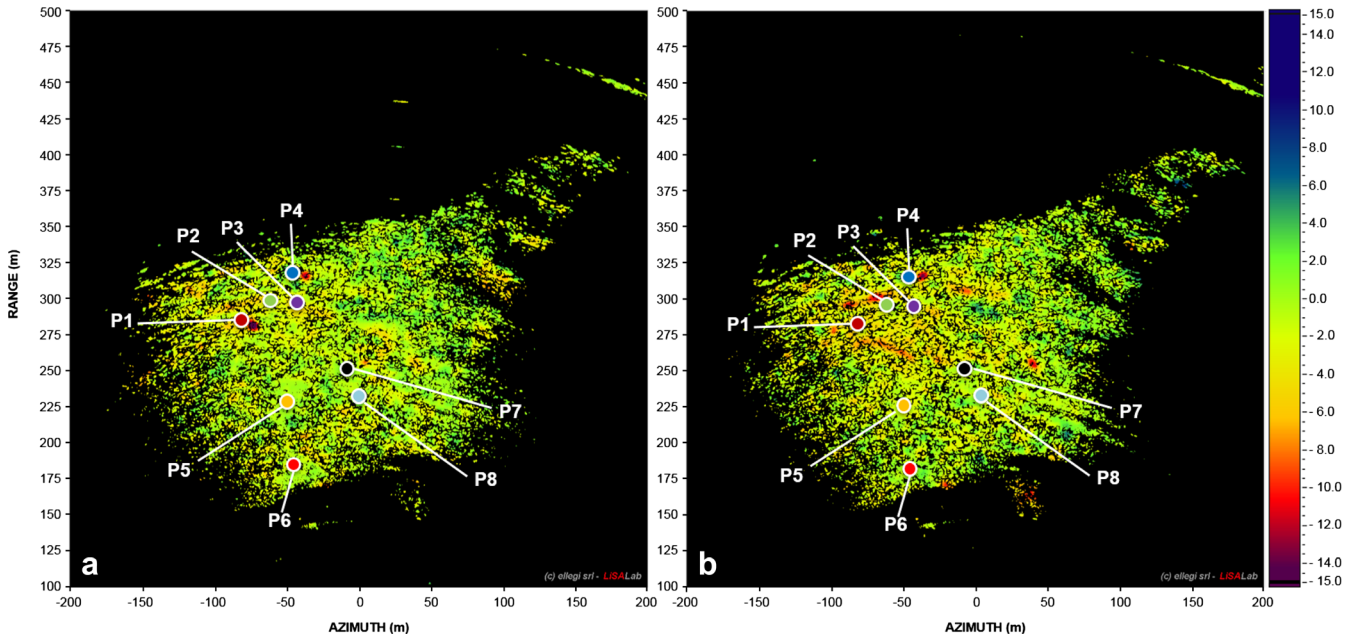
Fig. 7 Cumulative displacement maps obtained based on 1 h averages acquired between **a** 25 November 2015 05:30 h GMT + 1 and 27 November 2015 17:33 h GMT + 1 and **b** 20/12/2015 04:59 h GMT + 1 and 22 December 2015 20:12 h GMT + 1. P1-P8 represent the GB-InSAR monitoring points

Remote 3D mapping

The high-resolution point cloud and the variable laser return intensity values also allowed us to add information regarding the main geomorphologic features of the landslide. In fact, the raw laser scanner product (Fig. 10) shows high intensity values in association with bare soils and rock outcrops. In contrast, the
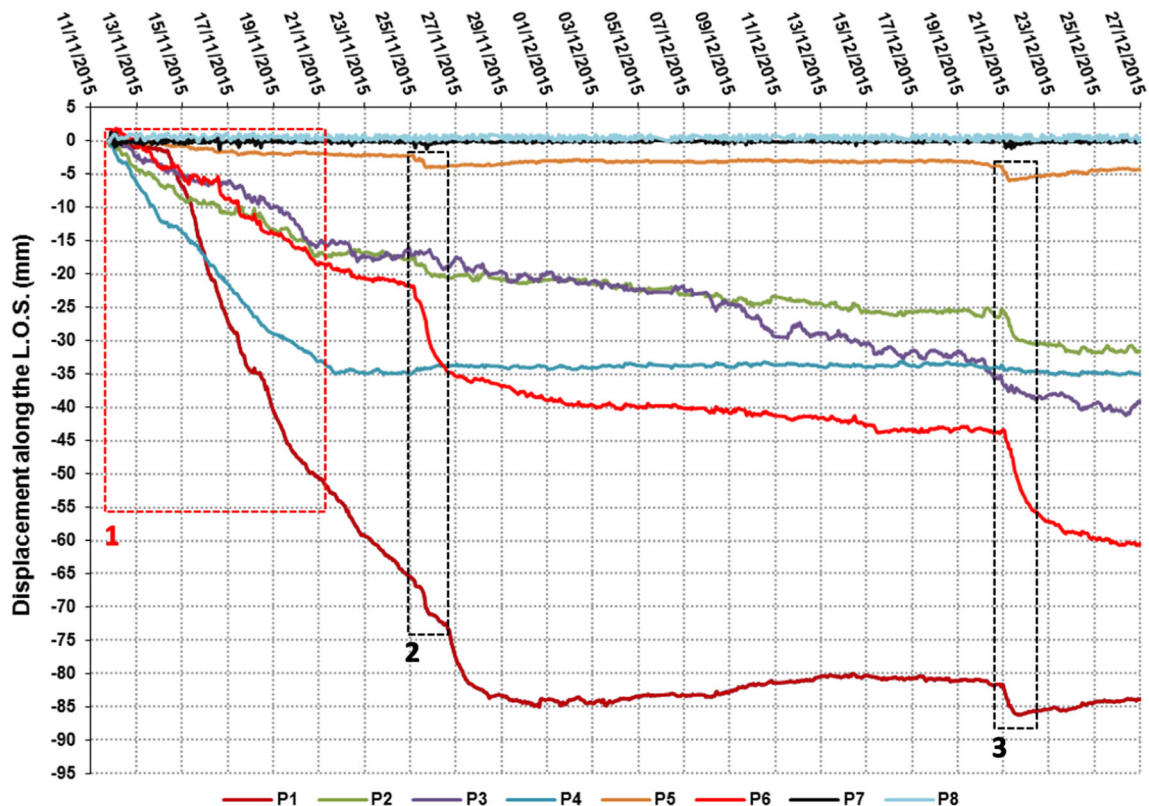
Fig. 8 Time series of GB-InSAR monitoring points (*dotted red rectangle* highlights the detected displacement phase: 1 = first 10 days of monitoring; *dotted black rectangles* denote the phases after the two acceleration events: 2 = first period, 3 = second period).

Table 1 Analysed cumulative displacement (in mm) and acceleration events (mean velocity in mm/day) of the GB-InSAR control points

Time period	Elapsed hours	Point 1 displacement (velocity)	Point 5 displacement (velocity)	Point 6 displacement (velocity)
11 Nov. 2015 17:59–21 Nov. 2015 23:03	244	54.3 (0.22)	2.1 (0.01)	19.6 (0.08)
25 Nov. 2015 02:25–26 Nov. 2015 17:00	37	7.6 (0.19)	1.6 (0.04)	12.8 (0.35)
20 Dec. 2015 23:43–22 Dec. 2015 20:12	45	3.7 (0.08)	0.9 (0.02)	13.7 (0.31)

erosional channel thalwegs of the landslide are characterized by low intensity values, probably due to the moisture influencing the backscattered signal through absorption of the near-infrared wavelength beam (Franceschi et al. 2009). However, it is important to highlight that the difference in intensity values depends on several factors, such as the acquisition geometry (e.g. scanner-object distance and angle of incidence; Kaasalainen et al. 2011), the surface roughness and the presence of vegetation. The TLS point cloud was also used to validate the location of the selected GB-InSAR control points with respect to the landslide geomorphological features: right flank erosional channel topmost sector (P1), by-pass pipes trail (P2, P3), upper crown sector (P4), left flank erosional channel source area (P5), lowermost sector (P6), rock outcrop (P7) and upper sector of the artificial drainage (P8).

Discussion

The main outcomes of this work suggest the effectiveness of the integrated monitoring system adopted to manage the Calatabiano landslide post-emergency phase. The peculiarity of this landslide event was its severe damage to CI, here represented by the disrupted local aqueduct, which produced a water shortage crisis in the city of Messina that lasted for several days and caused problems and discomfort for the local population. The adopted approach gave priority to a rapid system installation and near-real-time monitoring, in order to rapidly detect landslide displacements, ensure the safety of the workers involved in both the water pipeline by-pass construction and the landslide stabilization works and avoid further possible damage to the CI. Thanks to the versatility and portability of the devices, the GB-InSAR system was installed in a few hours on 11 November 2015, and the first displacement data became available while the TLS survey was performed. Furthermore, the employed remote sensing technique integration proved to be effective in surveying and monitoring the whole slope, overcoming the limitations of traditional single-point measurements.

The first 10 days of monitoring (11–21 November 2015; Figs. 6 and 8, Table 1) recorded the highest deformation rates (phase 1), which were related to the residual displacement of the landslide following the initial failure. As shown in Fig. 11, the landslide trigger was clearly related to the rainfall events that preceded on 24 October. In particular, more than 195 mm of cumulative precipitation fell during the period between 21 and 24 October (of which 182 mm occurred solely on 22 October).

Another rainfall event occurred between 30 October and 3 November (a total of 130 mm of cumulative precipitation was recorded, with a daily peak of 90 mm on 2 November; Fig. 11).
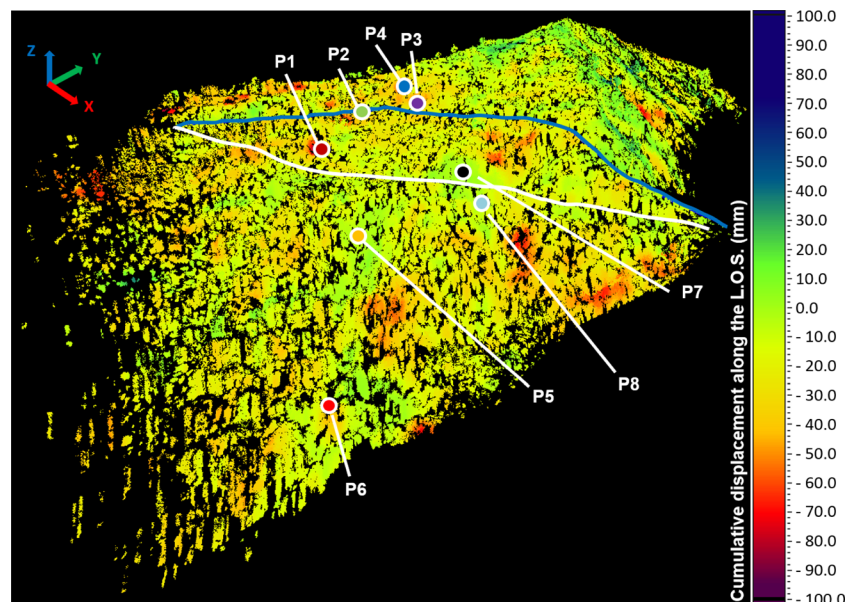

Fig. 9 Cumulative 3D displacement map for the entire monitoring period (from 11 November to 31 December 2015). GB-InSAR monitoring points (P1-P8) are highlighted together with the pipeline by-pass trail (*blue line*) and the bulldozer trail (*white line*)
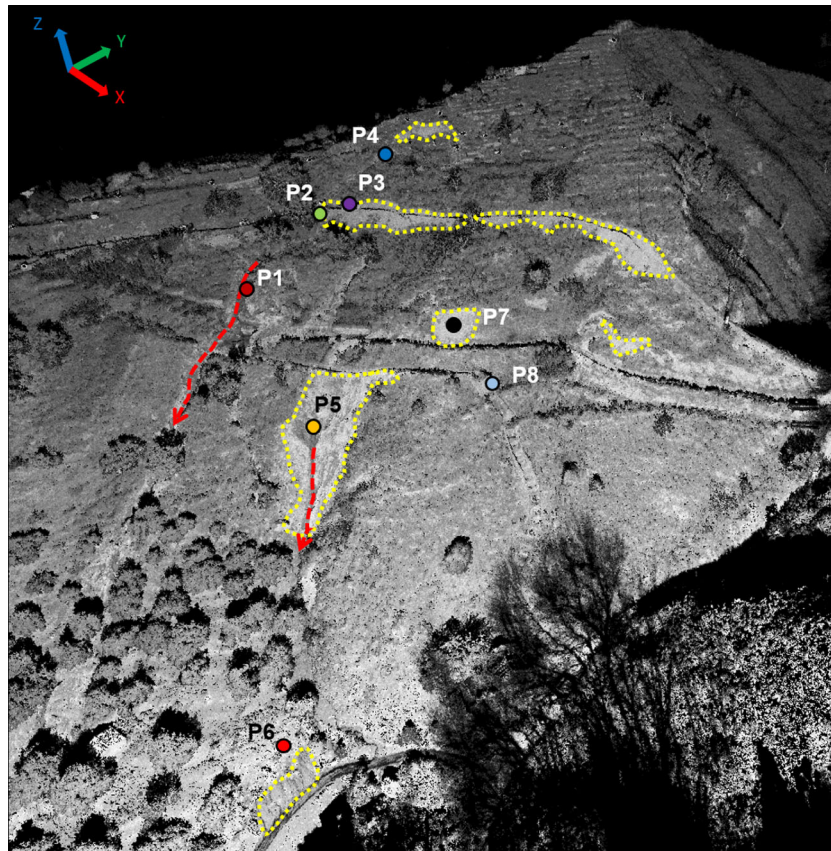
Fig. 10 TLS point cloud shaded by intensity values and GB-InSAR control points. *Yellow dashed polygons* indicate high intensity values related to bare soils and rock outcrops, corresponding to the following slope sectors, from top to bottom: the landslide crown, the by-pass pipes trail, the left bank erosional channel source area and the lowermost sector. The *red lines* mark the thalwegs of the erosion channels. P1–P8 represent the GB-InSAR monitoring points

This event may have contributed to the deformational trend. Two additional, albeit less intense, displacement periods (phases 2 and 3) were recorded during 25–26 November 2015 and 20–22 December 2015 (Figs. 7 and 8, Table 1), coinciding with two less intense rainfall events (approximately 25 and 30 mm of cumulative recorded precipitation, respectively) (Fig. 11). While the
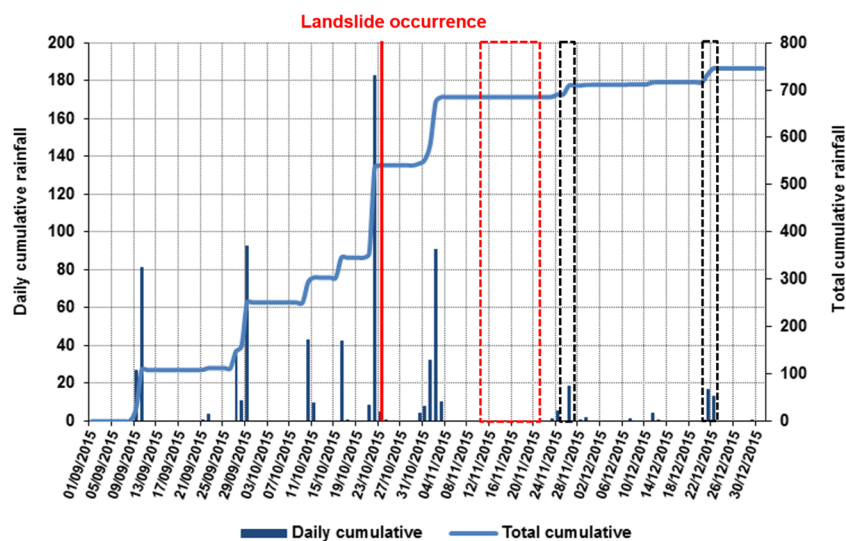

Fig. 11 Rainfall data from the Alcantara rain gauge station (courtesy of Osservatorio delle Acque—Regione Siciliana). *Dashed rectangles* indicate the first 10 days of monitoring (in *red*) and the phases after two further acceleration events (in *black*)
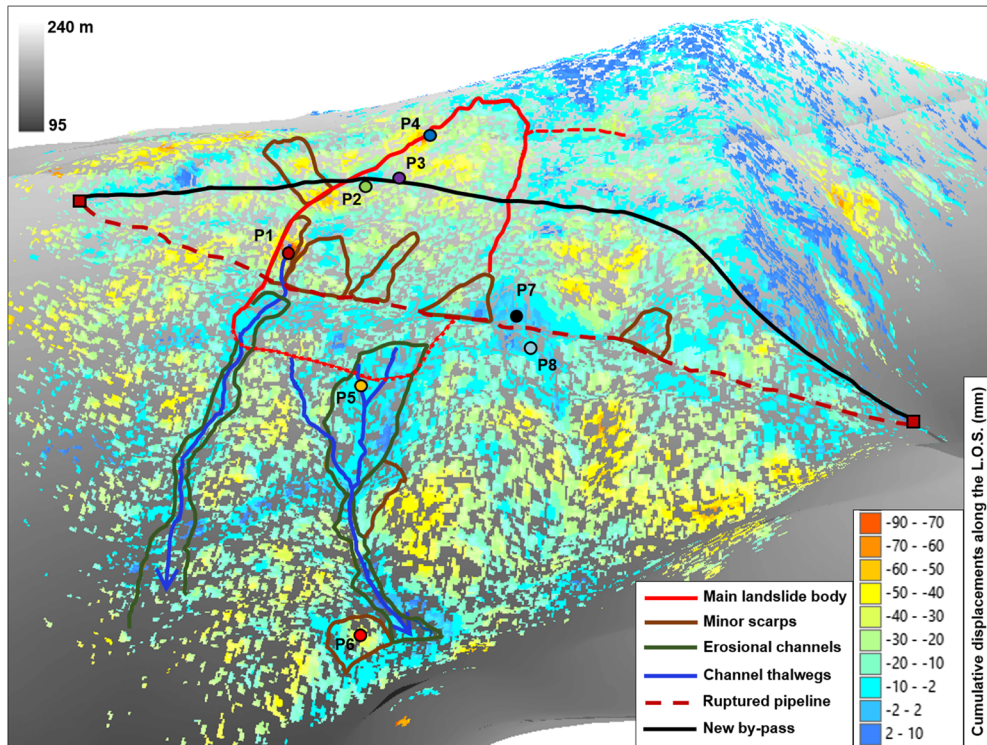
Fig. 12 3D geomorphological map of the Calatabiano landslide, projected on a high-resolution DEM, obtained by means of the TLS survey, and on the GB-InSAR cumulative displacement map. Control points, the pipeline by-pass trail (*black line*) and the ruptured pipeline (*dashed red line*) are highlighted. *P1–P8* represent the GB-InSAR monitoring points

first displacement phase (particularly evident in the P1 and P4 control points time series) shows the features of post-landslide residual deformation, the second and third phases (particularly evident in the P1, P5 and P6 control points series; Fig. 8) were associated with impulsive acceleration events that were very similar in terms of magnitude and elapsed time (Table 1).
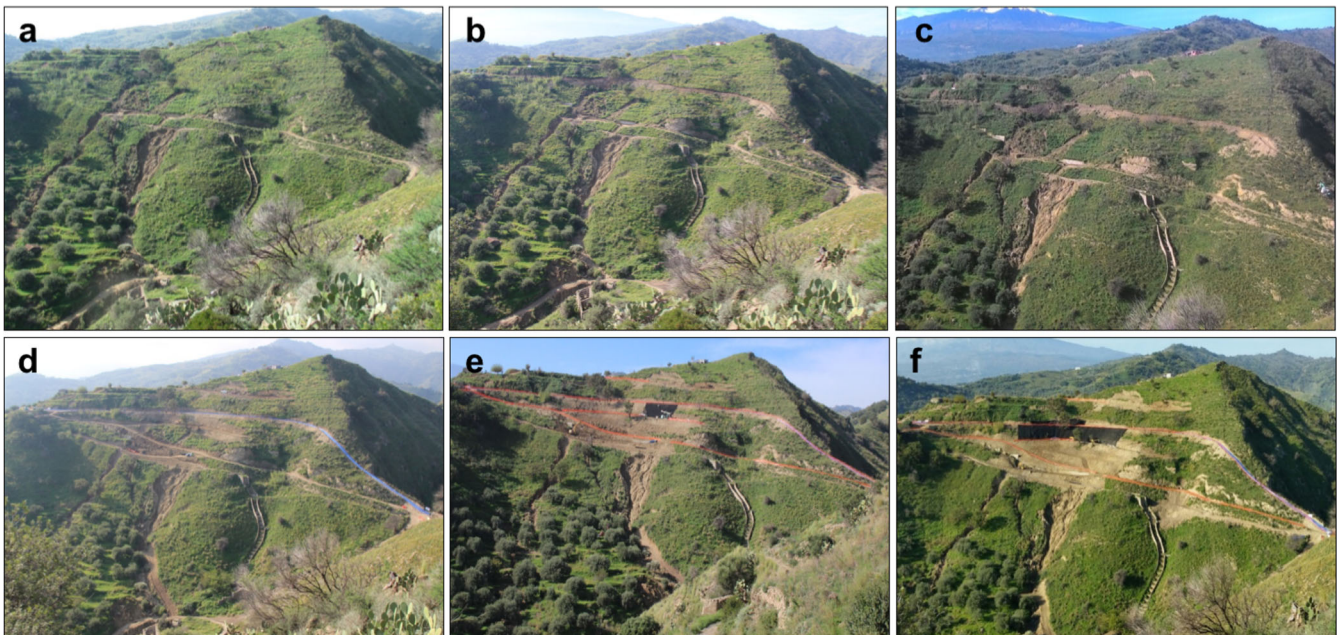

Fig. 13 Evolution of the earthworks on the monitored slope: **a**, **b** by-pass trail construction (10–12 November); **c**, **d** beginning of the slope reprofiling and by-pass pipe emplacement (14–17 November); **e**, **f** geogrid positioning and intense slope reprofiling (21 November–27 December)

The interpretation of the remote sensing data collected from 11 November to 31 December 2015 was supported by means of the remote 3D products (Figs. 9 and 10). Furthermore, these 3D products were integrated to generate an accurate 3D geomorphological map of the landslide (Fig. 12), with the aims of accurately locating the recorded displacements with respect to the landslide geomorphological features and the excavation activities and detecting critical sectors on the monitored slope. The following areas were determined to be critical sectors:

- The uppermost area of the right flank erosional channel, which during the monitored period was affected by high and constant displacements (Figs. 6, 7a and 9), as confirmed by the control point P1 time series (Fig. 8)
- The left flank erosional channel source (control point P5 area) and lowermost sectors (control point P6 area) (minor scarp in Fig. 12). The latter sector proved to be one of the most active in the first 10 days of monitoring (Fig. 6), as displayed by the P6 cumulative displacement (approximately 62 mm, the second highest value within the control points). Corresponding to the erosional channels, the time series of control points P1, P5 and P6 clearly show the presence of displacement, probably induced by the high ground moisture content, as confirmed by the rainfall data (Fig. 11) and field inspections
- The landslide upper crown area (control point P4 area), which was largely involved in the residual deformation observed during the first 10 days of monitoring (Fig. 6)
- The by-pass pipes (located in the area of control points P2 and P3), displaying 32 and 39 mm of cumulative displacement, respectively (Figs. 8 and 9)
- Monitored slope areas located outside the landslide body, corresponding to both the earth movement associated with the excavation of the by-pass and bulldozer trails and the landslide slope re-profiling (Figs. 7 and 13).

The main limitations of the GB-InSAR displacement data interpretation included noise effects and temporal decorrelation, due to the widespread vegetation cover of the monitored slope and the influence of man-made excavations and earth movement related to the by-pass construction and landslide restoration works. Therefore, the remotely sensed data were validated by means of periodic field inspections (Fig. 13), which proved to be crucial in detecting and interpreting the evolution phases of the construction during the monitoring period, especially for the bulldozer trails and slope reprofiling area (Figs. 7b and 13d–f).

The 3D landslide geomorphological map was fundamental in understanding the kinematic mechanisms associated with the landslide mass and in assessing the areal distribution of the landslide (a total of approximately 4900 m²) and its volume (on the order of approximately 25,000 m³, considering a 5-m average thickness of the landslide body based on field surveys). Therefore, accurate mapping provided important information for the local authorities and technicians involved in the emergency management and in the restoration works.

Conclusions

On 24 October 2015, intense rainfall triggered a landslide north of the town of Calatabiano (Sicily Island, Southern Italy). Although the portion of the slope affected by the failure was not exceptional in size or volume and no human casualties occurred, the event had an enormous social impact. The major pipeline providing water to the city of Messina was disrupted, and approximately 80 % of the city had limited access to this vital service for several days. The event demonstrated how the risk associated with landslides should not be assessed and managed only in terms of human safety but also in terms of the vulnerability of critical infrastructure. The remediation works required the creation of a by-pass trail around the damaged pipeline section and had to be performed directly on the unstable slope. Therefore, to assess the safety of the workers, a fully operational real-time monitoring network was deployed. The integrated use of GB-InSAR and TLS techniques allowed for a complete landslide characterization and a continuous assessment of the ongoing deformation rates on the slope. Two displacement thresholds and two velocity thresholds were defined in agreement with the emergency plan, which was based on a scale with three different warning levels. The triggering of the landslide was related to the rainfall events that preceded 24 October 2015, and the two accelerations recorded during the monitoring period (from 10 November to 31 December 2015) were correlated with the amount of precipitation in the area.

References

Abellan A, Vilaplana JM, Martinez J (2006) Application of a long-range terrestrial laser scanner to a detailed rockfall study at Vall de Nuria (eastern Pyrenees, Spain). Eng Geol 88:136–148

Bardi F, Frodella W, Ciampalini A, Bianchini S, Del Ventisette C, Gigli G, Fanti R, Moretti S, Basile G, Casagli N (2014) Integration between ground based and satellite SAR data in landslide mapping: the san Fratello case study. Geomorphology 223:45–60

Barla G, Antolini F, Barla M, Mensi E, Piovano G (2010) Monitoring of the Beauregard landslide (Aosta Valley, Italy) using advanced and conventional techniques. Eng Geol 116:218–235

Bozzano F, Cipriani I, Mazzanti P, Prestininzi A (2011) Displacement patterns of a landslide affected by human activities: insights from ground-based InSAR monitoring. Nat Hazards 59:1377–1396

Canuti P, Casagli N, Ermini L, Fanti R, Farina P (2004) Landslide activity as a geoindicator in Italy: significance and new perspectives from remote sensing. Environ Geol 45(907):919

Cassola P, Giammarino S, Puglisi D, Villa G (1991) Nuovi dati sedimentologico-petrografici e biostratigrafici sulla formazione di Piedimonte (Sicilia nord-orientale). Mem Soc Geol Ital 47:213–223

Catalano S, Corsaro RA, Marino M, Branca S, Cirrincione R, De Guidi G, Di Stefano A, Mazzoleni P (2010) Note illustrative della Carta Geologica d'Italia alla scala 1:50000, Foglio 613, Taormina. Ispra, S. EL. Ca, Firenze

Corsini A, Berti M, Monni A, Pizziolo M, Bonacini F, Cervi F, Ciccarese G, Ronchetti F, Bertacchini E, Capra A, Gallucci A, Generali M, Gozza G, Pancioli V, Pignone S, Truffelli G (2013) Rapid assessment of landslide activity in Emilia Romagna using GB-InSAR short surveys. In: Landslide science and practice. Springer, Berlin Heidelberg, pp. 391–399

Cruden DM, Varnes DJ (1996) Landslides types and processes. In: Turner AK, Schuster RL (eds) Landslides: investigation and mitigation. Transportation Research Board special report 247. National Academy Press, WA, pp. 36–75

Di Traglia F, Nolesini T, Intrieri E, Mugnai F, Leva D, Rosi M, Casagli N (2014) Review of ten years of volcano deformations recorded by the ground-based InSAR monitoring system at Stromboli Volcano: a tool to mitigate volcano flank dynamics and intense volcanic activity. Earth-Sci Rev 139:317–335

Fanti R, Gigli G, Lombardi L, Tapete D, Canuti P (2012) Terrestrial laser scanning for rockfall stability in the cultural heritage site of Pitigliano (Italy). Landslides 5:1–12

Franceschi M, Teza G, Preto N, Pesci A, Galgaro A, Girardi S (2009) Discrimination between marls and limestones using intensity data from terrestrial laser scanner. ISPRS J Photogramm 64:522–528

Frodella W, Morelli S, Fidolini F, Pazzi V, Fanti R (2014) Geomorphology of the Rotolon landslide (Veneto region, Italy). Journal of Maps 10(3):394–401

Geertsema M, Schwab JW, Blais-Stevens A, Sakals ME (2009) Landslides impacting linear infrastructure in west Central British Columbia. Nat Hazards 48:59–72

Gigli G, Intrieri E, Lombardi L, Nocentini M, Frodella W, Balducci M, Venanti LD, Casagli N (2014) Event scenario analysis for the design of rockslide countermeasures. J Mt Sci 11(6):1521–1530

Guzzetti F, Mondini AC, Cardinali M, Fiorucci M, Santangelo M, Chang KT (2012) Landslide inventory maps: new tools for an old problem. Earth-Sci Rev 112:1–25

Herrera G, Fernández-Merodo JA, Mulas J, Pastor M, Luzi G, Monserrat O (2009) A landslide forecasting model using ground based SAR data: the Portalet case study. Eng Geol 105:220–230

Intrieri E, Gigli G, Nocentini M, Lombardi L, Mugnai F, Fidolini F, Casagli N (2015) Sinkhole monitoring and early warning: an experimental and successful GB-InSAR application. Geomorphology 241:304–314

Jaboyedoff M, Oppikofer T, Locat A, Locat J, Turmel D, Robitaille D, Demers D, Locat P (2009) Use of ground-based LIDAR for the analysis of retrogressive landslides in sensitive clay and of rotational landslides in river banks. Can Geotech J 46:1379–1390

Kaasalainen S, Jaakkola A, Kaasalainen M, Krooks A, Kukko A (2011) Analysis of incidence angle and distance effects on terrestrial laser scanner intensity: search for correction methods. Remote Sens 3:2207–2221

Kadri F, Birregah B, Châtelet E (2014) The impact of natural disasters on critical infrastructures: a domino effect-based study. J Homel Secur Emerg 11:217–241

Kjekstad O, Highland L (2009) Economic and social impacts of landslides. In: Landslides–disaster risk reduction. Springer, Berlin Heidelberg, pp. 573–587

Luzi G (2010) Ground based SAR interferometry: a novel tool for geoscience. INTECH Open Access Publisher

Luzi G, Pieraccini M, Mecatti D, Noferini L, Guidi G, Moia F, Atzeni C (2004) Ground-based radar interferometry for landslides monitoring: atmospheric and instrumental decorrelation sources on experimental data. IEEE T Geosci Remote 42:2454–2466

Monserrat O, Crosetto M, Luzi G (2014) A review of ground-based SAR interferometry for deformation measurement. ISPRS J Photogramm 93:40–48

Murray AT, Grubesic TH (2007) Overview of reliability and vulnerability in critical infrastructure. In: Critical Infrastructure. Springer, Berlin Heidelberg, pp. 1–8

Nolesini T, Di Traglia F, Del Ventisette C, Moretti S, Casagli N (2013) Deformations and slope instability on Stromboli Volcano: integration of GBInSAR data and analog modeling. Geomorphology 180:242–254

Oppikofer T, Jaboyedoff M, Blikra LH, Derron MH (2008) Characterization and monitoring of the Aknes rockslide using terrestrial laser scanning. Proceedings of the 4th Canadian conference on geohazards: from causes to management, pp. 211–218

Pesci A, Teza G (2008) Effects of surface irregularities on intensity data from laser scanning an experimental approach. Ann Geophys-Italy 51:839–848

Petley D (2012) Global patterns of loss of life from landslides. Geology 40:927–930

RIEGL (2010) Data sheet of long range & high accuracy 3D terrestrial laser scanner LMS-Z420i. http://www.riegl.com/uploads/tx_pxpriegldownloads/10_DataSheet_Z420i_03-05-2010.pdf

Schulz WH, Coe JA, Shurtleff BL, Panosky J, Farina P, Ricci PP, Barsacchi G (2012) Kinematics of the Slumgullion landslide revealed by ground-based InSAR surveys. In Proc. Landslides and Engineered Slopes: Protecting Society through Improved Understanding—the 11th International and 2nd North American Symposium on Landslides and Engineered Slopes, Banff, Canada, pp. 3–8

Tarchi D, Casagli N, Fanti R, Leva D, Luzi G, Pasuto A, Pieraccini M, Silvano S (2003) Landslide monitoring by using ground-based SAR interferometry: an example of application to the Tessina landslide in Italy. Eng Geol 68:15–30

Voegtle T, Schwab I, Landes T (2008) Influences of different materials on the measurements of a Terrestrial Laser Scanner (TLS). The International Archives of the Photogrammetry, Remote Sensing and Spatial Information Sciences. Vol. XXXVIII. Part B5. Beijing

L. Lombardi · M. Nocentini · W. Frodella · T. Nolesini · F. Bardi · E. Intrieri · T. Carlà · L. Solari · G. Dotta (✉) · F. Ferrigno · N. Casagli
Department of Earth Sciences,
University of Firenze,
Via La Pira 4, 50121, Florence, Italy
e-mail: giulia.dotta@unifi.it

T. Carlà · L. Solari · G. Dotta
Regional Doctoral School of Earth Sciences,
University of Firenze,
Via La Pira 4, 50121, Florence, Italy